

TL  
706.1  
B84  
2006

NUMERICAL STUDY OF BLEED SLOT FLOW CHARACTERISTICS USING  
MAGNETO-AERODYNAMICS

by  
Szymon Buhajczuk, B.Eng  
Bachelor of Aerospace Engineering, Ryerson University, May 2004

A thesis presented to Ryerson University  
in partial fulfillment of the  
requirements for the degree of  
Master of Applied Science  
in the Program of  
Mechanical Engineering

Toronto, Ontario, Canada, 2006  
©Szymon Buhajczuk 2006

PROPERTY OF  
RYERSON UNIVERSITY LIBRARY

UMI Number: EC53480

#### INFORMATION TO USERS

The quality of this reproduction is dependent upon the quality of the copy submitted. Broken or indistinct print, colored or poor quality illustrations and photographs, print bleed-through, substandard margins, and improper alignment can adversely affect reproduction.

In the unlikely event that the author did not send a complete manuscript and there are missing pages, these will be noted. Also, if unauthorized copyright material had to be removed, a note will indicate the deletion.



---

UMI Microform EC53480  
Copyright 2009 by ProQuest LLC  
All rights reserved. This microform edition is protected against  
unauthorized copying under Title 17, United States Code.

---

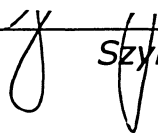
ProQuest LLC  
789 East Eisenhower Parkway  
P.O. Box 1346  
Ann Arbor, MI 48106-1346



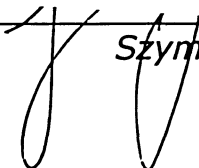
## AUTHORS DECLARATION

I hereby declare that I am the sole author of this thesis

I authorize Ryerson University to lend this thesis to other institutions or individuals for the purpose of scholarly research.

 \_\_\_\_\_  
*Szymon Buhajczuk*

I further authorize Ryerson University to reproduce this thesis by photocopying or by other means, in total or in part, at the request of other institutions or individuals for the purpose of scholarly research.

 \_\_\_\_\_  
*Szymon Buhajczuk*



## **ABSTRACT**

### **"Numerical Study of Bleed Slot Flow Characteristics Using Magneto-Aerodynamics"**

**Szymon Buhajczuk, B.Eng, Master of Applied Science in Mechanical Engineering, Ryerson University, 2006**

A numerical study into magneto-aerodynamic bleed control systems has been undertaken with the intent of improving the shock swallowing ability of high speed engine intakes. Past research had shown that bleed slots effectively remove sufficient mass flow of air from the system to permit shocks to be swallowed. A magnetic field's influence on a charged boundary layer creates a possibility of sealing a bleed slot when not needed. 2D bleed slots were modeled using structured grids for use with the FLUENT CFD solver. User defined functions were written to simulate charge generation and magnetic field forces. Solutions revealed that bleed slot angles, free stream Mach numbers, pressure ratios, boundary layer displacement thickness, field strength and field position all affect how the system performs. Results have shown that a properly positioned magnetic field can reduce sonic flow coefficients up to 88%, thus justifying further research and investment in wind tunnel experiments.



## **ACKNOWLEDGEMENTS**

First and foremost I would like to acknowledge my professor Dr. Paul Walsh for his knowledgeable help and guidance throughout the undergraduate and graduate years. His contributions to my education, scholarly development, and in particular this thesis, have been of paramount importance and influence in my successes. I couldn't have asked for a better supervisor and mentor.

Furthermore, I would like to thank my family and friends for showing their support and exhibiting much patience throughout my university career. They were the backbone and support structure of this endeavor, without which this thesis would not have happened.





# TABLE OF CONTENTS

Authors Declaration.....	iii
Abstract.....	v
Acknowledgements.....	vii
Table of Contents.....	ix
List of Tables .....	xiii
List of Figures.....	xv
Nomenclature.....	xvii
Acronyms.....	xix
Chapter 1: Introductory Topics and Literature Review .....	1
1.0 Introduction.....	1
1.1 High Speed Propulsion .....	2
1.2 Air Inlets & Inlet Starting .....	3
1.3 Bleed Flow Systems.....	7
1.4 Magneto-Hydrodynamics & Magneto-Aerodynamics .....	9
1.5 Flow Control Systems in High Speed Applications .....	10
1.6 Static Charge in Flows.....	13
1.7 Sonic Flow Coefficient .....	14
1.8 Boundary Layer Displacement Thickness .....	15
1.9 Thesis Objectives.....	16
1.10 Thesis Summary – Chapter List.....	17
Chapter 2: Research Scope .....	19
2.0 Research Preparation .....	19
2.1 Assumptions.....	19
2.2 Limitations .....	21
Chapter 3: Computational Domain and Grid.....	23

3.0	Grid Generation .....	23
3.1	Introduction to the Gambit Software Package.....	23
3.2	Domain and Geometry .....	25
3.3	Meshing Techniques .....	26
3.3.1	Hybrid Meshes .....	26
3.3.2	Structured Meshes.....	27
3.4	Important notes on The Final Grid.....	28
Chapter 4: Computation Fluid Dynamics – Simulating Compressible Flow .....		31
4.0	Computational Fluid Dynamics Process Overview .....	31
4.1	Introduction to the Fluent Software Package.....	31
4.2	Solution/Solver Control .....	32
4.3	Turbulence Models Tested.....	33
4.4	Boundary Conditions and Initial Conditions .....	34
4.5	Notes on Solution Accuracy .....	36
4.5.1	Richardson’s Extrapolation.....	38
Chapter 5: Simulating Static Charge and Magnetic Fields.....		41
5.0	Charge Generation and Magnetic Field Simulation.....	41
5.1	Fluent User Defined Functions (UDFs).....	42
5.2	Charge Generation through User Defined Scalar (UDS) Transport .....	42
5.2.1	Transport Equations .....	42
5.2.2	Source Term UDF for Charge Generation.....	43
5.3	Magnetic Field Application .....	45
5.3.1	User Defined Memory (UDM) Location for Field Shape Functions.....	45
5.3.2	Source Term UDFs for Momentum Source.....	46
Chapter 6: Results and Analysis .....		49
6.0	Results.....	49
6.1	Grid Independence Study.....	50
6.2	Solution (Code) Verification.....	53

6.3	Transient Effects .....	56
6.4	Feasibility Considerations (Charge Model Constant Independence).....	58
6.5	Field Strength Variation.....	62
6.6	Field Location Optimization .....	63
6.7	Bleed Slot Geometry Variation.....	66
6.8	Displacement Thickness Variation through Lead Plate Length Variation .....	67
6.9	Mach Number Variation .....	69
6.10	Pressure Ratio Variation .....	71
Chapter 7: Concluding Remarks & Suggestions for Future Research.....		75
7.0	Conclusions.....	75
7.1	Future Research Suggestions .....	77
References.....		81
Appendix A – Supplementary Programs: MATLAB Source Code.....		83
Appendix B – Detailed FLUENT Settings Summary .....		85
Appendix C – User Defined Functions: ANSI C Source Code .....		87
Appendix D – Raw Result Data.....		89



## LIST OF TABLES

Table 1: Edge Meshing Data: Number of Intervals (Nodes - 1) on Edge.....	29
Table 2: Boundary Conditions.....	35
Table 3: Richardson's Extrapolation Sample Results .....	39
Table 4: Relationship of slot location to displacement thickness.....	67
Table 5 : Grid Independence Study and Turbulence Model Selection Data.....	89
Table 6: Charge equation constant independence study, c constant variation.....	89
Table 7: Charge equation constant independence study, $\hat{\phi}$ constant variation.....	89
Table 8: Field Strength Variation Study Data.....	90
Table 9: Vertical Field Positioning Optimization Data .....	90
Table 10: Horizontal Field Positioning Optimization Data .....	90
Table 11: Slot Geometry Variation Study Data (Slot Angle Variation).....	91
Table 12: Boundary Layer Displacement Thickness Influence Data .....	91
Table 13: Mach number Influence Data .....	91
Table 14: Pressure Ratio Influence Data .....	91



## LIST OF FIGURES

Figure 1: Three Examples of High Speed Inlets [15] .....	4
Figure 2: Inlet Starting Schematic: Acceleration and overspeeding [8]. .....	6
Figure 3: Inlet Starting Plot: Acceleration and Overspeeding, Plot for $A_i/A_t = 1.5$ [8].....	6
Figure 4: Schematic from Macheret research on MHD control [13].....	11
Figure 5: Gambit 2.2.30 Software Package .....	24
Figure 6: Domain Breakdown Diagram (B) and Resulting Grid (A) .....	25
Figure 7: Hybrid Mesh Interface near Boundary Layer.....	27
Figure 8: Grid close up of hole region created in GAMBIT.....	28
Figure 9: Visual Reference for Edge Meshing Data.....	29
Figure 10: Final Computational Grid created in GAMBIT .....	29
Figure 11: Y+ on Geometry Walls: Turbulence Model Compliance .....	34
Figure 12: Boundary Condition Application Diagram (Schematic not to scale).....	35
Figure 13: Residual Convergence Plot .....	37
Figure 14: Mass Flow Rate Convergence Plot .....	37
Figure 15: Solution procedure for obtaining grid-converged mass flow rate.....	40
Figure 16: Contours of User Defined Scalar (Charge Per Unit Mass) .....	45
Figure 17: Field Shape Factor Product ( $h_x h_y$ ) stored in User Defined Memory .....	47
Figure 18: Definition of Case Variables .....	50
Figure 19: Grid Sensitivity for a Mach 1.97 Bleed System through a 90 Degree Slot.....	51
Figure 20: Grid Sensitivity Study for a Mach 1.97 Bleed System through a 90 Degree Slot - Influenced by Magnetic Field / Charge Generation.....	52
Figure 21: Conservation of Mass through slot study .....	52
Figure 22: Prandtl-Meyer Inlet. Code verification case at Mach 8.3.....	53
Figure 23: Published Figure [7] with thesis results (circled points) superimposed.....	54
Figure 24: Stream Lines within 90° Bleed Slot showing a Vena-Contracta.....	55
Figure 25: Vortex shedding from the bleed jet within plenum.....	56
Figure 26: Transient Sequence of Vortex Shedding (mass flow constant at 0.371 kg/s) .	57
Figure 27: Steady state Mach Contours solution showing Diamond Shock Pattern .....	57
Figure 28: Steady state converged solution with plenum .....	58



Figure 29: $Q$ versus $\max(\hat{q})$ , Demonstration of Coefficient Independence.....	59
Figure 30: $c$ Constant vs. Sonic Flow Coefficient: $90^\circ$ slot at Mach 1.97 .....	60
Figure 31: $c$ Constant vs. Maximum Charge Per Unit Mass: $90^\circ$ slot at Mach 1.97 .....	60
Figure 32: $\hat{\phi}$ Constant vs. Sonic Flow Coefficient: $90^\circ$ slot at Mach 1.97 .....	61
Figure 33: $\hat{\phi}$ Constant vs. Maximum Charge per Unit Mass: $90^\circ$ slot at Mach 1.97 .....	61
Figure 34: Field Strength Variation vs. Sonic Flow Coefficient .....	62
Figure 35: Magnetic Field positioning ( $h_x, h_y$ contours), Baseline and Optimized Case....	63
Figure 36: Field Centre Vertical Location Variation Study.....	64
Figure 37: Field Centre Horizontal Location Variation Study .....	64
Figure 38: Mach contours resulting from optimized field location .....	65
Figure 39: Mach Contours of $70^\circ$ Slot at a Free stream Mach number of 1.97 - Field On	66
Figure 40: Effect of $\delta^*$ on Sonic Flow Coefficients with Magnetic Field On & Off.....	68
Figure 41: Influence of $\delta^*$ on Effectiveness of Bleed Flow Control.....	68
Figure 42: Mach number and Sonic Flow Coefficients with Magnetic Field On & Off..	70
Figure 43: Influence of Mach number on Effectiveness of Bleed Flow Control.....	70
Figure 44: Effect of Pressure Ratio with Magnetic Field On & Off.....	72
Figure 45: Influence of Pressure Ratio on Effectiveness of Bleed Flow Control.....	72
Figure 46: Reversed flow induced by Magnetic Field at Pressure Ratio of 0.6 .....	73

## NOMENCLATURE

$A$	cell boundary area
$A^*$	reference area at sonic condition (typically throat)
$a$	speed of sound
$B$	magnetic field strength
$c$	shear-charge scaling constant
$D$	bleed slot width ('diameter')
$e_t$	total energy
$F_{x,y}$	momentum source terms
$h_{x,y}$	magnetic field shape factors
$h_g$	average grid size
$I$	Value index in numerical integration (summation)
$L$	slot depth
$M_w$	molecular weight
$N$	total number of discrete values used in numerical integration
$\dot{m}$	mass flow rate
$p$	pressure / order of convergence in Richardson's Extrapolation
$\hat{q}$	charge per unit mass [coulombs/unit mass]
$q(p)$	natural log function used in Richardson's Extrapolation
$Q$	sonic flow coefficient
$r$	grid refinement factor
$R$	gas constant
$S_{\hat{q}}$	charge per unit mass source term

$dS_{\dot{q}}$	derivative of charge per unit mass source term
s	sign function result
T	temperature
u,v	velocities (x and y components)
$U_{\infty}$	free stream velocity
x,y	Cartesian coordinates within the domain
$x_{\text{field-centre}}$	magnetic field centre x-coordinate
$y_{\text{field-centre}}$	magnetic field centre y-coordinate
V	cell volume
$\delta^*$	boundary layer displacement thickness
$\hat{\phi}$	charge-derivative scaling constant
$\gamma$	specific heat ratio
$\rho$	density
$\Gamma$	charge diffusion coefficient

## ACRONYMS

CFD	Computational Fluid Dynamics
EHD	Electrohydrodynamics
MHD	Magnetohydrodynamics
UDF	User Defined Function
UDS	User Defined Scalar
UDM	User Defined Memory
GUI	Graphical User Interface
RNG	Renormalization-group
SA	Spalart Allmaras



# **CHAPTER 1: INTRODUCTORY TOPICS AND LITERATURE REVIEW**

## **1.0 INTRODUCTION**

In the quest for speed, developments in propulsion and high speed aerodynamics have moved in leaps and bounds. To reach hypersonic speeds, typically defined as Mach 5 and above, air vehicles require specifically engineered propulsion systems designed to function at these high Mach numbers. The focus of this thesis is to explore the operational bounds of a bleed flow system using magneto-aerodynamics to control mass intake on high speed engines. Bleed flow systems have been proposed in the past to allow the removal of mass flow from the engine inlets. This has been done to allow supersonic engines to accelerate through lower Mach numbers to their design speed without a loss in performance. Since bleed flow within an engine is not desirable once a design Mach number has been reached, a control system which could seal the bleed perforations would be of great value. By taking advantage of the a flow's statically charged boundary layer, a magneto-aerodynamic bleed flow control system has the potential to control bleed without introducing any moving components into the system,

thus keeping the engines simple and efficient. To evaluate the feasibility of the magneto-aerodynamic system, this thesis has relied on numerical analysis, employing a commercial Computation Fluid Dynamics (CFD) software package, FLUENT. As compared to wind tunnel and other experimental testing, CFD has the advantage of being fast, and relatively inexpensive. S.D. Holland [10] showed that CFD is a good tool for designing experimental setups within the realm of hypersonic aerodynamics. Holland's studies of internal scramjet inlet aerodynamics found that numerical research such as this could be used to drive the design of detailed experiments. This indicates that CFD is a commonly used tool for initial research and design work for high speed propulsion. The intent of this thesis is to study the potential of bleed control systems and act as a starting point for future experimental research using Ryerson University's high speed wind tunnel.

The following introductory sections will focus on describing current technology in high speed propulsion and progressively narrow the focus to describe in detail bleed flow systems and their potential for magneto-aerodynamic control.

## **1.1 HIGH SPEED PROPULSION**

There are several categories of engines designed for supersonic flight. Currently, turbojet engines are almost exclusively used in present day aerospace applications. One inherent limitation of such engines is the complexity of their designs. They require multiple stage compressors and turbines, each consisting of hundreds of blades. The ability to generate thrust within such an engine is often limited by the temperature tolerance of the materials used within the turbine stages of the engine. To move beyond the limitations of a turbojet engine, ramjet and scramjet engines have been proposed as alternate methods of propulsion which significantly reduce the complexity of the engine and can significantly increase the flights speeds of the aircraft. Although these engines are simpler because they have fewer moving components, there are many aerodynamic design challenges in making them efficient and practical.

A ramjet differs from a traditional turbojet engine in that it does not have a standard compressor to increase intake air pressure or a turbine to drive the compressor. Intake air is compressed in the diffuser by decelerating the incoming air to subsonic

speeds and recovering higher pressures in a technique commonly referred to as 'ram' compression. The scramjet (or supersonic combustion ramjet) engine works on the same principle as the ramjet, with the one difference that the flow in the diffuser is never decelerated below Mach 1 and hence combustion occurs at supersonic speeds [8]. The scramjet engine, due to its ability to ingest high speed flows and perform combustion at supersonic speeds with fewer aerodynamic losses, is a primary candidate for propulsion of hypersonic vehicles.

One of the greatest challenges of designing a ramjet or scramjet, is the design of the inlet. High speed engines such as this are typically designed for a single design Mach number. This means that acceleration to the design Mach numbers is made difficult by the presence of flow spillage around the engine and shockwaves present ahead or within the engine inlets themselves. The process of removing these shockwaves and any spillage that occurs is known as inlet starting. There are numerous ways this can be accomplished, one of which is the application of bleed holes within the inlet.

## 1.2 AIR INLETS & INLET STARTING

The goal of an inlet is to decelerate and compress the flow, hence conditioning it for fuel addition and burning. Ideally, the process should be as close to isentropic as possible, with a minimal numbers of shocks. Three examples of such inlets are the Busemann Inlet, Prandtl-Meyer Inlet, and Oswatitsch Inlet [15]. These three inlet types, seen in Figure 1, demonstrate common characteristics such as an isentropic compression region and a final oblique or normal shock near the throat. The Busemann and Prandtl-Meyer inlets are similar in that they both use internal compression, with the Busemann inlet being axi-symmetric. The Prandtl-Meyer Inlet is a 2D inlet that ends with flat walls on each side. The Oswatitsch inlet is unique because the isentropic compression is not performed inside the inlet but rather ahead of the inlet using an externally protruding centre-body. According to inviscid theories studied by Molder *et al.* [15], the Busemann inlet is the most efficient of the three. A viscous analysis and experimentation showed that the Prandtl-Meyer inlet has the lowest performance, while the other two have essentially equal efficiencies and performance [15].



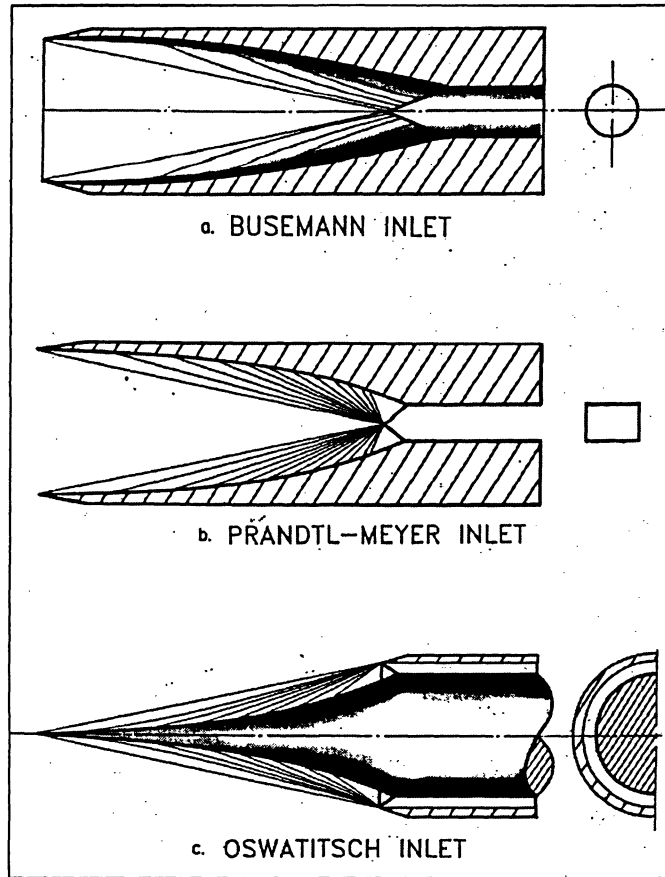


Figure 1: Three Examples of High Speed Inlets [15]

Accelerating an inlet to its design Mach number can be difficult because of the formation of shocks ahead of the inlet itself, preventing sufficient mass flow to achieve the design speed. Without the use of bleed, an inlet can be started (with mass spillage and strong shocks removed from the system) by over speeding the inlet. Figures 2 and 3 are shown to facilitate the explanation by comparison of physical phenomena to the mathematics of the situation. The different stages of starting the inlet are labeled (a) through (f) [8].

Ideally, the inlet to throat area ratio  $A_i/A_t$  is the same as the ratio of capture area to throat area ratio  $A_a/A_t$ . This can only occur at the design Mach number, under isentropic conditions. To begin the acceleration to design conditions, the inlet is initially in a subsonic free stream condition. Stage (a) of the starting process shows that the incident Mach number is sufficiently subsonic so that the inlet is not choked at the throat. The capture area  $A_a$  is dependent on downstream conditions forcing some of the flow to divert

around the inlet. As the Mach number is increased, stage (b) shows that the throat becomes choked and sonic. This means that the capture area and ratio  $A_a/A_t$  becomes dependent on the upstream Mach number. This relationship is defined by the equation below and shown as a solid line in Fig 3 [8]:

$$\frac{A_a}{A_t} = \frac{1}{M} \left[ \frac{2}{\gamma+1} \left( 1 + \frac{\gamma-1}{2} M^2 \right) \right]^{(\gamma+1)/2(\gamma-1)} \quad (1)$$

In stage (b), Equation 1 and Figure 3 indicate that the capture area ratio  $A_a/A^*$  is lower than the physical inlet area ratio  $A_i/A_t$ , where  $A^*$  is area at sonic conditions. To satisfy this difference in area ratios, flow spillage becomes the accommodating mechanism. As the flight Mach number goes sonic in stage (c), a weak detached shock forms ahead of the inlet. This shock is needed to reduce the velocity back to subsonic where the flow continues to spill around the inlet. It is past this point that non-isentropic effects start to play a role. This can be seen in Figure 3's dashed  $A_a/A_t$  curve which starts to diverge from the isentropic ( $A_a/A^*$ ) curve at stage (c). At stage (d), the Mach number has been increased to the design Mach number and the weak shock becomes a strong curved shock. For the purpose of this discussion, this curved shock can be approximated to be a normal shock. The presence of this normal shock causes a non-isentropic flow which brings the velocity back to subsonic ahead of the inlet. Thus, spillage continues to occur and the flow entering the inlet is subsonic. This is obviously not desirable, because the total pressure of the intake air is lower in this case than for completely isentropic compression.

To start the inlet, a process of overspeeding must be employed at this stage. The inlet flow at stage (e) is increased to a speed just short of a specific overspeed Mach number  $M_o$ . This speed ( $M_o - dM$ ) causes the shock to move to the opening of the inlet. It can be noted that spillage is no longer occurring at the overspeed Mach number, although the flow is still brought down to subsonic speeds in the convergent portion of the inlet. At stage (e') the inlet is accelerated just above the overspeed Mach number ( $M_o + dM$ ). The area ratio for the detached shock is above that of  $A_i/A_t$ . Therefore, the shock is "swallowed" as it enters the convergent portion of the inlet. The shock cannot obtain a stable position in the convergent section of the inlet due to the fact that any small

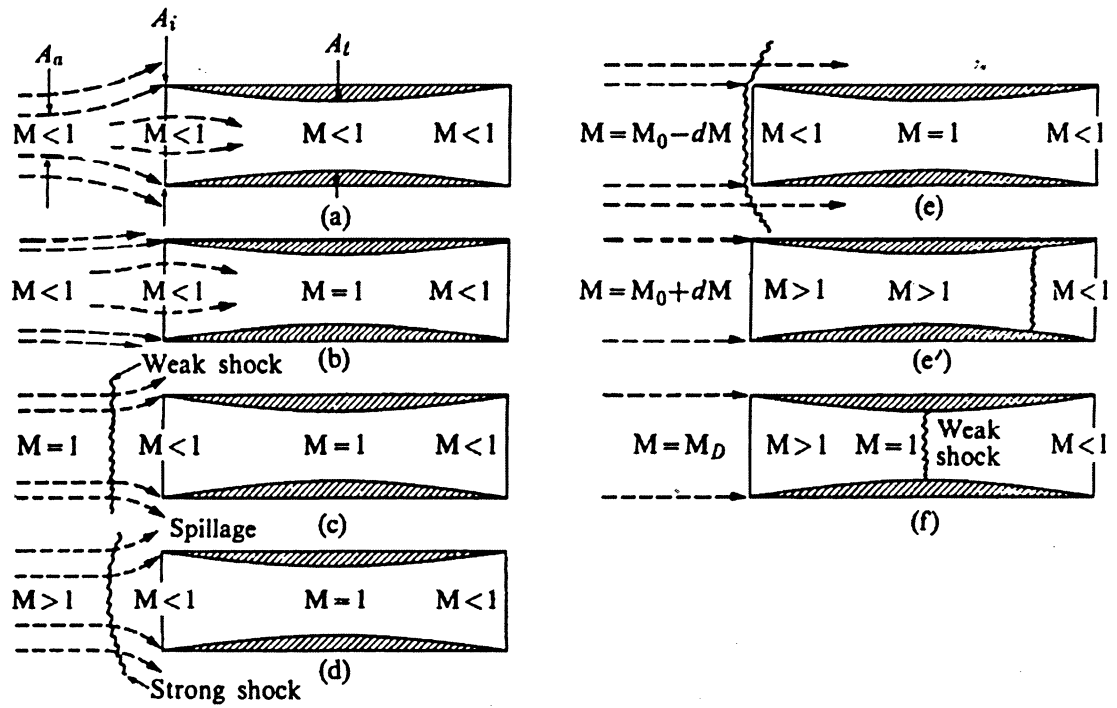


Figure 2: Inlet Starting Schematic: Acceleration and overspeeding [8].

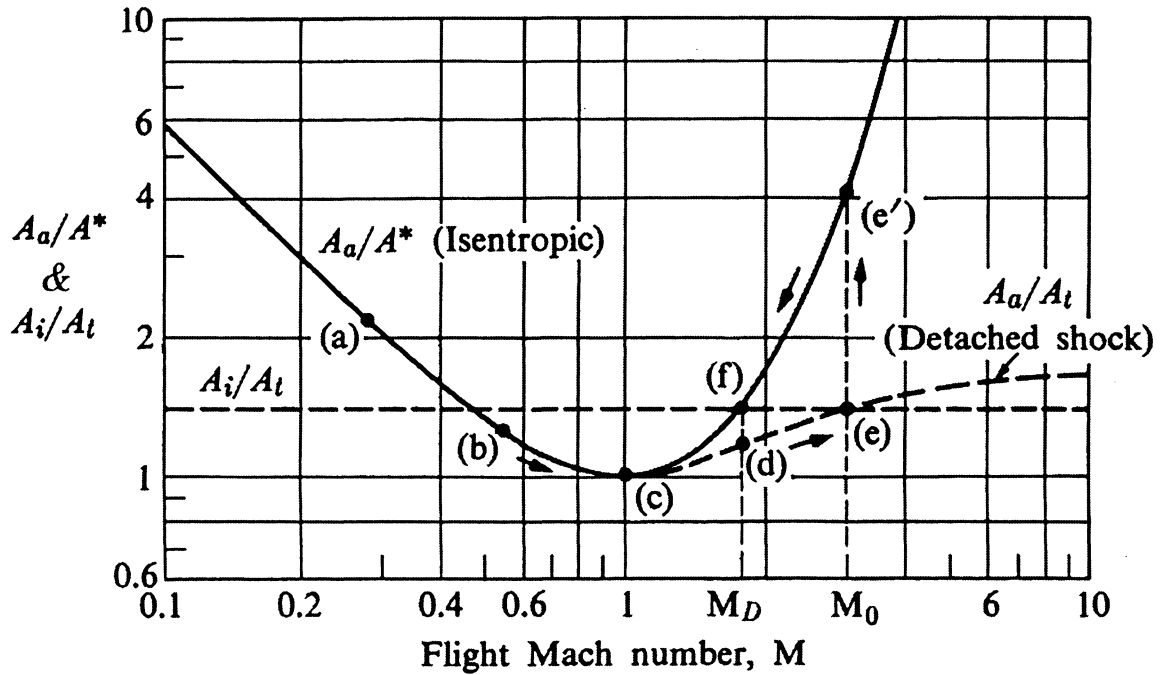


Figure 3: Inlet Starting Plot: Acceleration and Overspeeding, Plot for  $A_i/A_t = 1.5$  [8].

disturbance causes it either to back out the inlet or continue through the inlet until its swallowed. Since the shock enters the inlet by moving into it, it has to continue moving until it passes through the throat. It then finds a stable equilibrium downstream of the throat in the overspeed condition. At this point, the inlet can be decelerated back down to the design Mach number at stage (f) where the flow becomes isentropic, with a weak shock just downstream of the throat. Although overspeeding is a straightforward method of starting an inlet, it is often not practical, because it requires Mach numbers much higher than design speeds [8]. Another possibility for starting inlets would be to vary the contraction ratio by changing the throat area. This would require moving components to form a variable geometry inlet, thus increasing complexity, expense and decreasing reliability. This created a desire for other mechanisms of starting inlets, one of which is the use of perforations in the form of bleed holes or slots within the inlet itself.

### **1.3 BLEED FLOW SYSTEMS**

Before bleed systems were considered for use in inlet starting, they were employed on aircraft for the purpose of boundary layer control. This application of bleed systems is currently moving into the realm of hypersonics and seen in the research of Y.P. Goonko and I.I. Mazhul [6]. Their research focused on reducing the thick boundary layer which forms on a hypersonic aircraft forebody. This boundary layer is thick when entering the inlet due to frictional and compressive heating and can significantly reduce engine performance. Their research looked at the addition of a bleed wedge above the inlet of the aircraft. A bleed wedge is a sharp long body which effectively splits oncoming flow into two channels: the main flow channel and the bleed flow channel. Typically, it is placed just above the boundary layer that has developed along the body of the aircraft, such that the bleed flow channel captures the boundary layer and bleeds it away. This ensures that the boundary layer on the compression ramp of the inlet has to redevelop from the beginning, greatly reducing the boundary layer thickness within the inlet. Goonko and Mazhul found that a bleed system such as this can increase the mass flow into the engine by 5 to 11 percent depending on the Mach number. The boundary layer thickness was effectively reduced from 50% of the entrance height to 25%. Although this increased amount of air going into the inlet is beneficial to the propulsion

system, the bleed system itself caused a 5 to 12 % reduction in maximum L/D of the hypersonic aircraft [6]. This was due to the fact that the presence of the bleed wedge increased the overall aircraft drag. Goonko's research differed from this thesis because it looked at an external bleed system. Low-momentum boundary layer flow was bled away before entering the inlet, thus increasing the overall flow into the engine. Unfortunately, internal bleed systems such as the ones studied in this thesis have the reverse effect and reduce the amount of air that enters the combustion stages of a propulsion system.

A bleed system within an inlet allows the removal of necessary mass flow from the inlet to prevent spillage ahead of the intake. As flow is bled away from the intake, the detached shock seen in stage (d) of Figure 2 moves into the inlet. Many bleed holes are usually employed and the shock moves further back as the holes closer to the throat continue to bleed away mass flow downstream of the shock. Effectively, bleed perforations reduce the physical inlet area ratio of the inlet,  $A_i/A_t$ , so that the overspeed velocity needed to swallow the shock is reduced. With enough bleed holes, it is possible to eliminate any need for overspeeding whatsoever. This is known as self-starting. As early as 1962, experimental studies by Wu [22] were performed on perforated diffusers. It was found that the perforations (or bleed holes) can successfully aid the shock swallowing process. Wu employed Schlieren photography to study the presence of shockwaves inside the intake and found that the perforations created weak oblique disturbances which he determined to be Mach waves, although the main shock had been swallowed.

Numerical CFD methods have also been used to study this topic. CFD studies carried out by Tam *et al.* [20] looked at applying bleed holes to Busemann inlets. Their findings showed that bleed holes were successful in allowing inlets to self-start and that the efficiency of the bleed system can be increased by strategically placing holes based on the Kantrowitz limit. All these studies showed that bleed systems effectively removed sufficient mass flow from the inlet to allow shock swallowing. An unfortunate side effect of a bleed system is that it reduces maximum thrust possible at design conditions due to reduced mass flow. To reduce the impact of the bleed system at design conditions, Tam *et al.*'s implementation of the Kantrowitz limit reduced the amount of bleed flow necessary for shock swallowing. Arbitrary location of bleed holes caused a 31% loss of

mass flow, as opposed to 24% using the Kantrowitz limit [20]. This research shows that even an optimally designed bleed system can create significant reductions of airflow into the engine. Further improvements require bleed flow control, where the mass flow can be reduced even further once it is not needed at design conditions.

A thorough study of a bleed system requires experimental and analytical data of bleed flow performance for comparison. Harloff and Smith [7] studied different experimental setups such as bleed holes, plates and slots. They proposed analytical models to calculate sonic flow coefficients based on geometry and free stream flow conditions. An important aspect of their research, useful for this project, was the collection of numerous data and results for a wide ranging collection of experimental setups. These data were used for code and grid verification within this thesis.

## **1.4 MAGNETO-HYDRODYNAMICS & MAGNETO-AERODYNAMICS**

Although numerous works in the fields of magnetohydrodynamics (MHD) and magneto-aerodynamics have been published, most of the information is not relevant to this project. The publications largely deal with highly conducting fluids and ionized flows. Since this thesis deals with a weakly charged boundary layer, some concepts from these fields will be reviewed because analogies to statically charged boundary layers can be made. Furthermore, concepts can be borrowed for the development of charge generation and magnetic field body force simulation.

According to past research, only flows with non-negligible electrical conductivity will exhibit magnetic interactions. Although non-ionized air has a negligible conductivity, it can be ionized at high temperatures, or by injecting electron beams into the flow. At 3500 K, air's conductivity increases to 1 mho/m, and at 5000K to 40 mho/m. This compares to a value for sea water at 4 mho/m [11]. The field of MHD deals largely with the interactions of charged particles, and the magnetic fields that they generate through their motion, as well as forces created by externally applied magnetic fields. At higher temperatures, when the air's conductivity increases, the moving particles themselves will generate significant fields in which other charged particles will respond. This sets up a coupled dynamic system which is described by MHD theories [19]. Internal magnetic fields in an MHD system have their own behaviour and

governing equations. These systems exhibit magnetic waves, Alfvén waves, shocks, boundary layers, pressures, diffusion and other magnetic phenomena [19, 11]. In MHD systems, magnetic fields become yet another vector field that changes dynamically. Although these phenomena have analogies and similarities to those of normal compressible flows, there are interesting effects in magneto-aerodynamics such as wakes around an object moving in both downstream and upstream directions [11]. Since this thesis deals with weakly charged flows, which show no observable MHD effects due to their negligible conductivity, it can be concluded that any magnetic fields generated by these charged particles are negligible. This simplifies the system significantly, allowing for a simpler hypothetical formulation of applied forces due to an external magnetic field acting on statically charged particles within the boundary layer. One important concept that can be borrowed from the derivation of MHD formulations is the force that is generated by electric and magnetic fields. The force on a charge  $q$ , moving at velocity  $\vec{v}$ , exposed to magnetic and electric fields  $\vec{B}$  and  $\vec{E}$  is as follows [19]:

$$\vec{F} = q(\vec{E} + \vec{v} \times \vec{B}) \quad (2)$$

## 1.5 FLOW CONTROL SYSTEMS IN HIGH SPEED APPLICATIONS

Control methods similar to the one proposed in this thesis have been studied recently and are reviewed in this section. The difference between the study presented in this thesis and research done in the past is the magnitude of forces required to modify the flow. The literature review presented in this section deals with modifying large scale flows using magnetic fields, resulting in movement of large masses of air and repositioning of shockwaves. The electrical conductivity of air necessary for this kind of control is high, typically requiring ionization. This thesis, on the other hand, deals with modification of flows on the order of boundary layer thicknesses, requiring much weaker forces. It is hypothesized that the forces necessary to seal a bleed slot will be small enough that static charge buildup within the boundary layer will be sufficient and ionization will not be necessary. This is a new concept which has not received much attention in the scientific field, but looking at research that deals with large scale modifications of ionized flow can still be of value.

In 2001, Macheret *et al.*[13] did studies using magnetohydrodynamics (MHD) to try to control hypersonic flow outside of an inlet. In their research, cold air was ionized using electron beams, effectively increasing electrical conductivity. They proposed that the vector product of moving currents with magnetic field lines,  $\vec{j} \times \vec{B}$ , could create significant forces required by their research. Their numerical MHD codes coupled plasma kinetics, MHD equations and 2D inviscid flow equations. Figure 4 shows the schematic of their study. It depicts the forebody of a hypersonic aircraft ahead of an inlet. The oblique shocks are represented by thin solid lines and are generated by the forebody nose, transition ramp to the inlet, as well as the inlet entrance itself. The arrows show where e-beam guns inject electron beams, as well as the position of the magnetic field. The current density  $j_y$  and the magnetic field  $B_z$  are shown to generate a perpendicular force  $\vec{j} \times \vec{B}$ . The results of the study showed that such a system could modify a flow significantly so as to effect shock positions near the inlet. They found that a shock can be brought back to the cowl lip of the inlet even when an aircraft is flying at speeds higher than design [13].

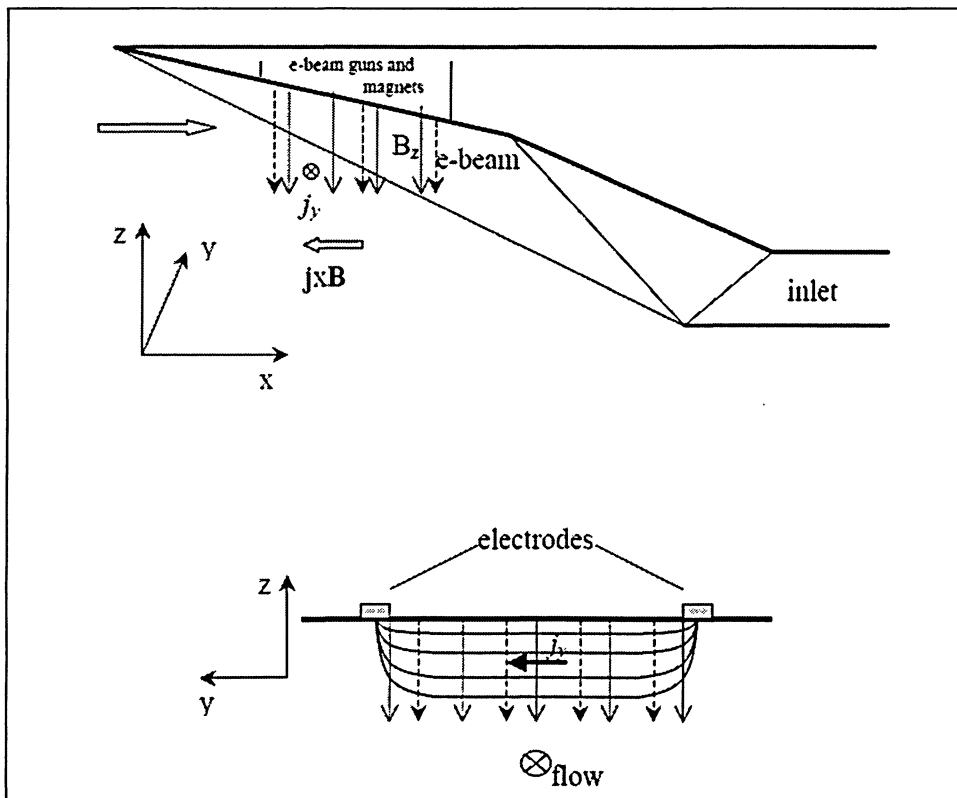


Figure 4: Schematic from Macheret research on MHD control [13]



Additional research published in 2002 by Macheret *et al.* [14] theoretically analyzed the effects of weakly ionized (cold) plasma under MHD conditions. A summary was made of current technological propositions in MHD technology such as drag reduction, thrust vectoring, sonic boom mitigation, boundary layer control and scramjet inlet control. One of the concerns that was mentioned regarding this technology was arcing that can occur between electrode segments, thus reducing the performance of a MHD system. Also noted were the high power inputs that are necessary with the use of electron beams (for ionizing cold flows) for any MHD effects to be significant. They looked at the strength of MHD effects in different scenarios and found that MHD lends itself mainly to modification of low speed core flows or flows within the boundary layers. They concluded that the MHD relative strength is higher in the near wall regions than in the core flows [14]. This research serves to validate the ideas within this thesis by showing that magnetic field effects can be observed in small scale flow modification cases. It can be also concluded that the effectiveness of such systems is a matter of scale, such that any over estimation in magnetic field control effects will only force the reduction in controllable bleed slot size. Since bleed systems are sized to match boundary layer thicknesses, it is possible that sufficient flow modification can be obtained on that scale.

Another interesting flow control system worth noting is using off-body energy addition. This system studied by Macheret *et al.* [12] has similar effects to that of the MHD control systems mentioned earlier. It was found that depositing energy (adding heat) upstream of a cowl lip on a hypersonic aircraft can have a significant impact on the increase of kinetic energy efficiency of an inlet. This is accomplished by increasing mass capture at off design conditions. To deposit energy, a circular-cylinder Gaussian heating profile was employed upstream and slightly below the inlet. Their study was numerical in nature so the heat addition was a theoretical construct, and physical mechanisms of heat delivery were suggested but not analyzed. Some suggestions included hot-air jets and plasma-controlled external combustion. The heat addition in this study resulted in an increase of inlet compression ratios by 15-20%. This increase was due the fact that the heated region resulted in gas expansion significant enough to cause deflection of the flow, so that it formed a virtual cowl extension. This resulted in a situation where the

oblique shock ahead of the inlet meets the lip of the virtual cowl, thus reducing spillage. [12]

The flow control systems mentioned above, all employ different mechanisms of adding energy or momentum to the flow. Similarly, it is possible to hypothesize that weakly charged boundary layers can be harnessed for the purpose of modification of bleed flows. The following section discusses static charge in boundary layers and the possible mechanisms by which they form.

## **1.6 STATIC CHARGE IN FLOWS**

Electrostatic charge buildup on surfaces due to contact with flow has been observed in numerous phenomena. Cases of aircraft electrification have been observed where movement of atmospheric air over the body of an aircraft can electrify its body and cause dangerous discharges. This implies that surfaces and possibly fluids become statically charged when high speed flow moves over a solid surface. Examples are not only limited to aircraft electrification. Explosions of supertankers have been noted in 1969, after cleaning them with high-velocity water jets [2]. It is reasonable to assume if a surface has been charged, then the boundary layer around that body will become statically charged at least partially as well.

In the case of aircraft electrification, often charge is transferred in collisions of aerosol particles with the aircraft body. The research of Chernyi in 1995 [3] has attempted to quantify the electrification currents for the purpose of predicting electrification rates. It was found that the current is approximately proportional to the aircraft velocity cubed and the surface area that the flow is exposed to [3]. By extension, it is reasonable to assume that, within high speed applications such as hypersonic inlets with long compression ramps, there would be a significant charge on the surface of the inlet due to aerosols, and similarly in the boundary layer. The presence of charged aerosols and particles within the boundary layer of the flow could be potentially used by forcing them to form ion-winds, hence adding momentum to the flow in desired directions. Ion-wind effects are body forces that add momentum to the flow. Although these momentum changes are not expected to be large enough for flow modification such

as the MHD applications mentioned previously, it is possible they can affect bleed flow on a small scale and hence control mass flow rates through the intake perforations.

## 1.7 SONIC FLOW COEFFICIENT

The sonic flow coefficient is a non-dimensional value defined as the ratio of mass flow rate through an actual perforation as compared to an ideal, isentropic converging-diverging nozzle with a throat area the same as the size of the perforation. This value is commonly used in the study of bleed systems as it gives the researcher immediate information about the performance of the bleed slot, whereas the value of mass flow rate does not. To calculate the sonic flow coefficient in any case, the quasi-one dimensional equations for compressible flow within nozzles were used [1].

The known values in the system are:

Total free stream pressure:	$p_o$ [Pa]
Total free stream temperature:	$T_o$ [K]
Specific heat ratio for air:	$\gamma = 1.4$
Gas constant for air:	$R = 287$ J/kgK
Throat area (assuming unit depth)	$A^* = 0.004399$ m <sup>2</sup>
Physical mass flow rate (from CFD)	$\dot{m}_{physical}$ [kg/s]

The total density is calculated using the ideal gas law:

$$\rho_o = \frac{p_o}{RT_o} \quad (3)$$

The density at sonic conditions (throat) denoted by superscript \* is obtained using:

$$\rho^* = \rho_o \left( \frac{2}{\gamma + 1} \right)^{\frac{\gamma}{\gamma - 1}} \quad (4)$$

The temperature at the throat is obtained similarly by:

$$T^* = T_o \left( \frac{2}{\gamma + 1} \right) \quad (5)$$

The speed of sound at the throat is calculated by:

$$a^* = \sqrt{\gamma R T^*} \quad (6)$$

Therefore the mass flow rate through an ideal nozzle at the throat is calculated using

$$\dot{m}_{ideal} = \rho^* A^* a^* \quad (7)$$

Once this is known, the value of mass flow rates in any physical system (such as ones obtained in this study) can be divided by the ideal flow rate to obtain the sonic flow coefficient.

$$Q = \frac{\dot{m}_{physical}}{\dot{m}_{ideal}} \quad (8)$$

To obtain these values repeatedly without need for manual recalculation, a MATLAB program was written, the source code of which is found in Appendix A. Mass flow rate, total free stream pressure and temperature were obtained from FLUENT after each CFD case and input into the MATLAB program. At this point, a value of Q could be obtained automatically.

## 1.8 BOUNDARY LAYER DISPLACEMENT THICKNESS

Within this research, it was known that displacement thickness will need to be calculated numerous times at a given point in the flow's boundary layer. This is because one of the studies performed within this thesis looked at the effects of boundary layer thickness on sonic flow coefficient. Different lengths of plate leading up to the bleed slot were used to generate different values of boundary layer thickness. There was no way to know the exact thickness before obtaining a CFD solution. Hence, a numerical integration procedure was employed to process the CFD results and report the required value of thickness.

Displacement thickness is defined as follows [18]:

$$\delta^* = \int_0^\delta \left( 1 - \frac{\rho u}{\rho_\infty U_\infty} \right) dy \quad (9)$$

Since this study deals with numerical values, the above equation was redefined in terms of discrete values that could be obtained from the FLUENT CFD solver.

$$\delta^* = \sum_{i=1}^N \left[ 1 - \frac{\left( \frac{\rho_i + \rho_{i-1}}{2} \right) \left( \frac{u_i + u_{i-1}}{2} \right)}{\rho_\infty U_\infty} \right] (y_i - y_{i-1}) \quad (10)$$

The MATLAB source code written to perform this calculation based on data extracted from FLUENT can be found in Appendix A.

## 1.9 THESIS OBJECTIVES

To control the amount of mass flow in a bleed system, a magneto-aerodynamic system is proposed in which magnetic fields are used to manipulate the weakly charged boundary layers and bleed flows. A numerical feasibility study was performed to determine the likelihood of magnetic fields having a significant impact on the amount of mass that is bled from the boundary layer. Since magnetic fields can be easily turned on and off at will, it is possible they could seal a bleed slot without requiring any moving mechanical parts. This would produce a system which is capable of swallowing a normal shock within the intake at off-design conditions and minimizing efficiency decrease due to bleed at design conditions.

The objectives of this thesis include the following:

- 1) Develop a numerical grid to model bleed flow within a 2D slot.
- 2) Modify the FLUENT solver through the use of user defined functions to simulate static charge generation in the boundary layer.
- 3) Introduce the influence of magnetic fields on the flow by adding source terms to the momentum equations through the use of user defined functions.
- 4) Determine the feasibility of a magneto-aerodynamic bleed control system by observing the conditions under which such a system can function.
- 5) Observe and summarize the variation of specific system parameters such as Mach number and geometry and its influence on the control system.

## **1.10 THESIS SUMMARY – CHAPTER LIST**

The following section outlines the scope of each thesis chapter to help present the ideas from this research in an organized fashion.

Chapter 1 introduced the concepts of high speed propulsion and in particular discussed the difficulties of starting high speed inlets. Furthermore, a review of bleed systems for the purpose of inlet starting was summarized. Finally, a bleed flow control system was proposed using the concept of a weakly charged boundary layer being manipulated by magnetic fields.

Chapter 2 will attempt to outline some of the assumptions and resulting limitations of this research to help place the numerical studies in proper context.

Chapter 3 will discuss the techniques employed in generating the computational domain and resulting grid. Failed attempts at hybrid grid generation will be briefly described and the final resulting structured grid will be described in detail.

Chapter 4 will outline the FLUENT CFD solver used, as well as describe how the cases were set up in detail. Boundary conditions and initial conditions, as well as discussion on solution accuracy, will be discussed in this chapter.

Chapter 5 will present the modifications made to FLUENT by adding a transport equation which simulates charge generation, as well as the addition of source terms to the momentum equations for magnetic field body force simulation.

Chapter 6 is a collection of all the results obtained within this thesis. It starts with code verification and grid independence studies, and continues on to summarize how the magneto-aerodynamic bleed control system behaves under the variation of parameters such as Mach number, pressure ratios, displacement thickness, as well as magnetic field strength and position.

Chapter 7 concludes this thesis by presenting possible paths that can be taken to further this research,



## **CHAPTER 2: RESEARCH SCOPE**

### **2.0 RESEARCH PREPARATION**

The research presented in this thesis is a numerical feasibility study of a previously unexplored bleed flow control system. Due to the nature of a feasibility study, certain assumptions have been made to facilitate the research process. This implies that this research has certain limitations which must be identified at the outset of the process. The following sections take time to identify the purpose of this research, as well as outline the assumptions made and resulting limitations.

#### **2.1 ASSUMPTIONS**

The following is a list of assumptions that were made within the study.

- 1) The Mach number is not high enough (temperatures not high enough) for ionization of air by dissociation.
- 2) Any charge generation that occurs within the system is a static charge, which occurs within the boundary layer. It is assumed this happens through flow interaction with the wall surface and through intense shear acting on aerosol particles within the boundary layer. If this phenomenon does not produce a significant charge, an external source of charge may be introduced to the flow (eg. Localized ionization, electron beams, etc).



- 3) Diffusion of charge within the flow is negligible, and any diffusion present in the simulations is imposed solely for the purpose of CFD solution stability. Although this assumption may not precisely reflect reality, it was decided that, with the lack of experimental data to show the behaviour of diffusion of static charge, it is more appropriate to reduce diffusion effects than blindly represent them.
- 4) Any constants within the charge generation equations have not been precisely determined and have been only set according to “constant-independence” criterion required by the study. Constant-independence means that the constants in the charge generation equations could change without affecting the validity of conclusions made in this thesis. This will be discussed further in the results section of this thesis.
- 5) The moving charged particles within the flow produce very weak magnetic fields. It was assumed that any externally applied magnetic field will be significantly stronger than the weak magnetic forces generated by moving charged particles.
- 6) The following typical CFD assumptions based on FLUENT settings were made for air:
  - a. Air behaved as an ideal gas, governed by the equation of state [9]:

$$e_t = \frac{a^2}{\gamma(\gamma-1)} + \frac{1}{2}(u^2 + v^2) \quad (11)$$

Specifically within FLUENT, the following form of the ideal gas law is used in compressible flows [4]:

$$\rho = \frac{p}{\frac{R}{M_w} T} \quad (12)$$

- b. Viscosity is governed by the Sutherland Law [21]

$$\frac{\mu}{\mu_o} \approx \left( \frac{T}{T_o} \right)^{3/2} \left( \frac{T_o + S}{T + S} \right) \quad (13)$$

where T is temperature in Kelvin,  $\mu$  is viscosity in kg/ms

and  $T_o = 273$  K,  $\mu_o = 1.75 \times 10^{-5}$  kg/ms,  $S_{air} \approx 110.4$  K

c. The following properties were fixed (set as default within FLUENT)

- i.  $C_p$  (J/kgK) = 1006.43
- ii. Thermal Conductivity (W/mK) = 0.0242
- iii. Molecular Weight (kg/kmol) = 28.966
- iv. UDS (Charge Density) Diffusivity (kg/ms) = 0.01

## 2.2 LIMITATIONS

The assumptions outlined in the previous section impose certain limitations to the applicability of this research. These limitations include:

- 1) A complete design of a bleed system cannot be accomplished by the results of this thesis alone.
- 2) This thesis is used to determine the feasibility of the magneto-aerodynamic concept.
- 3) The shape and generation of the magnetic field was not studied. Modified field shape may improve performance.
- 4) The simulation does not take into account the mechanisms of how the charge is generated or effects of internally generated magnetic field forces. Therefore, charge generation is not modeled exactly, neither is charge diffusion.
- 5) This study is limited to 2D cases only.

Although these limitations exist, the research presented within this thesis shows insight into the aerodynamic behaviour of potential bleed control systems and displays trends which are likely to exist in more comprehensive numerical studies, as well as experimental setups.



## **CHAPTER 3: COMPUTATIONAL DOMAIN AND GRID**

### **3.0 GRID GENERATION**

To begin the study, first a numerical 2D grid had to be developed for the FLUENT CFD solver used in this research. The Gambit software package by FLUENT Inc. was used to perform the work. There are many aspects of grid generation that had to be taken into account when designing a grid to ensure a certain degree of solution accuracy. The following sections will describe some of the issues that were encountered while designing the grid.

#### **3.1 INTRODUCTION TO THE GAMBIT SOFTWARE PACKAGE**

The grid generation software used was FLUENT Inc.'s Gambit 2.2.30. Gambit (screenshot shown in Figure 5) is a geometry and grid generation package that allows the user to work at a high or low level. It has built-in geometrical primitives, 2D and 3D generation tools and other high level functions, but also allows the generation of custom geometries through the use of lower level tools such as vertex, edge, face and volume generation. The research in this thesis dealt with large domains that had simple tetrahedral shapes (See Domain Breakdown Figure 6) of which the vertex locations had

been pre-calculated based on bleed slot geometry. The low level tools were used to generate the domain. Vertices were first created and then joined to form edges. These edges were then used to define the faces (or 2D domain sections) used for meshing.

Meshing in Gambit is handled by tools which enable a user to mesh edges and faces with custom parameters such as grid spacing, successive ratio of grid spacing growth, off wall spacing, boundary layer tools and other useful functions. It offers the option of meshing faces using numerous structured and unstructured schemes, and allowing hybrid meshes as well. The following sections will outline the process that took a geometry design to a fully developed numerical grid.

One downside to using FLUENT Inc.'s grid generator and solver is the lack of advanced mesh smoothing routines which would greatly improve grid quality.

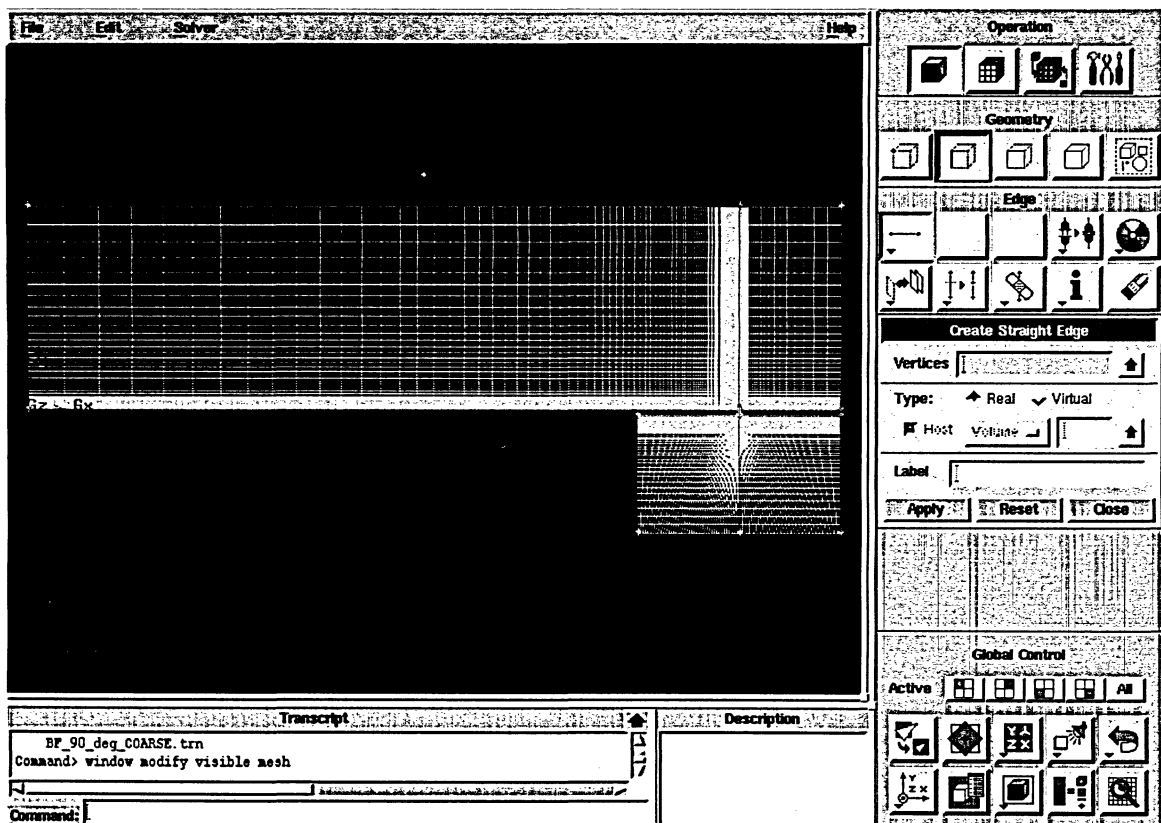


Figure 5: Gambit 2.2.30 Software Package

### 3.2 DOMAIN AND GEOMETRY

The primary bleed slot geometry studied in this research was a 90 degree bleed slot, perpendicular to the main flow. The computational domain was divided into 3 zones: a flat plate with uniform flow above it (Flow Field), the bleed slot, and a plenum beneath. Each was divided into sub-domains (Seen in Figure 6). The Flow Field was divided into 4 sections: Upstream, Downstream, Boundary Layer Left (of the slot) and Boundary Layer Right. The Hole was divided into 2 sections, Hole Left and Hole Right. The Plenum was divided up similarly to the Flow Field. It had 4 sections labeled as Plenum Left, Plenum Right, Plenum Boundary Layer Left, and Plenum Boundary Layer right. Dividing the domain into the subsections outlined above allowed precise control of grid spacing within the boundary layer close to the walls, within the bleed slot, and at the domain far field extents. This was done so that grid spacing could be kept tight near the walls and inside the hole, but allowed the use of a coarse mesh out near the farfield and pressure outlets within the plenum.

Another benefit to dividing the domain into unique zones, is that it allowed the possibility for initializing each zone with different values at the beginning of a CFD solution procedure.

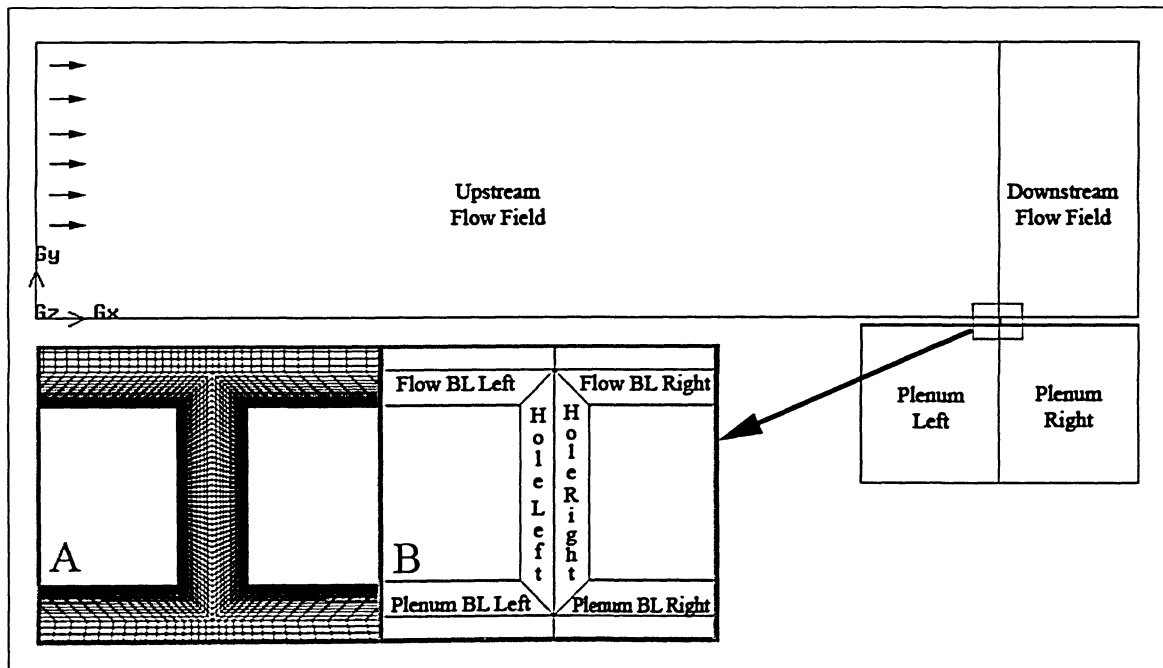


Figure 6: Domain Breakdown Diagram (B) and Resulting Grid (A)

The domain extents were chosen to be significantly far away from the bleed slots so that their influence on bleed results would be negligible. Although the flow is largely supersonic, disturbances can still propagate upstream through the subsonic boundary layers. The upstream flow field boundary was 1.75 m ahead of the bleed slot centre line, although this value changed for the study of boundary layer displacement thickness effects. The downstream flow field boundary was 0.25 m behind the bleed slot centerline. The pressure far field boundary above the bleed slot was 0.5 m above the entrance to the bleed slot. The plenum was 0.5 m wide and the bottom boundary was located 0.3 m below the bleed slot entrance.

### **3.3 MESHING TECHNIQUES**

Gambit offered the use of structured and unstructured quadrilateral elements or unstructured triangular elements for the purpose of meshing the domain. Both were considered as potential discretizations. The trials and resulting mesh are explored in the following sections.

#### **3.3.1 HYBRID MESHES**

The domain had been initially discretized using a hybrid mesh. A structured grid was applied to off wall regions to resolve the boundary layer and an unstructured grid was applied everywhere else. The benefit of using unstructured triangular elements was that the grid smoothness could be controlled very well within the unstructured region. Furthermore, it avoided the high aspect ratio cells in unwanted areas (where flow direction would be oblique to the cell alignment). A sample of a hybrid mesh can be seen in Figure 7 and in general worked well, except for a few limitations which would prove unacceptable. First of all, it would not allow the FLUENT solver to work with second order upwinding schemes for the flow and turbulence models due to spurious oscillations. Furthermore, transition from structured to unstructured cells was not always smooth, as seen in Figure 7, due to the small off wall spacing of the structured region and the coarseness of the triangular elements adjacent to it.

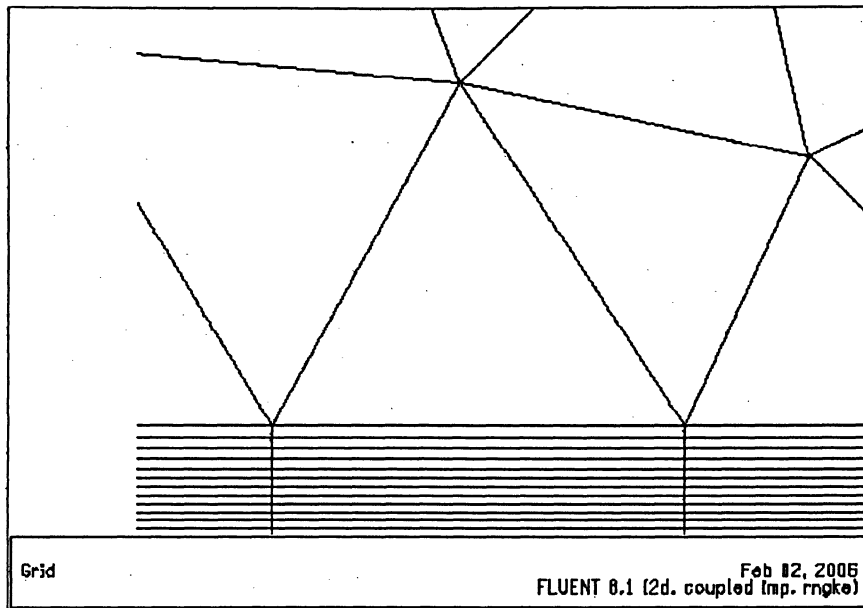


Figure 7: Hybrid Mesh Interface near Boundary Layer

In CFD computations, the Navier-Stokes equations are modified from their integral forms to work with a discretized domain. Since this process only approximates the actual equations, truncation errors are present in any CFD solution. This truncation error is significant whenever the aspect ratios of adjacent cells are very dissimilar. In the above Figure 7, it can be seen that, although the growth of the structured cells within the boundary layer is smooth, an intense discontinuity is encountered when the unstructured region is reached. Since this study deals with flows and charge generation that depend heavily on flows within a boundary layer, discontinuities so close to the boundary layer are not acceptable.

### 3.3.2 STRUCTURED MESHES

To avoid the problems mentioned with Hybrid Meshes, a second grid was designed which was entirely structured. Its design allowed the use of second order upwinding schemes and increased grid smoothness significantly. The main feature of this grid, versus ones that had been tried initially, is that the tight boundary layer spacing follows the walls only and did not cause any tight spacing or high aspect ratio cells near the domain extents (specifically in the plenum). The boundary layer grid (tightly spaced cells) can be seen wrapping around the corners in Figure 8. Also, the grid's relationship



to the domain breakdown can be seen in Figure 6. Close-up A shows the grid near the slot, and close-up B shows the labeled domain breakdown near the slot.

### 3.4 IMPORTANT NOTES ON THE FINAL GRID

The grid was designed to make sure that it sufficiently resolves the boundary layers and captures the unique features of a bleed flow system. One of the most important aspects of resolving the boundary layer and other features was to have a very small off wall spacing. Within this study, the off wall spacing was 0.01 mm (0.2% of bleed slot diameter). This was used to ensure that the grid satisfied the requirements of the turbulence model. The maximum growth factor used in successive cell sizes was 1.12. Data in Table 1 is a compilation of specifications used in the generation of the above mentioned grids. It outlines the number of intervals on each edge as well as the node distribution. Figure 9 and Table 1 have can be cross referenced through the use of lower case letters. Figure 10 shows the complete resulting grid within the domain.

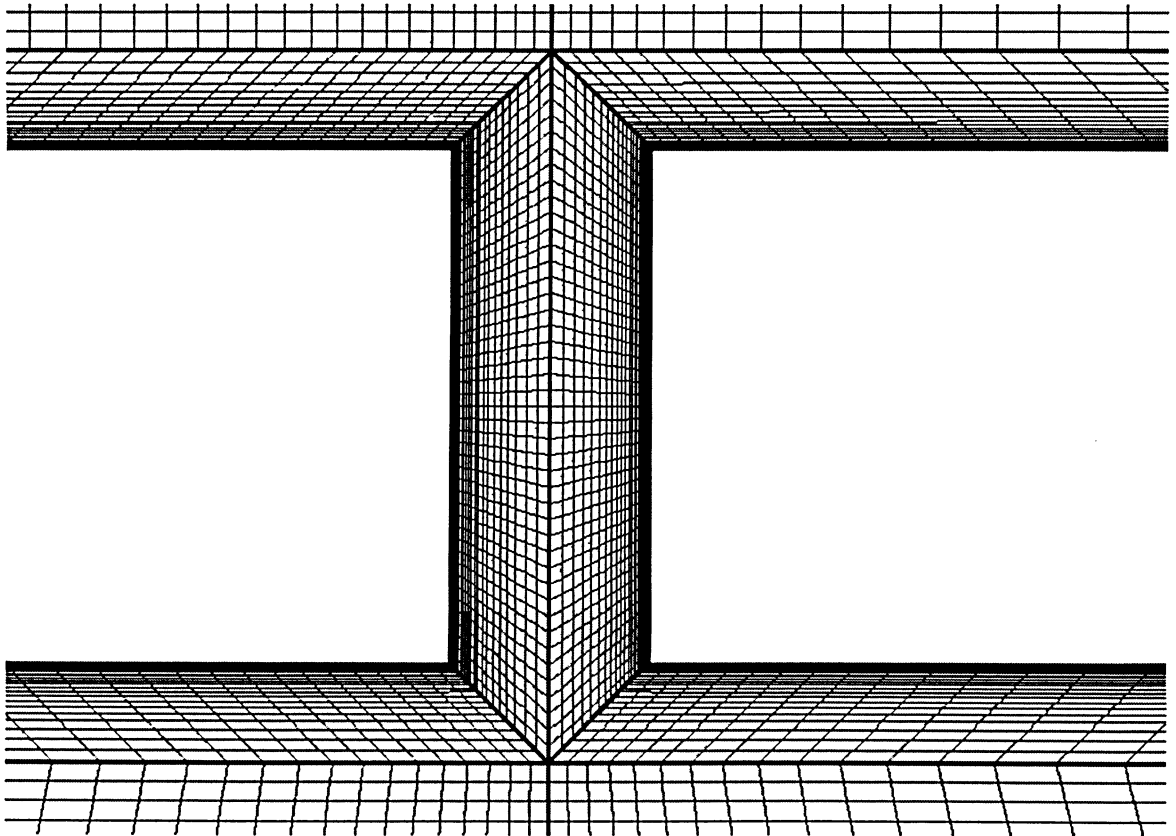


Figure 8: Grid close up of hole region created in GAMBIT

EDGE INDEX	a	b, f	c	d	e	g	h	i
# OF INTERVALS	144	44	68	29	44	58	58	44
NODE DISTRIBUTION SPECIFICATION	Near Slot Spacing =0.4mm	Near Slot Spacing =0.4mm	Near Slot Spacing =0.4mm	Near Wall Spacing =0.01mm	Equal Spacing	Near Slot Spacing =0.4mm	Equal Spacing	Equal Spacing

Table 1: Edge Meshing Data: Number of Intervals (Nodes - 1) on Edge

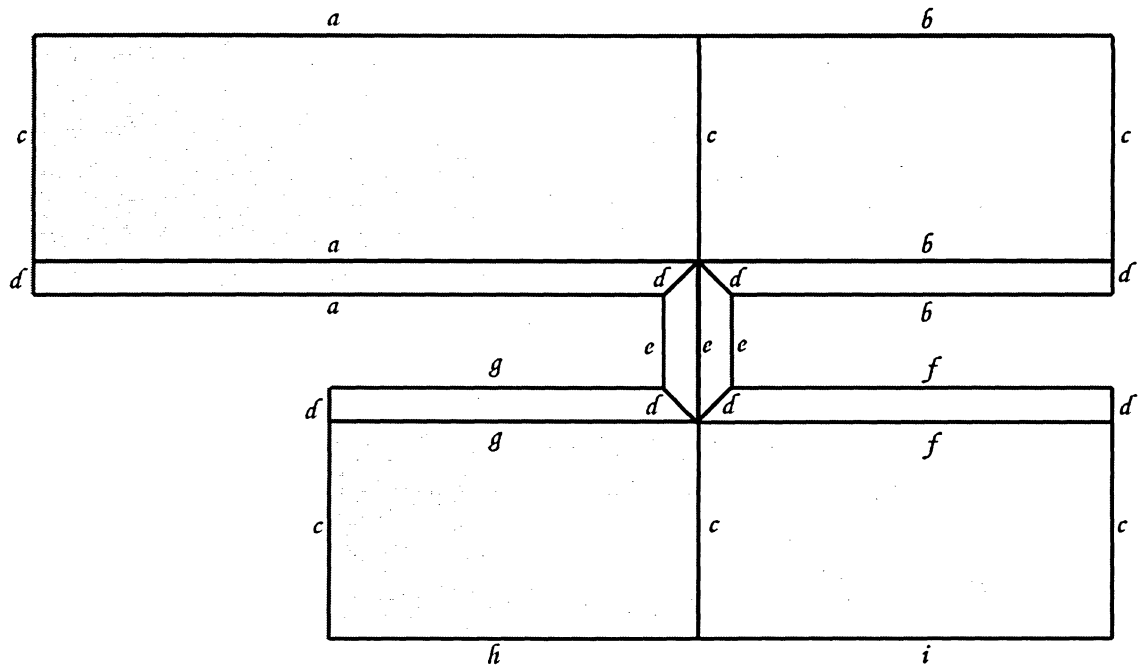


Figure 9: Visual Reference for Edge Meshing Data

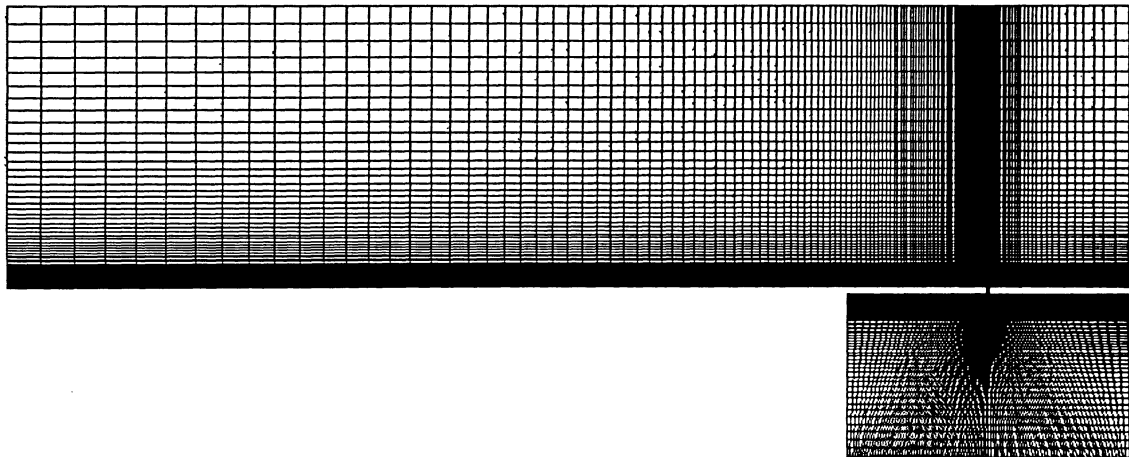


Figure 10: Final Computational Grid created in GAMBIT



## **CHAPTER 4: COMPUTATION FLUID DYNAMICS – SIMULATING COMPRESSIBLE FLOW**

### **4.0 COMPUTATIONAL FLUID DYNAMICS PROCESS OVERVIEW**

Computational Fluid Dynamics (CFD) is a numerical solution process beginning with the discretization of a physical geometry/domain. Once a domain is discretized, an iterative solution of the discrete Navier Stokes equations can be performed on the individual control volumes that arise from the meshing process. Navier Stokes equations include momentum conservation, energy conservation, and continuity. In addition, turbulence equations can be solved if needed. In this thesis, a one equation turbulence model was used. To perform the CFD analysis in this thesis, the spatial discretization was performed in the GAMBIT package as described in the previous chapter. To solve the Navier Stokes equations, the FLUENT software package was used and is described briefly below.

### **4.1 INTRODUCTION TO THE FLUENT SOFTWARE PACKAGE**

FLUENT 6.2.16 used in this thesis, is a high end commercial CFD package developed by FLUENT INC. It has the capability of running steady state as well as transient solutions. It offers segregated and coupled solution schemes, with options of implicit and explicit formulations for the coupled solver. FLUENT is capable of handling both 2D planar, 2D axisymmetric and 3D grids. On top of its basic solvers, it

has the capacity of handling multi-phase flows and dynamic meshes. FLUENT also has powerful post-processing tools, allowing the plotting of contours, vectors, streamlines, transient animations and X-Y data plots along user defined surfaces.

The most important feature of FLUENT that was useful within this thesis was the ability to handle user defined functions (UDFs). UDFs expand FLUENT's potential to limitless possibilities. They allow the user to add extra equations to be solved, as well as modify existing Navier-Stokes equations by specifying source terms. This feature was of great importance within this thesis, by expanding FLUENT's capabilities to handle charge generation and magnetic field body forces. UDFs and an in depth application of their use within this research is discussed in Chapter 5.

## **4.2 SOLUTION/SOLVER CONTROL**

This thesis used FLUENT's coupled – implicit formulation. Coupling was required due to the high speed nature of the flows. Since this was a highly compressible supersonic flow with significant density variation, the coupled formulation was appropriate. Furthermore, the implicit formulation was used to increase the convergence rate of the solver. An explicit formulation was available but was not used since the small off wall spacing would have required very small time steps (Courant numbers) to maintain numerical stability. A Courant number of 0.1 was used right after solution initialization and increased to 1 over several hundred iterations (actual number of iterations depending on the case).

The Navier Stokes and modified turbulent viscosity equations were set to use second order upwind discretization. This ensured higher accuracy than first order at the cost of convergence speed. The additional transport equation (charge per unit mass generation equation) added through the user defined scalar (UDS) function was set to a first order upwind discretization. Although not as accurate as a second order formulation, it was necessary due to instabilities that arose. When a second order upwind setting was used, the values of charge per unit mass within the boundary layer and plenum would appear negative in certain regions due to erroneous oscillations. Since this was not possible according to the charge generation equations developed, the negative values must have been a result of numerical error. This was addressed by resetting the UDS

equation discretization back to first order. A detailed specification of all FLUENT settings is found in Appendix B.

### 4.3 TURBULENCE MODELS TESTED

Due to the fact that the bleed slot size was on the order of the boundary layer displacement thickness, only turbulence models with enhanced wall treatment were considered for these simulations. First, the two equation RNG k- $\epsilon$  turbulence model with enhanced wall treatment was used to model viscous effects. A steady state solution procedure using the RNG k- $\epsilon$  model did yield a converged mass flow rate within the bleed slot. Although a converged mass flow was obtained, the plenum flow field would not converge to a steady state solution. Switching to a transient analysis, it was found that the jet emerging from the bleed slot into the plenum was causing transients such as vortex shedding. The transient analysis did indicate that, over time, the solution within the plenum does indeed tend towards a steady state. Finally, the one-equation Spalart Allmaras (SA) turbulence model was chosen for use in this study. The speed increase of using a single equation model was not the only benefit to using the SA model. More importantly, it was found that a steady state solution within the plenum could be obtained without using an intermediate transient solution procedure. A pre-requisite for using the SA model is that the  $Y^+$  of the first off-wall node has to be within the viscous sub-layer. This means that any value of  $Y^+$  on the order of 1 is acceptable [4]. After obtaining the solution with the redesigned structured grid, the  $Y^+$  values along the majority of the wall sections were less than 4 and therefore acceptable for use with the SA model. (See Figure 11).

Furthermore, it was found that the mass flow rate solutions obtained from the k- $\epsilon$  and SA turbulence models differed by only 0.1%. The SA model has also been verified by Paciorri *et al.* [17] for use in applications such as hypersonic flows and, since this study deals primarily with high speed flows, their results, conclusions and validations were found to be relevant.

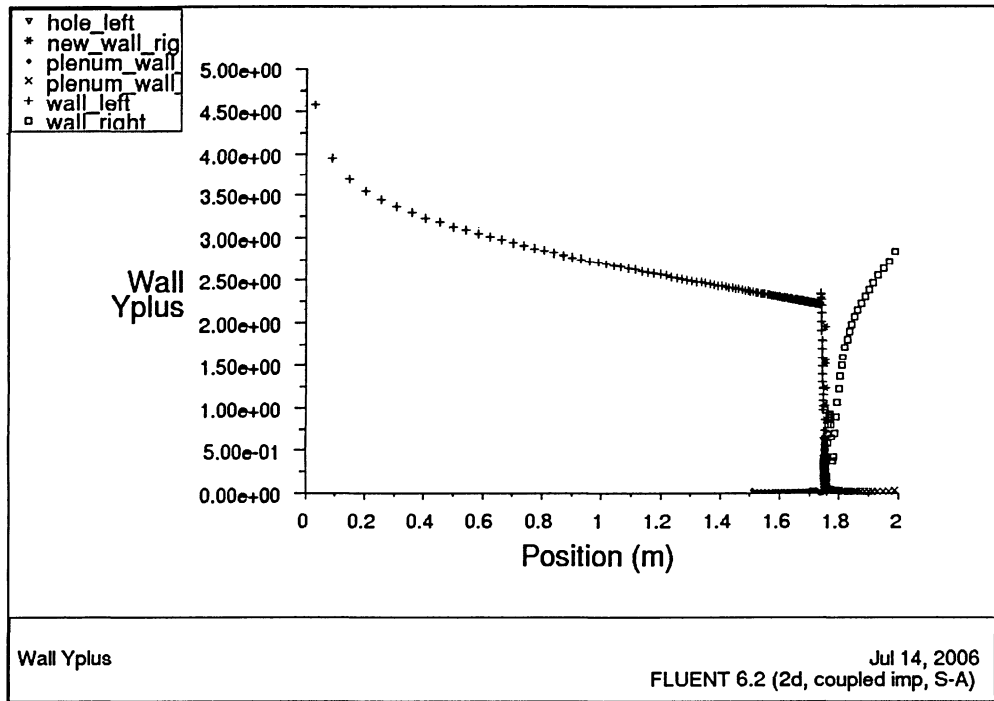


Figure 11: Y+ on Geometry Walls: Turbulence Model Compliance

#### 4.4 BOUNDARY CONDITIONS AND INITIAL CONDITIONS

The boundary conditions used in this study are summarized in Table 2 and can be cross referenced with Figure 12 for clarity.

For any CFD computations, initial conditions must be specified within the domain. Although simply filling the domain with null values should have still yielded a converged solution, a simple initial condition closer to reality was imposed to increase convergence speed. The flow field region above the bleed slot was filled with uniform flow at the Mach number and pressure equaling that of the pressure farfield conditions. This meant that with the exception of the boundary layer, and near slot regions where shocks are present, the flow field would start close to its converged solution.

The slot and plenum regions were initialized with zero velocity and the plenum pressure, as defined in pressure outlet (#4) in Table 2. This would generate an initial state with a pressure imbalance between the slot and the flow field above ( $P_{\text{PLENUM}}/P_{\text{FREESTREAM}}=0.1$ ), hence driving the flow into the slot within very few iterations.

BOUNDARY CONDITION INDEX	BOUNDARY CONDITION TYPE	APPLICATION	TYPICAL VALUES (SOME VALUES VARIED DEPENDING ON CASE)	CHARGE GENERATION (UDF) CONDITION
#1	Pressure Far Field	Inflow in Flow Field Region	Mach Number: 1.97 Pressure: 101325 Pa Temperature: 300 K	Constant Value (0)
#2	Pressure Far Field	Top of flow in Flow Field Region	Mach Number: 1.97 Pressure: 101325 Pa Temperature: 300 K	Constant Flux
#3	Pressure Outlet	Outflow in Flow Field Region	Pressure: 101325 Pa	Constant Flux
#4	Pressure Outlet	All Plenum Domain Extents	Pressure 10132.5 Pa	Constant Flux
#5	Wall (No Slip)	All Wall Sections	N/A	N/A

Table 2: Boundary Conditions

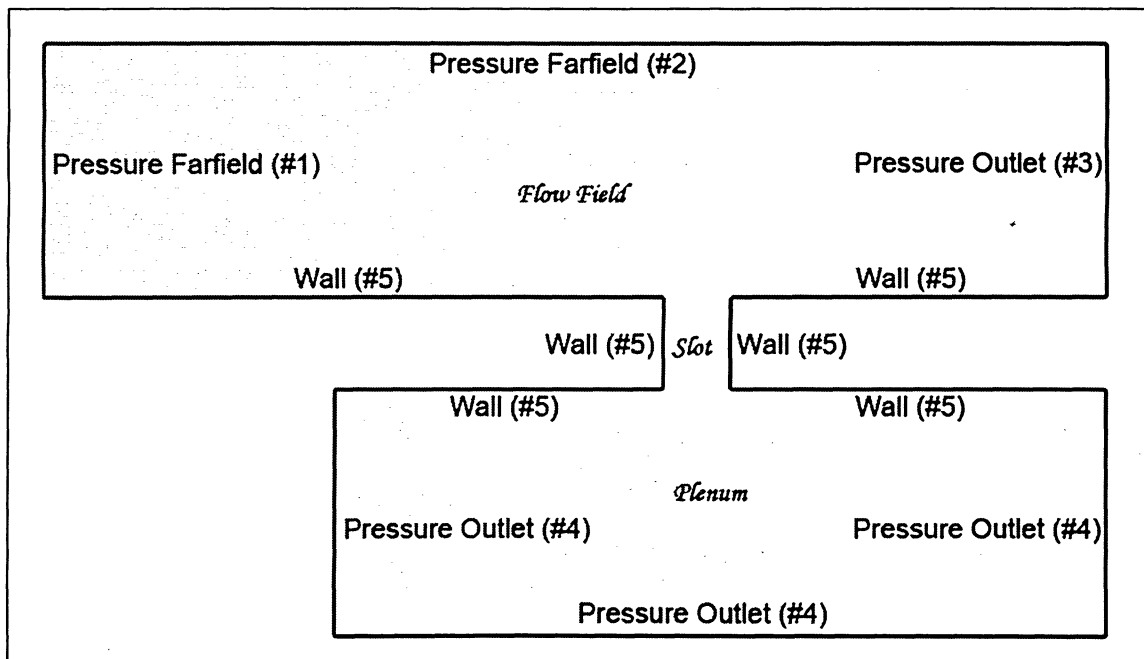


Figure 12: Boundary Condition Application Diagram (Schematic not to scale)



For numerous cases that had identical geometry, a previously solved (converged) solution was used as an initial condition for the current case (since changes were expected to be fairly small between cases). This procedure was used when only charge generation equation constants were varied and magnetic field strength and location changed. This method was also used if only the boundary conditions changed. For example, if from one case to the other the  $P_{\text{PLENUM}}/P_{\text{FREESTREAM}}$  ratio changed, only the plenum pressure outlet boundary condition would have to be modified. This meant that the flow field would be very similar to the previous case, and the previous solution can be used as an initial condition for the current case.

#### 4.5 NOTES ON SOLUTION ACCURACY

To ensure proper convergence and a degree of solution accuracy, a number of parameters were assessed. First, the residuals were monitored and were used to determine whether the solution appeared to be converging. The monitored residuals of Figure 13 and their corresponding equations were as follows:

- 1) X-Velocity (X-Momentum Equation)
- 2) Y-Velocity (Y-Momentum Equation)
- 3) Continuity (Mass Conservation Equation)
- 4) Energy (Energy Equation)
- 5) Nut ( $\mu_T$ , Turbulent Viscosity for Spalart Allmaras Turbulence Model)
- 6) Uds-0 (User Defined Scalar , Charge Per Unit Mass Transport Equation)

Solutions were typically run until the residuals would not drop any further and would start to oscillate. Convergence was considered successful when the residuals would flat line or oscillate below a value of  $10^{-3}$ . This can be seen in Figure 13.

To get a more accurate sense of convergence, bleed mass flow through the slot was monitored. A figure showing the mass flow rate monitor can be seen in Figure 14. A line (surface) was created within FLUENT at  $-5.6 \times 10^{-3}$  m from the top of the slot (approximately half way through the slot). FLUENT could then automatically integrate the flow variables across this surface and compute a mass flow rate.

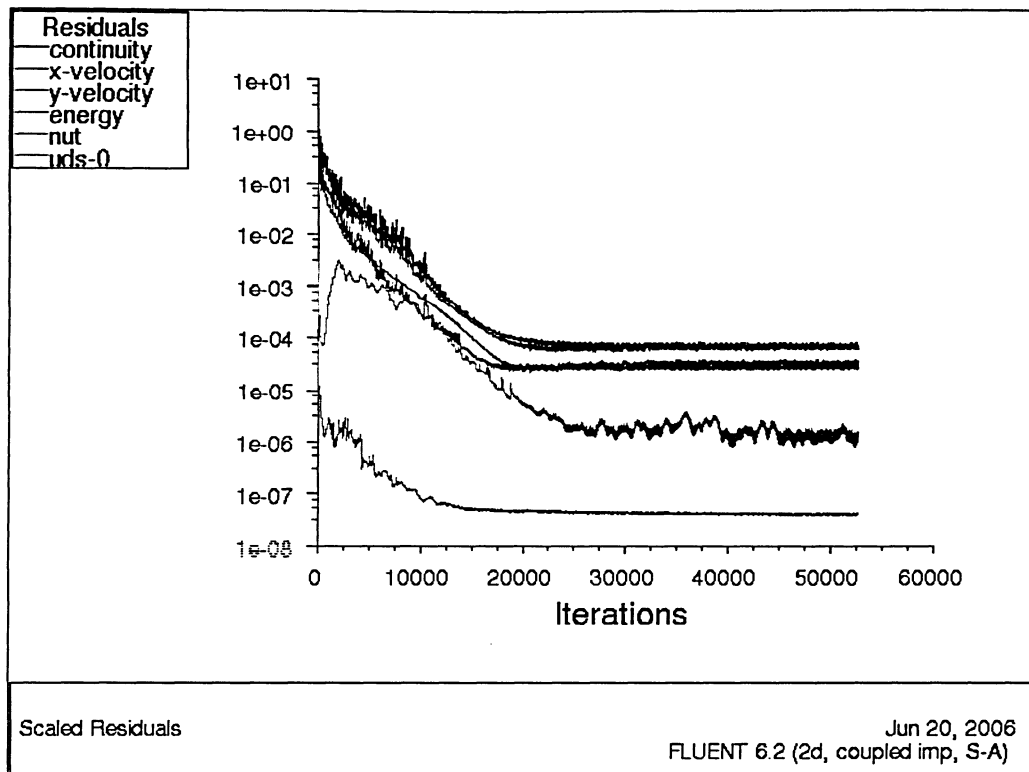


Figure 13: Residual Convergence Plot

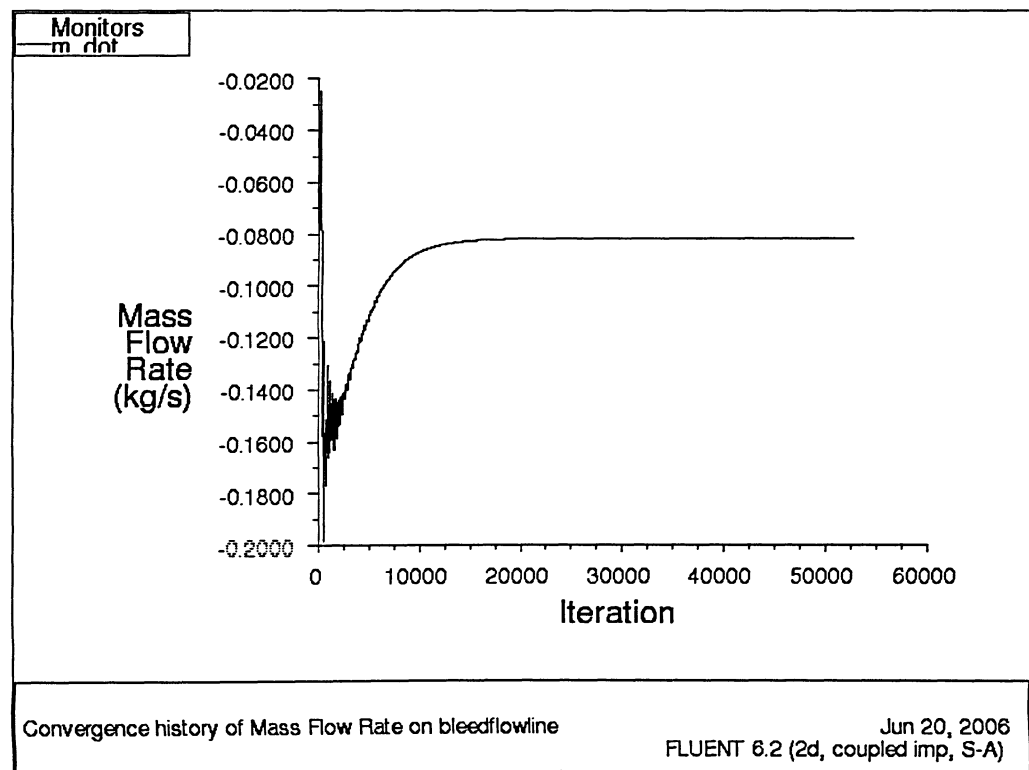


Figure 14: Mass Flow Rate Convergence Plot

The value of mass flow rate in each iteration was then written to a file and plotted on a monitor on an ongoing basis. These values were observed, and a solution was considered converged when the mass flow rate would be determined to 3 significant digits. Although occasional cases would not converge to 3 significant digits and would show oscillatory behaviour, the mean value of mass flow and the range of its oscillation were recorded and documented.

#### 4.5.1 RICHARDSON'S EXTRAPOLATION

Numerical accuracy not only depends on the converged values but on the quality of the grid. In any numerical study, a grid independence assessment should be performed to ensure that the values obtained in the research do not change significantly with grid size (number of cells and node spacing). The process of determining grid independence involved generating numerous grids of different sizes and obtaining solutions from each. Then, with increasing number of nodes, the values should appear to converge on a single value. Since often it is computationally too expensive to generate the final grid which would show a completely grid converged solution, a process known as Richardson's extrapolation was employed. It takes values from a series of known solutions at different grid refinements and extrapolates what the grid converged value is likely to be. Richardson's extrapolation in this thesis was performed according to the "Statement on the Control of Numerical Accuracy" within the editorial policy of the *Journal of Fluids Engineering* [16].

The first step in performing Richardson's extrapolation is to calculate the average grid size,  $h_g$ . In a 2D domain, it is done as follows:

$$h_g = \left[ \frac{1}{N} \sum_{i=1}^N (A_i) \right]^{1/2} \quad (14)$$

where  $N$  is the total number of cells,  $A_i$  is the area of the  $i^{\text{th}}$  cell. Once this is calculated for 3 successive grid refinements  $h_{g1}$ ,  $h_{g2}$ ,  $h_{g3}$  where  $h_{g1} < h_{g2} < h_{g3}$ , two grid refinement factors have to be calculated such that  $r = h_{g\_coarse}/h_{g\_fine}$ .

$$r_{21}=h_{g2}/h_{g1} \quad \text{and} \quad r_{32}=h_{g3}/h_{g2} \quad (15)$$

At this point, the apparent order of convergence  $p$  has to be calculated:

$$p = \frac{1}{\ln(r_{21})} \left| \ln \left| \frac{\dot{m}_3 - \dot{m}_2}{\dot{m}_2 - \dot{m}_1} \right| + q(p) \right| \quad (16)$$

$$q(p) = \ln \left( \frac{r_{21}^p - s}{r_{31}^p - s} \right) \quad (17)$$

$$s = 1 \cdot \text{sign} \left( \frac{\dot{m}_3 - \dot{m}_2}{\dot{m}_2 - \dot{m}_1} \right) \quad (18)$$

where  $\dot{m}$  was the mass flow rate computed by the respective grid.

This is obviously an iterative procedure and a simple MATLAB program was written to solve for  $p$ , seen in Appendix A. Figure 15 shows the procedure that the program follows. At this stage, an extrapolated value can be calculated using:

$$\dot{m}_{EXTRAPOLATED}^{21} = (r_{21}^p \dot{m}_1 - \dot{m}_2) / (r_{21}^p - 1) \quad (19)$$

This extrapolated value can then be compared to numerous grids, and the percentage deviation from it indicates an approximation of grid induced error. Sample results of the procedure can be seen in Table 3 below. It shows first order convergence and indicates that a 31,211 node grid is 3.1% away from a grid converged solution.

	GRID 1	GRID 2	GRID 3	THESIS GRID
NODES	153,067	89,744	52,852	31,211
REPRESENTATIVE SIZE [mm]	2.745	3.589	4.678	
MASS FLOW RATE [kg/s]	0.36556	0.36718	0.36927	
r <sub>21</sub>	1.3075			
r <sub>32</sub>	1.3035			
p (Order of Convergence)	1.0043			
EXTRAPOLATED MASS FLOW RATE	0.360 kg/s			
THESIS MASS FLOW RATE				0.371 kg/s
% ERROR USING 31,211 NODES GRID (GRID USED IN THIS RESEARCH)	100*(0.371-0.360)/0.360 =			3.1 %

Table 3: Richardson's Extrapolation Sample Results

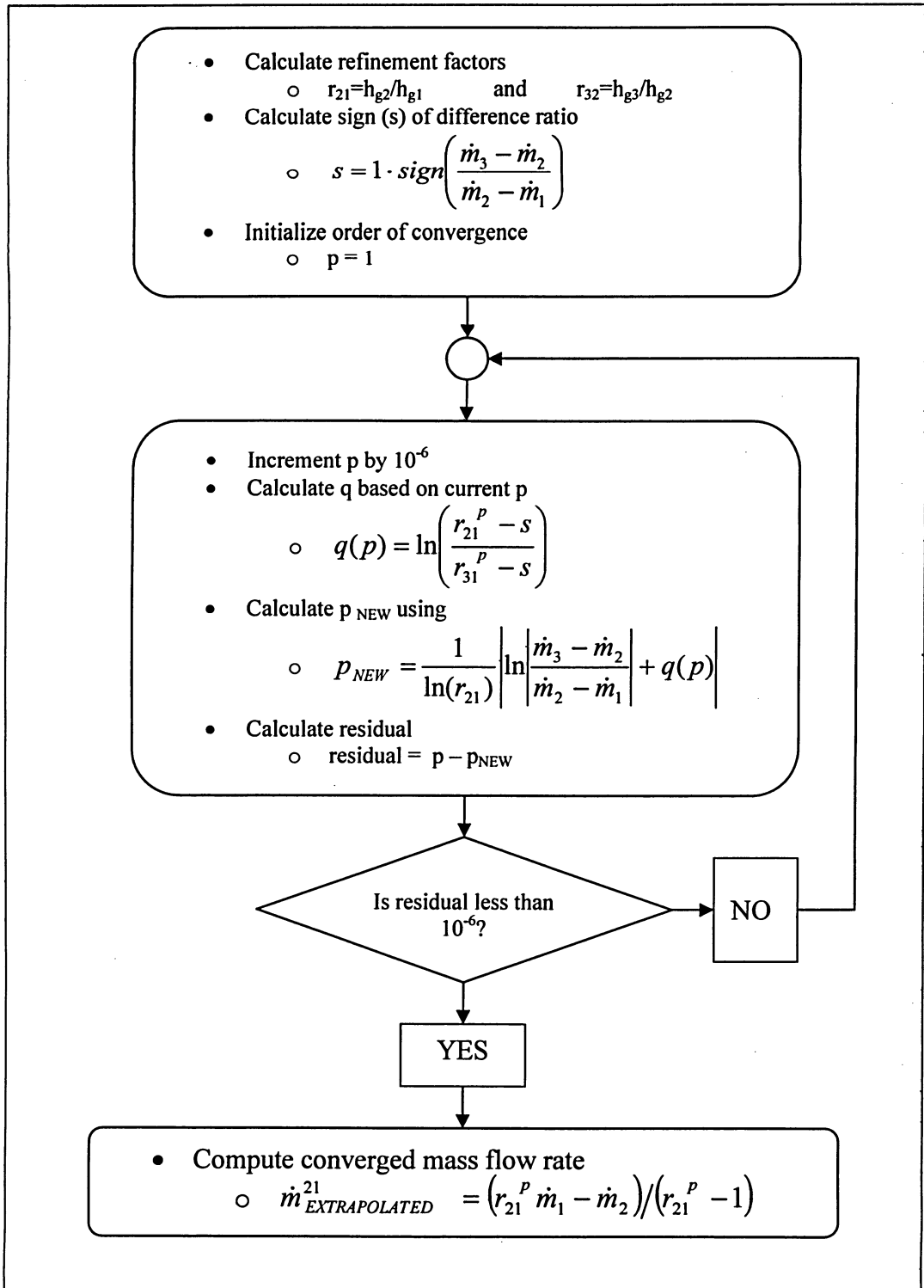


Figure 15: Solution procedure for obtaining grid-converged mass flow rate

## **CHAPTER 5: SIMULATING STATIC CHARGE AND MAGNETIC FIELDS**

### **5.0 CHARGE GENERATION AND MAGNETIC FIELD SIMULATION**

The success of this study depended on the ability to simulate a few physical phenomena other than those built into the FLUENT software package. To facilitate this process, FLUENT offers the ability to modify the equations it solves by introducing source terms through the use of user defined functions (UDFs). It allows further freedom of simulation by allowing the user to introduce whole new user defined scalar (UDS) transport equations. The UDS transport came in useful in trying to simulate the transport of charge throughout the flow. A useful feature in applying a magnetic field was the ability to define a certain property (such as magnetic field strength) within user defined memory (UDM). The process of using UDFs, UDS, and UDM are discussed in the following sections.

## 5.1 FLUENT USER DEFINED FUNCTIONS (UDFs)

UDFs in FLUENT are defined by writing custom ANSI C code. The user specifies in FLUENT, the location of the source code file that holds the user's functions. FLUENT then proceeds to automatically compile the source code using the computer system's built in C compilers. Although the code syntax is that of ANSI C, most commands and data types are specified within FLUENT's UDF.h header file. Once UDF.h is included at the beginning of the code, these custom data types and commands can then be invoked throughout the user defined functions. For example, the user can loop through all the cells in a given domain by using the following commands:

```
thread_loop_c(t,d)    and    begin_c_loop(c,t)
```

These commands and more are defined in the FLUENT UDF Manual [5]. The complete source code for all the UDFs written in this thesis is found in Appendix C.

## 5.2 CHARGE GENERATION THROUGH USER DEFINED SCALAR (UDS) TRANSPORT

To simulate the generation and transport of charge, two things had to be defined within FLUENT. First, a user defined scalar was turned on. This procedure effectively turns on an extra transport equation within FLUENT that works with an arbitrary scalar defined by the user. In this project, the scalar was assumed to be charge per unit mass  $\hat{q}$ . FLUENT then had to be told that the flux (convection) of this scalar happens through mass flow. To give meaning to this arbitrary scalar transport, a source term had to be defined by writing UDFs.

### 5.2.1 TRANSPORT EQUATIONS

The following equation was added by turning on FLUENT's UDS function.

$$\frac{\partial}{\partial t} \int_V \rho \hat{q} dV + \oint_A \rho \hat{q} V \cdot dA = \oint_A \Gamma \nabla \hat{q} \cdot dA + \int_V S_{\hat{q}} dV \quad (20)$$

It is an integral form of the transport equation for the variable  $\hat{q}$ . The first left hand side term is a non-steady term which upon convergence should go to zero. The

second left hand side term in the equation is the convection of charge as defined by the “flux through mass flow” setting within FLUENT. This setting effectively introduces the  $\rho V \cdot dA$  values in the convection term. The first right hand side term is the diffusion of charge. As per the Assumptions (Section 2.1), the diffusion of charge  $\Gamma$  value was maintained at a value of 0.01. This kept diffusion effects low but maintained numerical stability. The last term on the right hand side is the most important. It is the source term for  $\hat{q}$  term that gives the rest of the equation a non-trivial solution. It was defined as a UDF and is described in the following section.

### 5.2.2 SOURCE TERM UDF FOR CHARGE GENERATION

The following equation was used to define the source term within the transport equation:

$$S_{\hat{q}} = c\rho \cdot \exp\left(-\frac{\hat{q}}{\hat{\phi}}\right) \cdot \left(\mu_T \left|\frac{\partial u}{\partial y} + \frac{\partial v}{\partial x}\right|\right) \quad (21)$$

The above source term ensures that charge is generated through the presence of shear stress in the flow. The term in the second bracket takes a similar form to viscous terms within the Navier Stokes equations [4]. This was done to limit the charge generation to the boundary layer only. The presence of the exponential term simulates the decreasing ability to generate charge when the flow is already charged. The shear-charge constant,  $c$ , and charge-derivative constant,  $\hat{\phi}$ , in the source term were added as scaling factors for the amount of charge being generated. The shear-charge constant was used to scale the source term, while the charge-derivative constant was added to scale the source term's derivative. Currently, both are being assumed to be a constant, but it is possible that they could be dependent on flow properties such as temperature, which could be experimentally determined. The shear-charge constant and charge-derivative constant must be evaluated if a successful bleed slot design is to be achieved. For the purpose of this study, the default values of  $c$  and  $\hat{\phi}$  that were used were  $1 \times 10^5$  and  $3 \times 10^5$ , respectively. Initially, these were set arbitrarily but later refined after a constant independence study was performed (section 6.4). The values were set such that they



coincide with the corner of the plots in Figures 30 and 32. This corner is the transition point where flow cannot be reduced anymore. Increasing these constants any further would not result in further reduction of sonic flow coefficients. Since this represents a best case scenario, it would show the upper limit of the magneto-aerodynamic system's effectiveness. Knowing the upper limit gives future researchers an idea of the bleed system's maximum potential.

To define the source term in the UDF source code, a `DEFINE_SOURCE()` macro (defined in `UDF.h`) is invoked. This macro is computed at every iteration, when the source term for the transport equation is needed by the solver. It requires the definition of the source term itself, as seen in Equation 21, and the derivative of the source term. For purposes of solution stability, it is a common practice that the derivative should be negative; otherwise, unrestrained growth may result [5].

$$dS_{\hat{q}} = -\left(\frac{\rho c}{\hat{\phi}}\right) \cdot \exp\left(-\frac{\hat{q}}{\hat{\phi}}\right) \cdot \left(\mu_T \left|\frac{\partial u}{\partial y} + \frac{\partial v}{\partial x}\right|\right) \quad (22)$$

For a final design, all constants in Equations 20, 21 and 22 would have to be obtained using experimentation. For the purposes of this feasibility study, educated estimates were made to assign values to those constants. A short preliminary study was conducted to make sure the conclusions of this magneto-aerodynamic system do not hinge on knowing the exact values of these constants.

The following contour plot (Figure 16) shows the results of the user defined scalar transport equations when the solution is converged. As desired, the charge per unit mass is confined to the boundary layer in the main flow above the bleed slot. This is a result of specifying the source term to be proportional to the shear stress, and keeping diffusion value low. Evidence of a non-zero diffusion coefficient can be seen below the bleed slot in the plenum itself. A uniform non-zero charge per unit mass is seen all over the plenum, where the flow is much slower. This implies that convection does not dominate the flow as it does above the slot (lower Reynolds number), allowing charge to diffuse.

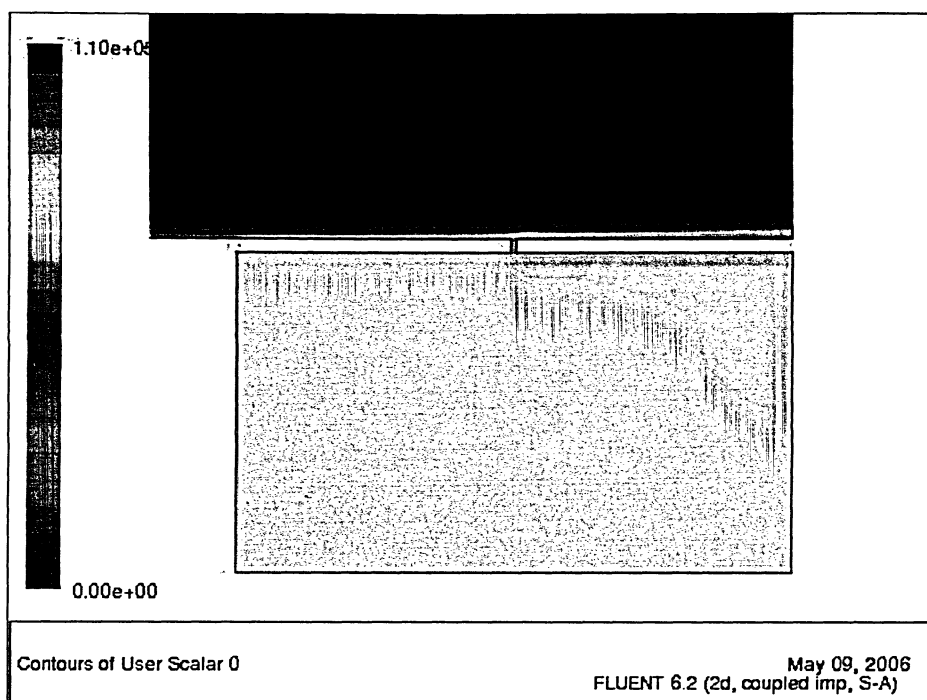


Figure 16: Contours of User Defined Scalar (Charge Per Unit Mass)

### 5.3 MAGNETIC FIELD APPLICATION

To impose magnetic forces on the flow, two things had to be defined within the UDF. First, the shape of the field had to be computed and stored within user defined memory (UDM). This would only have to be done once, right before starting the iterative process. The second part of imposing the magnetic field was to add body forces to the momentum equations. This was done by adding source terms to the X-momentum and Y-momentum equations within FLUENT through the use of UDFs. The following sections explain this two step procedure in detail.

#### 5.3.1 USER DEFINED MEMORY (UDM) LOCATION FOR FIELD SHAPE FUNCTIONS

The first step in imposing a magnetic field was to scale the maximum field strength,  $B$ , by a field shape factor product  $h_x h_y$ . The individual shape factors,  $h_x$  and  $h_y$ , had to be determined by Equations 23 and 24. The range of each of these  $h$  terms was between 0 and 1. Anywhere the function yielded a negative result, it would be replaced with a null value implying no field presence. This would cause the field to be

concentrated around a user defined centre point ( $x_{\text{field-centre}}$ ,  $y_{\text{field-centre}}$  specified in m). The shape functions were modified accordingly when field centre point required repositioning.

$$h_x = -10000(x - x_{\text{field-centre}})^2 + 1 \quad (23)$$

$$h_y = -2500(y - y_{\text{field-centre}})^2 + 1 \quad (24)$$

$$\text{If } h_x \text{ or } h_y < 0 \quad , \quad h_x h_y = 0 \quad (25)$$

These equations were specified by invoking the DEFINE\_ON\_DEMAND macro (defined in UDF.h header file) within the UDF source code. The shape functions above were written so that they were evaluated and stored in a user defined memory (UDM) location. This would ensure that FLUENT can efficiently access the pre-evaluated shape functions at any time, without having to perform shape function computations at every iteration. To call this UDF, do the necessary computations (Equation 23 and 24), and populate the UDM locations for each cell within the domain, the EXECUTE ON DEMAND function was called inside of the FLUENT solver GUI. Upon Executing On Demand, the UDM locations for each cell are filled and ready for use at any point after that by the FLUENT solver. The figure below shows contours of the values created and stored in the User Defined Memory. As Equations 23 and 24 (and condition in equation 25) are specified, it can be seen in the diagram that the range of values is between 0 and 1.

### 5.3.2 SOURCE TERM UDFs FOR MOMENTUM SOURCE

The force required for flow modification is generated when a charged particle moves through a magnetic field. The force acts in the direction perpendicular to the plane defined by the magnetic field and flow direction vectors. Therefore, to control the flow within an engine inlet (aligned in the x-direction) and bleed slots (aligned in the y-direction), magnetic field lines must be aligned in the z-direction. The vector product of the magnetic field line vectors and the flow vectors yields the force direction and

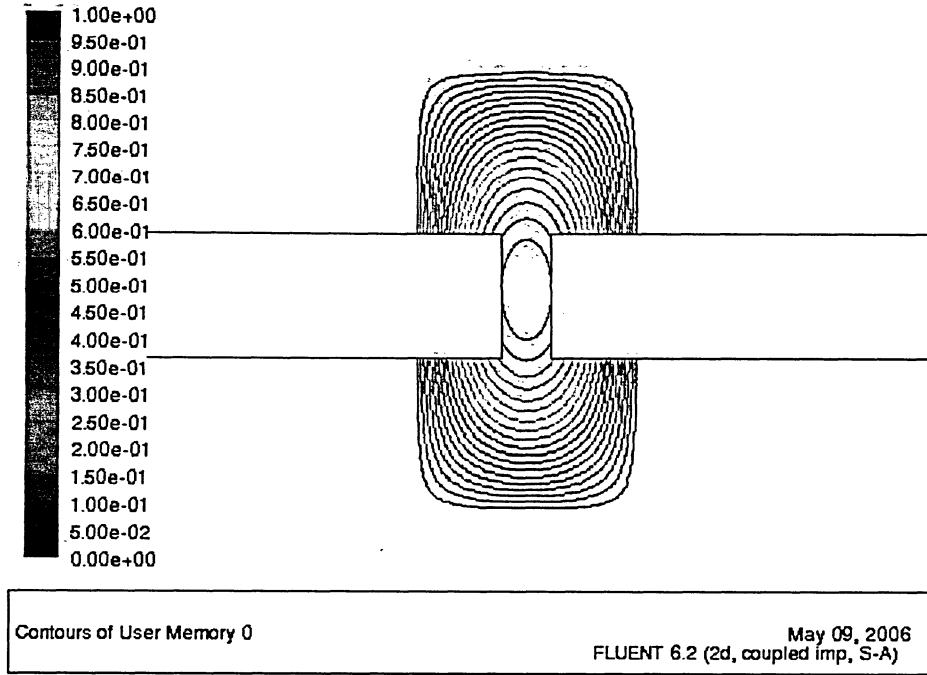


Figure 17: Field Shape Factor Product ( $h_x h_y$ ) stored in User Defined Memory

magnitude. Typically a force generated by a magnetic field is defined by the equation [19]:

$$F = q\vec{V} \times \vec{B} \quad (26)$$

This equation had to be modified by splitting it into its x and y components and scaled by shape factors described earlier. In the absence of a discrete-phase model, force on the flow was modeled using a continuum analysis; therefore these forces were scaled by density to convert them to source terms on a per volume basis. This was required for use in the FLUENT finite volume solver.

$$F_x = -vBh_x h_y \hat{q}\rho \quad (27)$$

$$F_y = uBh_x h_y \hat{q}\rho \quad (28)$$

These equations were defined using DEFINE\_SOURCE() within the user defined function code. Later  $F_x$  and  $F_y$  were applied in FLUENT as source terms for the x and y moment equations, respectively.



## CHAPTER 6: RESULTS AND ANALYSIS

### 6.0 RESULTS

The following sections will present a summary of the data collected from the numerical CFD research, and evaluate it in terms of the feasibility criteria. For all results presented in the following sections, the performance variable studied is the sonic flow coefficient,  $Q$ . This was calculated from a mass flow rate obtained from FLUENT's surface integration feature. A vertical FLUENT surface (line) was created that spans the slot width at -0.56 mm (approximately half the depth of the slot) below the top surface of the hole. Figure 18 shows the definition of geometrical and flow parameters that will be varied through the numerous studies presented in this chapter.

Unless otherwise indicated, the following is the baseline:

- Slot placed such that  $\delta^*/D = 0.95$
- $D$  (Diameter) = 4.399 mm
- Depth to Diameter ratio ( $L/D$ ) = 2.54
- Slot Angle =  $90^\circ$
- Free stream Mach number = 1.97
- $P_{\text{FREE STREAM}} = 101325 \text{ Pa}$
- $P_{\text{PLENUM}} / P_{\text{FREE STREAM}} = 0.1$

The above definition of slot width is made by specifying a diameter ( $D$ ). In the general field of bleed flows, numerous configurations are studied including holes; therefore, it is a common practice to specify the width of the perforation as a diameter for consistency. For this reason, the 2D slot width is specified as a diameter.

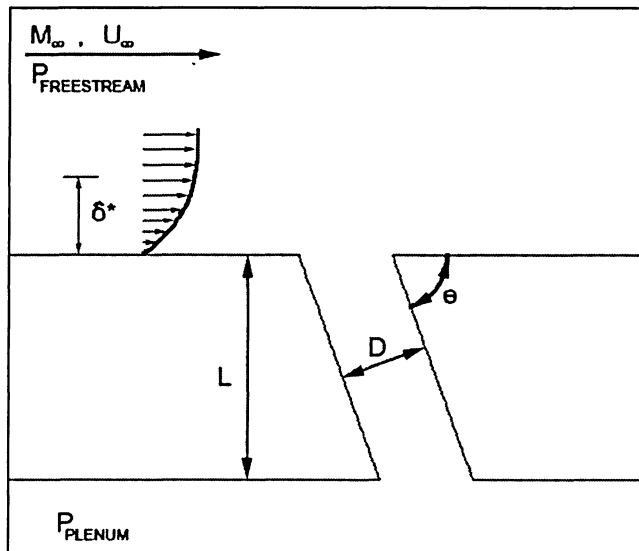


Figure 18: Definition of Case Variables

## 6.1 GRID INDEPENDENCE STUDY

Grid independence studies were performed to determine the sensitivity of the mass flow rate through the bleed slot with respect to mesh size. The first study involved grids of 90 degree bleed slots at Mach 1.97.

The first cases ran without the presence of magnetic fields. It was found that grid sizes of 31,211 nodes yield solutions that are within approximately 3.1% of a grid converged solution of 0.360 kg/s. To obtain this estimate, Richardson's extrapolation was used as outlined in the "Statement on the Control of Numerical Accuracy" in the Journal of Fluids Engineering [16]. The procedure was outlined in more detail in Section 4.5.1. This grid size was selected since this thesis looks for changes in bleed flow much greater than 3.1 %; hence, errors of this magnitude are acceptable. Figure 19 shows the results of mass flow rates for numerous grid sizes.

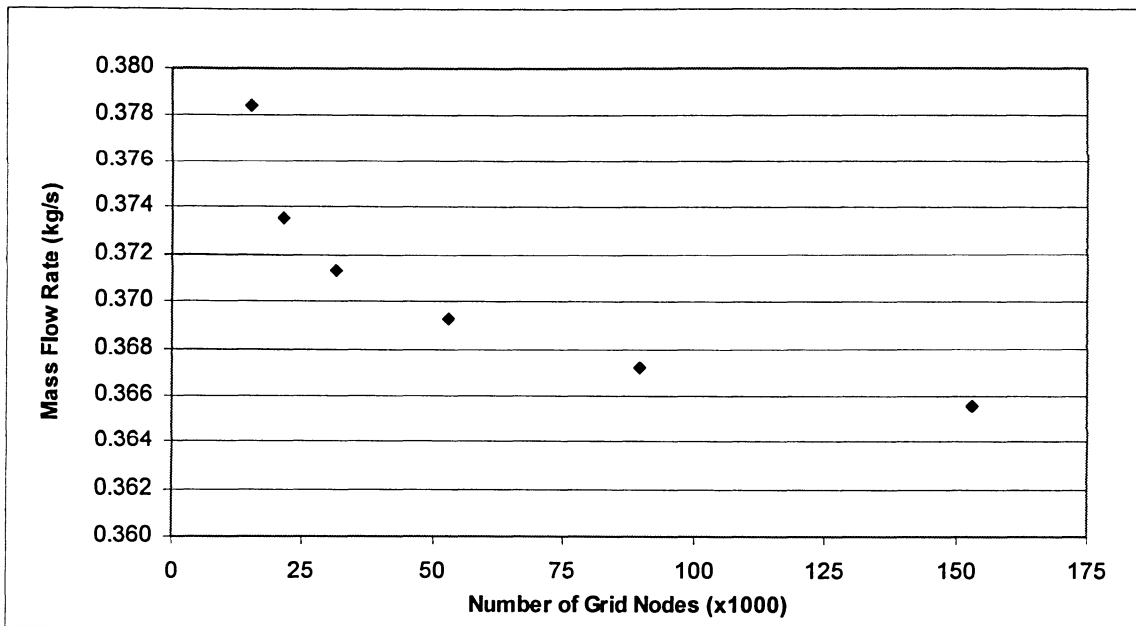


Figure 19: Grid Sensitivity for a Mach 1.97 Bleed System through a 90 Degree Slot

The second stage of grid independence studies looked at the effects of charge generation, as well as presence of magnetic fields. This ensured that the presence of charge and magnetic fields within the flow did not change its sensitivity to grid size. The results of this study showed oscillatory grid convergence as seen in Figure 20, and the 31,311 node grid yielded a solution which differed by approximately 3.7% from grid the converged values. To study this erratic oscillation of mass flow rates, conservation of mass in the slot was inspected. A secondary sampling surface was created 1.1 mm above the midpoint of the hole and auxiliary mass flow rates were sampled there. Then they were compared to the mass flow rates at the midpoint and the percent difference was plotted. This can be seen in Figure 21. The main purpose of this was to ensure that the grid convergence can be obtained. Due to conservation of mass, in the absence of mass creation or destruction, the mass flow rates should be the same. It is apparent from Figure 21 that as the number of nodes in the grid increases, the percent difference in mass flow rates tends towards 0. Furthermore, the mass flow rate on the 31,311 node grid is approximately 1% away from state of perfect mass conservation.



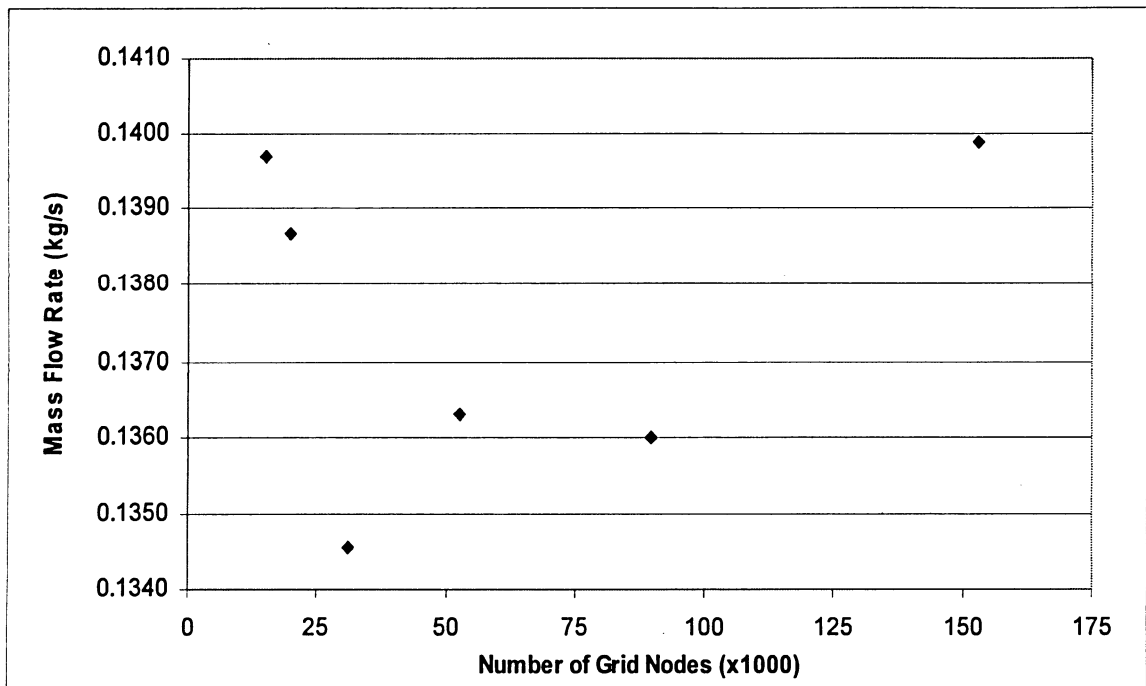


Figure 20: Grid Sensitivity Study for a Mach 1.97 Bleed System through a 90 Degree Slot - Influenced by Magnetic Field / Charge Generation

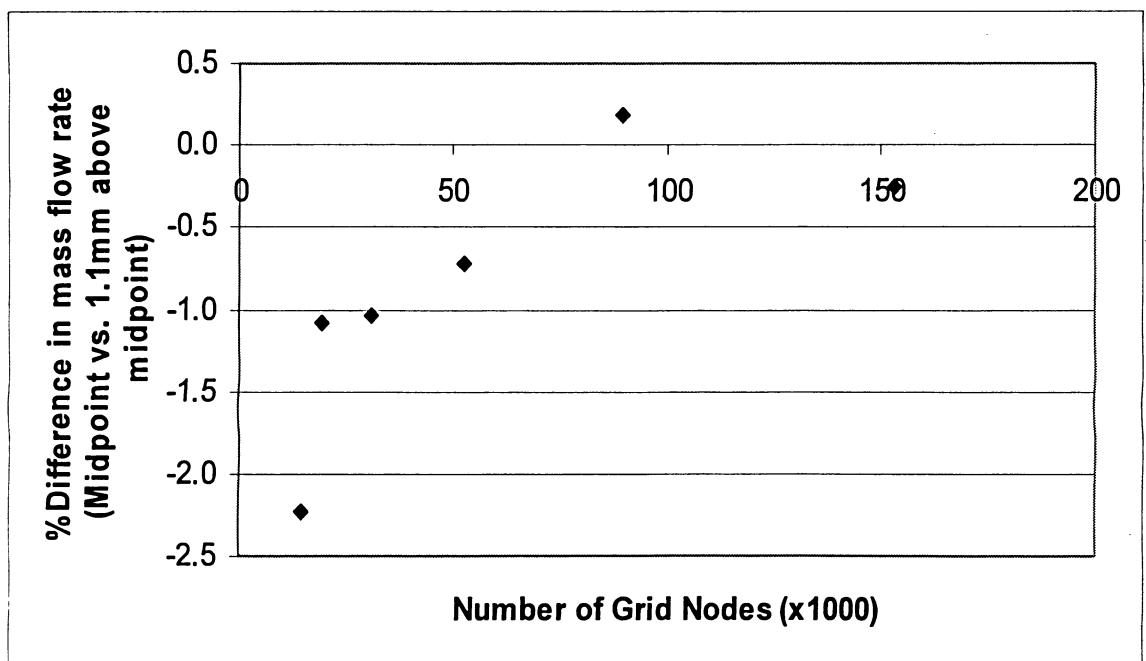


Figure 21: Conservation of Mass through slot study

To present the numerical errors on the side of caution, 4% error bars appear on all remaining plots of sonic flow coefficient, and only one study in Figure 36 shows results approaching the error threshold. Certain figures have error bars of upwards of 5% due to oscillations of the mass flow rate in certain rare cases. These oscillations have been noted and presented in the raw data in Appendix D.

## 6.2 SOLUTION (CODE) VERIFICATION

The first test to verify the FLUENT code's capability of handling compressible flows was a simple Prandtl Meyer inlet (Figure 1 in Chapter 1) geometry. The Prandtl Meyer inlet was exposed to a free stream Mach number of 8.3. It has some important features which appropriately appeared in the inviscid FLUENT solution. A smooth isentropic compression emanating from the inlet ramp was present, as well as an oblique shock intersecting the corner of the ramp and throat of the inlet. Figure 22 below shows these phenomena, which allows a preliminary qualitative verification of the solver.

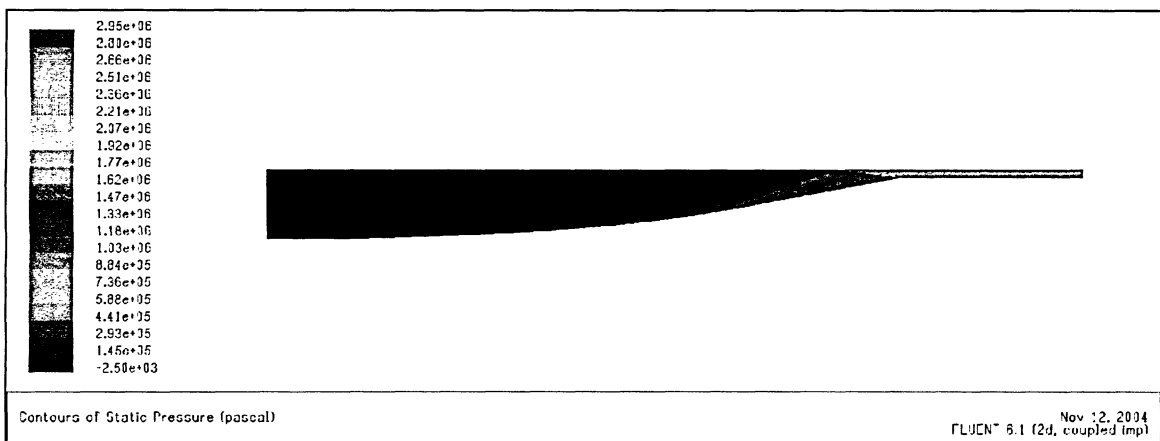


Figure 22: Prandtl-Meyer Inlet. Code verification case at Mach 8.3

For verification, compression ratios of the inlet were compared to theoretical values derived by Molder *et al* [15]. The FLUENT local pressure to free stream pressure ratio ( $p/p_{atm}$ ) before the oblique shock was approximately 5.7, while the theoretical one is 6.0, showing only a 5% discrepancy. The pressure ratio behind the shock was approximately 26 in FLUENT versus a theoretical value of 27, yielding a discrepancy of 3.7%. This shows that the FLUENT solver is capable of performing compressible

solutions within a satisfactory margin of error. For a more context specific comparison using bleed flows, a verification was performed on 90° bleed slots.

To quantitatively verify the FLUENT code's ability to handle bleed flow and grids generated in this thesis, a number of cases were run at different plenum pressure to total free stream pressure ratios. These data were compiled and compared to data obtained from Harloff and Smith [7]. Figure 23 presents the published experimental data for a 90° bleed slot with a depth to diameter (L/D) ratio of 2.54 exposed to range of Mach numbers and pressure ratios. The experimental data are for a 3D slot that is 1cm long (in the z-coordinate direction). Superimposed on this figure are data generated by FLUENT using the 2D (no z-coordinate) grids created in this thesis. At pressure ratios below approximately 0.05, there is a very high agreement between CFD and experiment. As the pressure ratio increase, there is a discrepancy that arises. This discrepancy was expected and analyzed as follows.

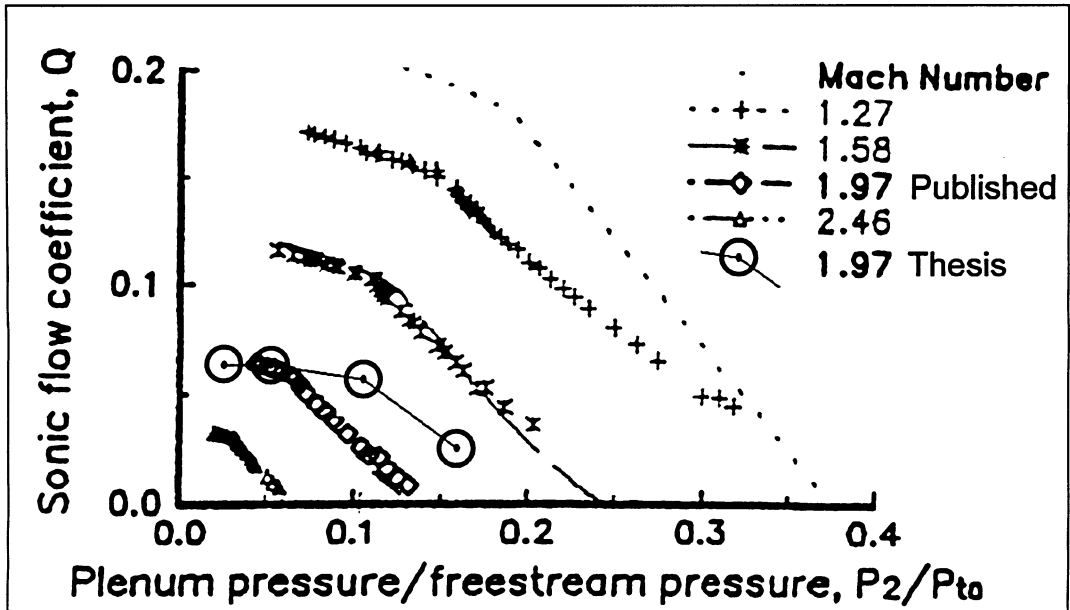


Figure 23: Published Figure [7] with thesis results (circled points) superimposed.

A 3D system experiences boundary layer interference effects that are not present in a 2D system. A 3D slot's extra walls, and the interaction of boundary layers from walls which meet at 90° cause additional drag and impede flow thus reducing sonic flow coefficients. A 2D analysis does not exhibit this phenomenon and therefore it is expected that the values would be elevated. A possible reason the agreement is higher at lower

pressure ratios is because lower pressure ratios increase the flow through the slot, effectively increasing the Reynolds number and therefore making boundary layer and viscous effects less significant. As the pressure ratio increases, the flow slows down through the bleed slot and viscous effects which are magnified by 3D geometry become more significant.

FLUENT's correct behaviour can also be verified by observing qualitative features of a bleed system. Qualitative observations will ensure that FLUENT is correctly modeling certain phenomena which have a significant impact on sonic flow coefficients. Figure 24 shows a typical "vena contracta" within a bleed slot. A vena contracta is an effective narrowing of a bleed slot due to separation [7]. This narrowing creates a virtual throat through which the flow can pass through. Without the vena contracta, the throat would be much larger and sonic flow coefficients would be unrealistically high.

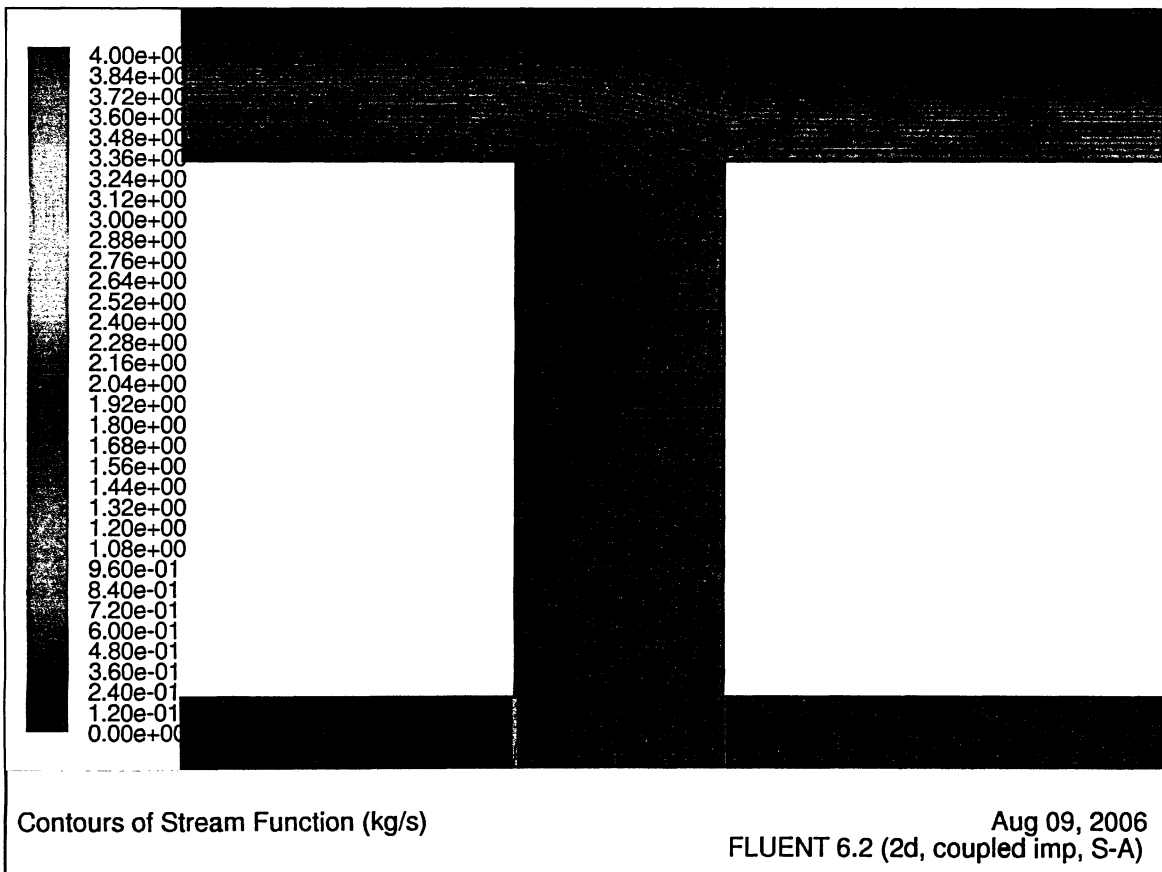


Figure 24: Stream Lines within 90° Bleed Slot showing a Vena-Contracta

### 6.3 TRANSIENT EFFECTS

Although transient effects did not influence the final outcomes and results of this study, it is worth mentioning the process by which convergence of results was obtained. In early trials with the k- $\epsilon$  turbulence model, convergence to steady conditions using the state solver could not be obtained within the plenum. Upon changing FLUENT settings to perform a time dependant analysis, a steady state solution was obtained by going through an initial transient stage. The transient analysis leading up to steady state was noted and shown in Figure 25. It shows how the jet emerging from the bleed slot is wavy. Observing a transient analysis animation, it was evident that the snaking jet was shedding vortices (appearing as closed contours visible in Figure 25). A transient sequence of images can be seen in Figure 26. This shows how the vortices propagate downwards towards the pressure outlet boundary. Also, it should be emphasized that even though the solution had initial transients to go through, they did not affect the main flow above the slot or inside the flow. The mass flow rates recorded were converged well before the plenum solution reached steady state. Even though Figure 26 shows the plenum changing, the mass flow rate through the slot stayed constant at 0.371 kg/s. This was due to the fact that the jet emerging from the bleed slot was supersonic. Since the plenum is downstream of the slot, it did not influence the mass flow rate at all.

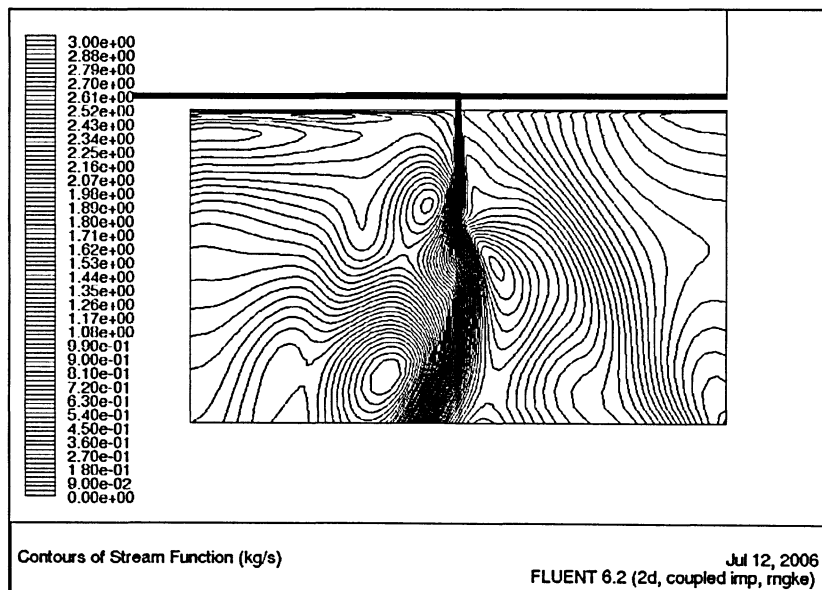


Figure 25: Vortex shedding from the bleed jet within plenum

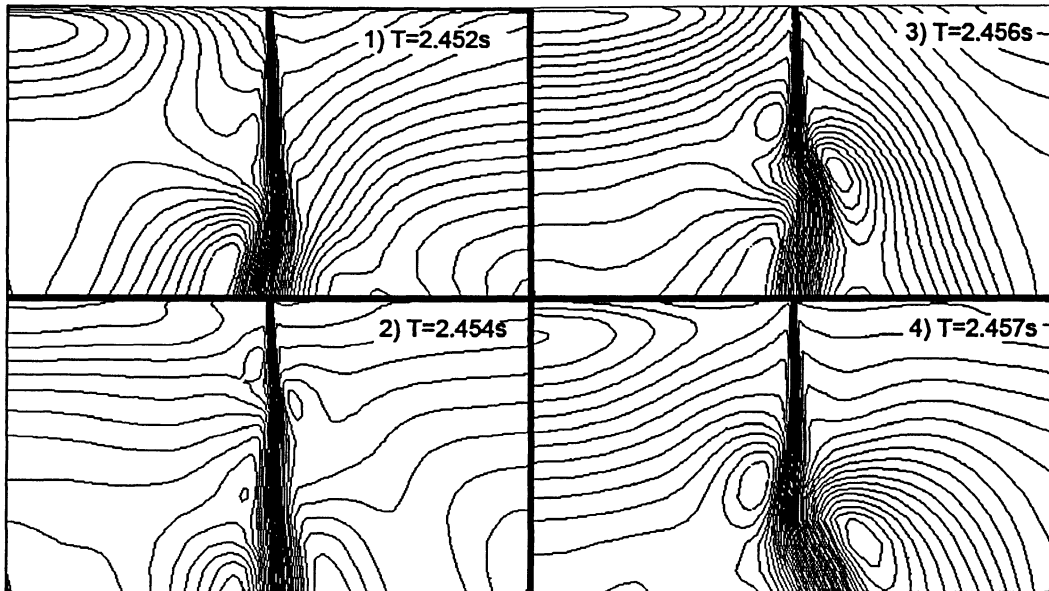


Figure 26: Transient Sequence of Vortex Shedding (mass flow constant at 0.371 kg/s)

Upon reaching a steady state solution, the jet emerging from the bleed slot settled down and emerged in a straight diamond shock pattern of a supersonic exhaust (seen in Figure 27). To verify that the boundary conditions in the plenum are behaving as they should, it can be observed in Figure 28 that the steady state streamlines on all 3 sides (left, bottom, right) of the plenum are perpendicular to the boundaries. Once it was discovered that a steady state solution could be obtained without having to use a transient analysis using the S-A turbulence model, the S-A model was used for the entire thesis.

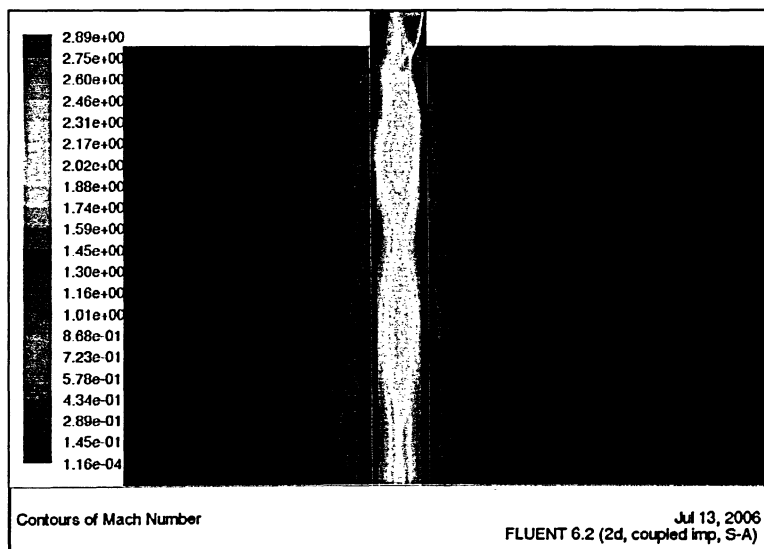


Figure 27: Steady state Mach Contours solution showing Diamond Shock Pattern

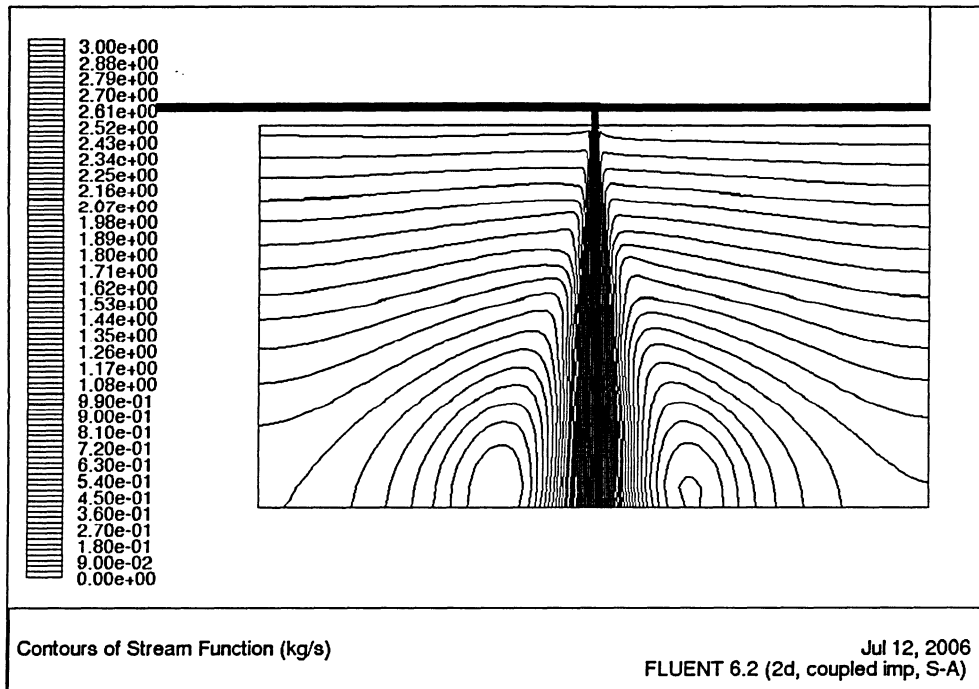


Figure 28: Steady state converged solution with plenum

#### 6.4 FEASIBILITY CONSIDERATIONS (CHARGE MODEL CONSTANT INDEPENDENCE)

The first set of cases to be studied were designed to see if the constants present in the charge generation source term would influence the conclusions in this thesis. Figure 29 shows two curves, one that resulted from variations in the shear-charge constant,  $c$ , and another that resulted from the variation of the charge-derivative constant,  $\hat{\phi}$ . The coincidence of both plots shows that, regardless of which constant is manipulated, the mass flow rate depends only on the maximum charge present in the flow. Therefore, it can be concluded that the constants do not influence the feasibility of the system studied in this thesis, and the knowledge of their values would be only necessary for design purposes. Obtaining these constants could be done through experiment.

Figure 29 is a compilation of data presented in Figures 30 through 33. The main feature of these four figures is that they show a definite limit to how much the sonic flow coefficient can be reduced by simply varying the constants. This can be especially seen in Figures 30 and 32. This limit is reached regardless of how much charge is in the

boundary layer, because maximum charge can continue to increase (as seen in Figure 31) even though the sonic flow coefficient is not changing any more. Even though there is a limit that is reached, it happens after at least a 64% drop in sonic flow coefficient. This happens on Figure 32 at a  $\hat{\phi}$  value of  $3 \times 10^7$  where the sonic flow coefficient has dropped down to a value of 0.0231 (as compared to a sonic flow coefficient of 0.0636 when the magnetic field is off). This implies that in the worst case scenario, the charge equation constants can limit the effectiveness of the system to no less than 64%. Varying the shear charge constant,  $c$ , shows a higher limit to sonic flow coefficient drop. It is approximately 89% , occurring at a  $c$  value of  $2 \times 10^5$  and yields a sonic flow coefficient of 0.00657.

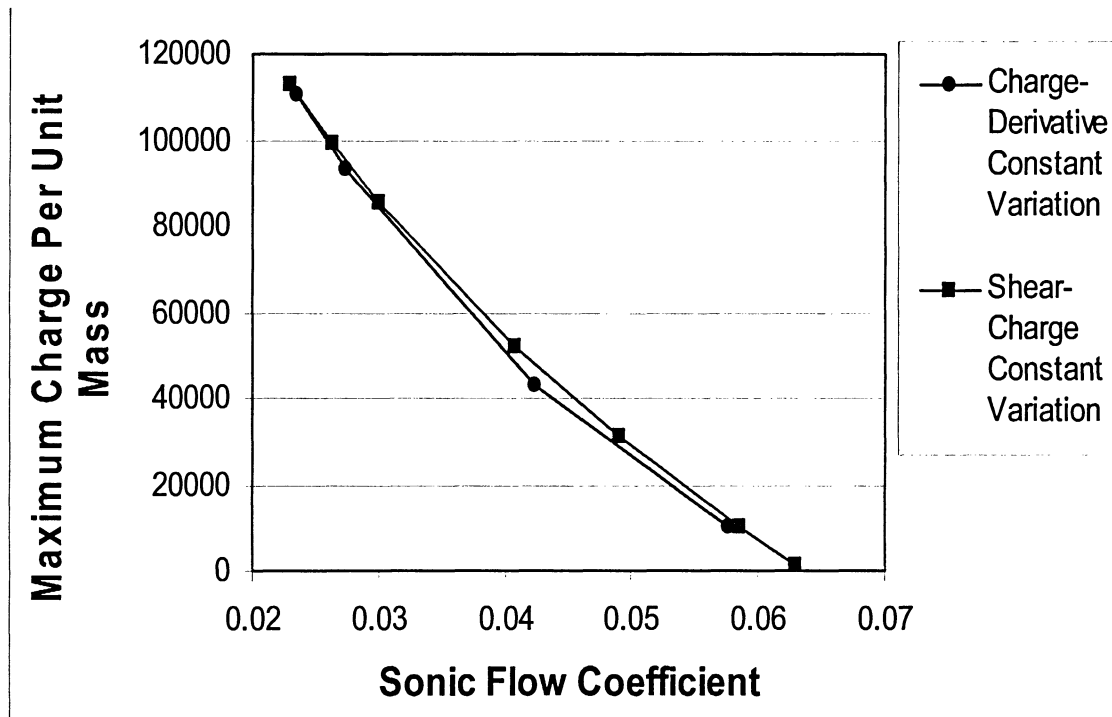


Figure 29:  $Q$  versus  $\max(\hat{q})$  , Demonstration of Coefficient Independence



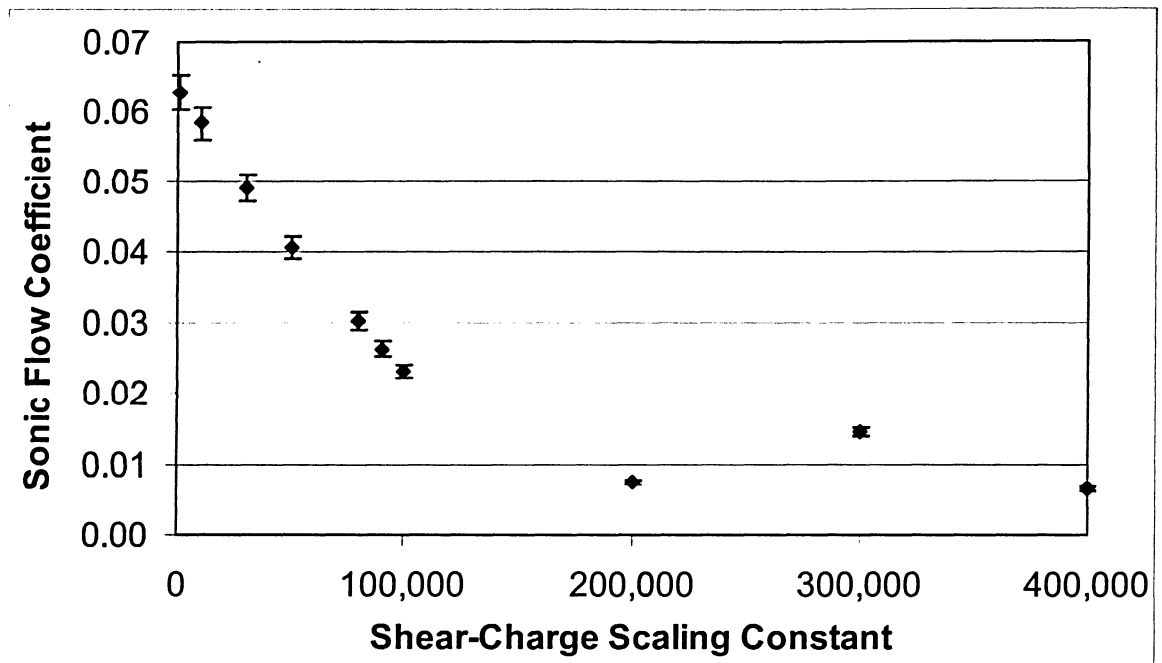


Figure 30: c Constant vs. Sonic Flow Coefficient: 90° slot at Mach 1.97

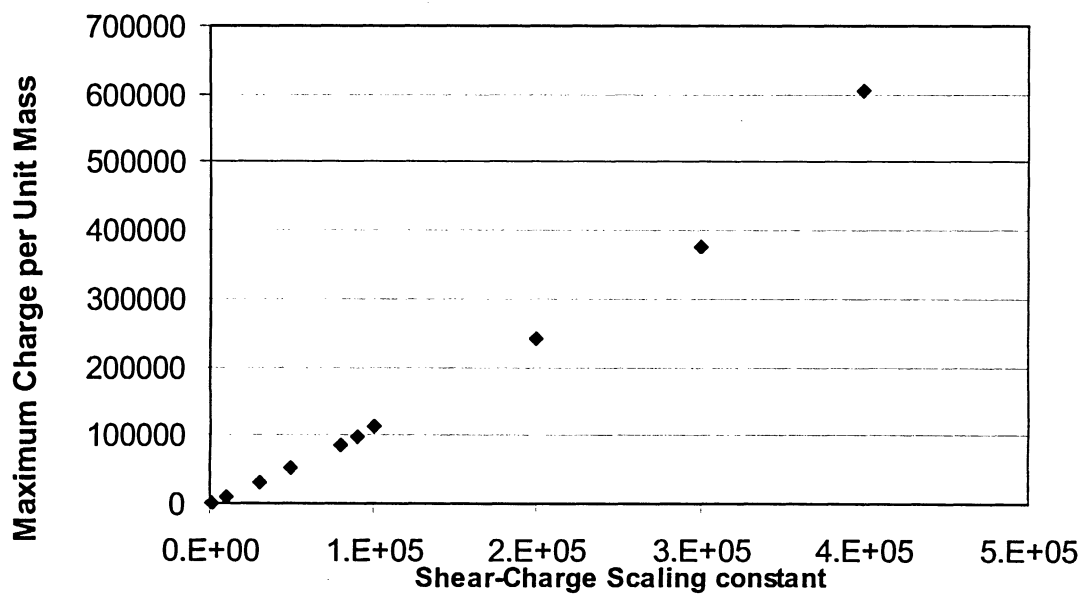


Figure 31: c Constant vs. Maximum Charge Per Unit Mass: 90° slot at Mach 1.97

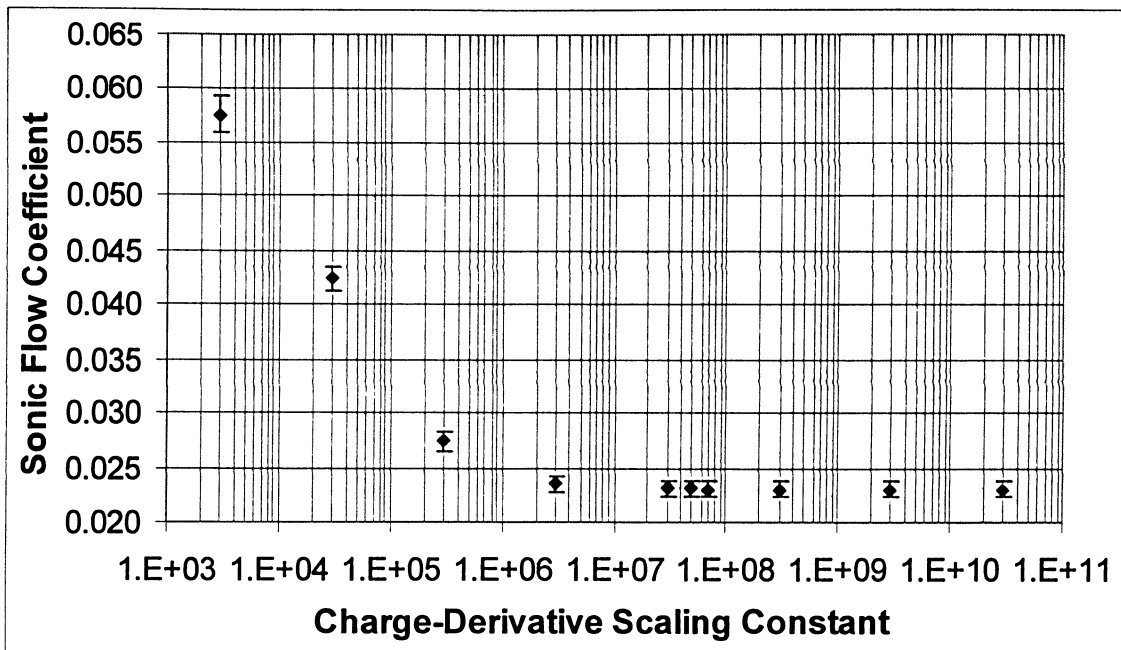


Figure 32:  $\hat{\phi}$  Constant vs. Sonic Flow Coefficient: 90° slot at Mach 1.97

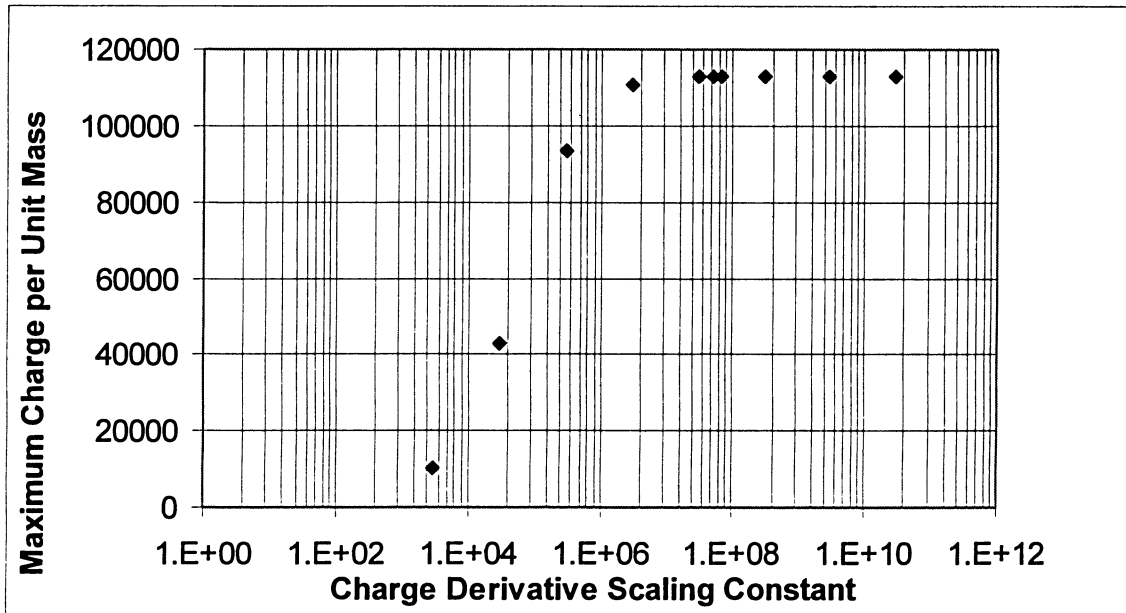


Figure 33:  $\hat{\phi}$  Constant vs. Maximum Charge per Unit Mass: 90° slot at Mach 1.97

## 6.5 FIELD STRENGTH VARIATION

A study to see the effects of magnetic field strength was performed. It is evident from Figure 34 that raising the field strength increases the effectiveness of the bleed control system by dropping the value of sonic flow coefficients. The field strength was specified by inputting a value of  $B$  in Equations 27 and 28. This value corresponds to the maximum strength at the centre of the field distribution (where  $h_x h_y$  equals 1). By simply varying the field strength alone, the sonic flow coefficients can be dropped by upwards of 89%. This takes the sonic flow coefficient from 0.0636 without a magnetic field, to 0.00676 at a field strength of 0.9 Tesla. As in the previous section, it appears that there is a physical limit to which the sonic flow coefficients can be reduced, but this is not of concern, because the limit of 89% would be very satisfactory.

One major observation that can be drawn from this is as follows. Even if the maximum charge in the flow is overestimated by the charge generation source terms, it can be compensated for by increasing the magnetic field strength. If the amount of charge was underestimated, then a real-life system would require a weaker magnetic field. This is not a concern since a weaker magnetic field would require less power to implement.

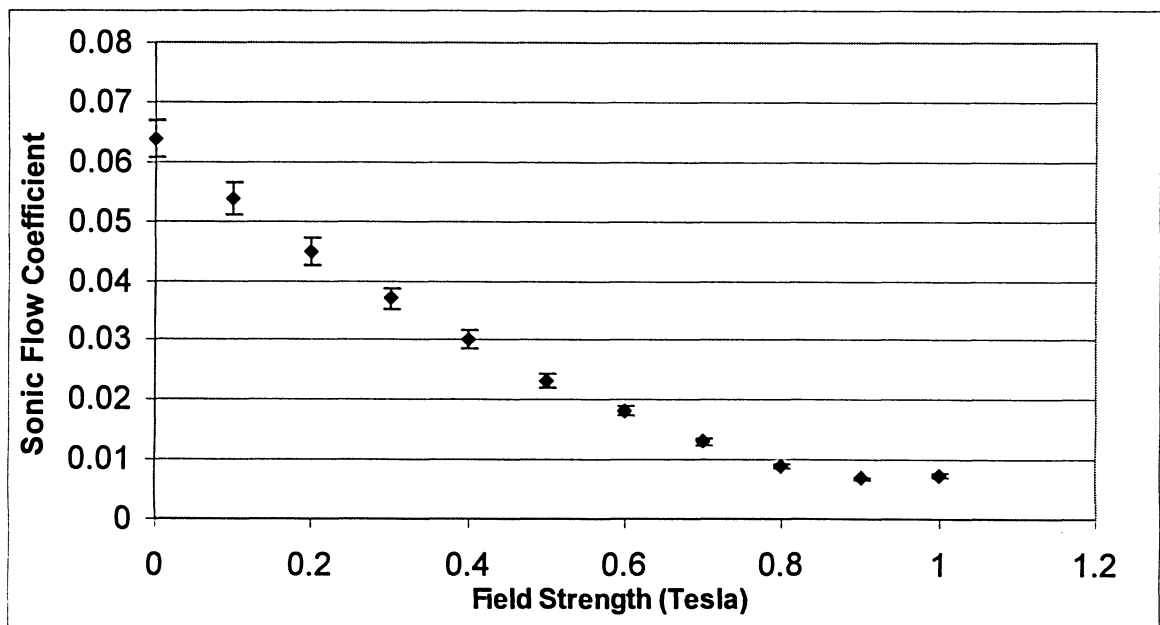


Figure 34: Field Strength Variation vs. Sonic Flow Coefficient

## 6.6 FIELD LOCATION OPTIMIZATION

Through the field shape functions  $h_x h_y$ , it was possible to move the field centre around freely. Taking advantage of this, an optimization of field centre location was performed, while keeping the strength of the centre fixed at 0.5 Tesla. Figure 35 below demonstrates how the field strength distribution (determined by the shape function  $h_x h_y$ ) is taken from the baseline position to the eventual optimized position.

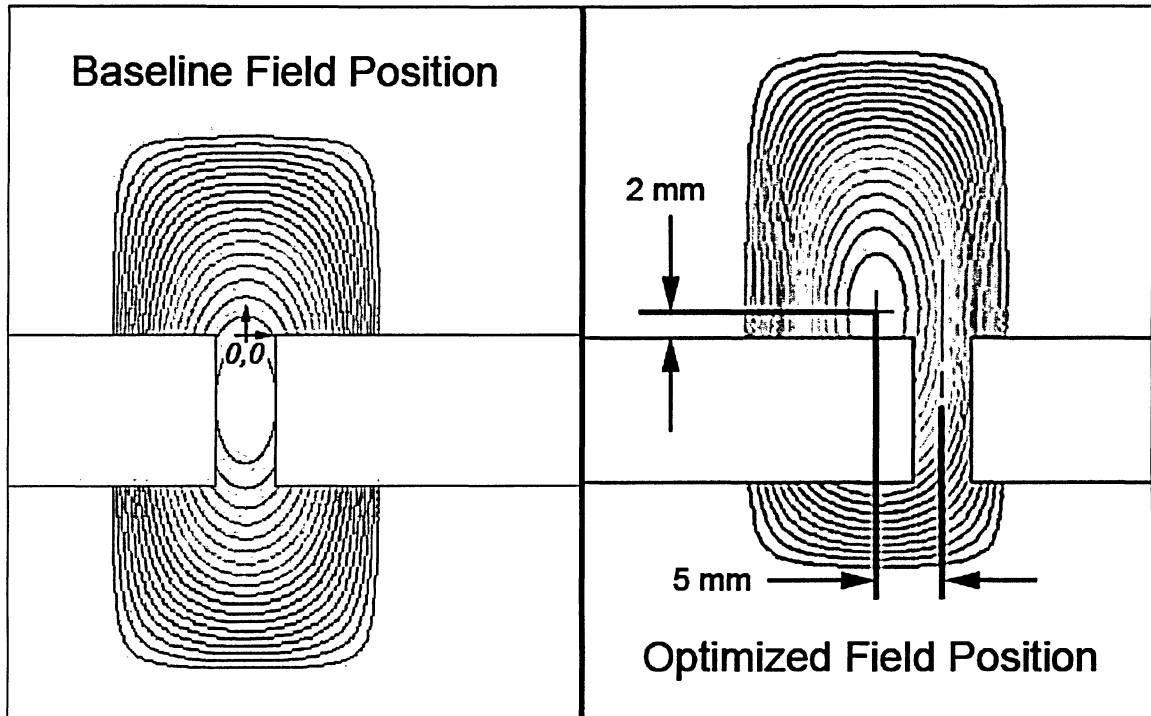


Figure 35: Magnetic Field positioning ( $h_x h_y$  contours), Baseline and Optimized Case

First, solutions for different vertical locations were obtained. These can be seen in Figure 36. It was found that by simply moving the field centre from the vertical centre of the slot to approximately 2 mm above the entrance of the slot, the sonic flow coefficient can be reduced from 0.135 to 0.110. This translates to an 18% reduction. Furthermore, once solutions were obtained for different horizontal positions (with the field centre fixed at a +2 mm vertical position obtained earlier) even much greater drops in sonic flow coefficient were obtained. Figure 37 shows that by placing the field -5mm from the slot centre line, the coefficient can be dropped from 0.110 to 0.044, translating to another 60% reduction. Overall, this optimized location of the field centre results in

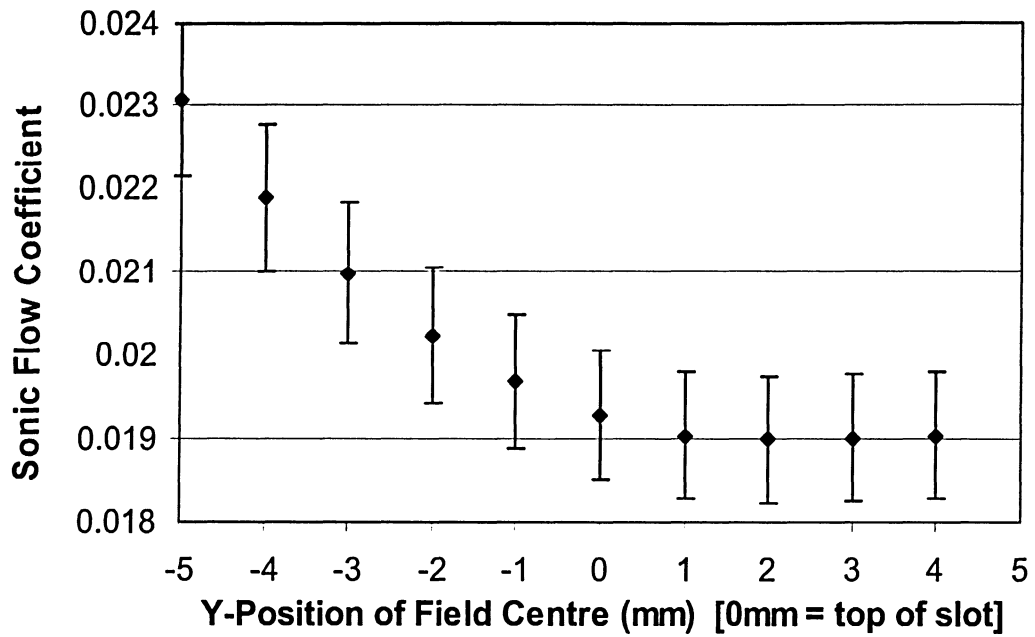


Figure 36: Field Centre Vertical Location Variation Study

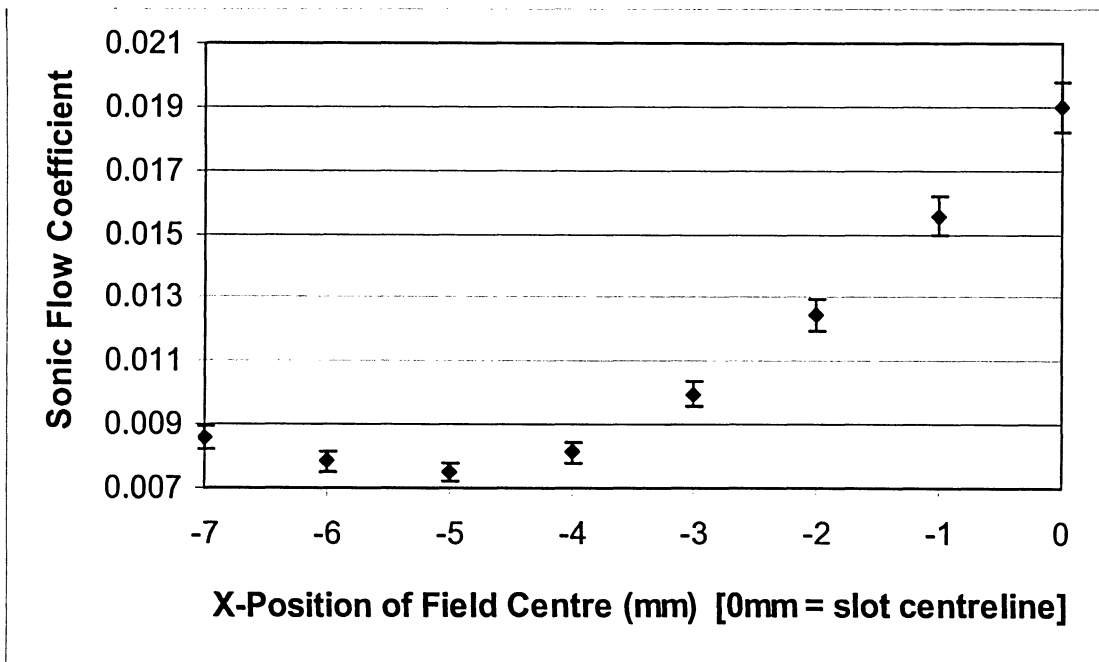


Figure 37: Field Centre Horizontal Location Variation Study

an 88% decrease in sonic flow coefficient over the no-field case. Figures 38 shows the resulting Mach contours of this optimized case. One important side effect of implementing a magnetic field worth noting is the resulting separation bubble right behind the slot. Although it does reattach, it creates significant shocks within the main flow, which could reduce the efficiency of an engine inlet [10].

A supplementary case was run to combine the results of the field strength and position studies. A case with the optimum field position and a field strength of 0.9 Tesla (as obtained in section 6.5) yielded a sonic flow coefficient of 0.0204 which translates to a drop of 70% from the no-field case. This means that a 3 parameter (x position, y position, strength) optimization should be performed to find an ideal field design.

*Note: The remaining (geometry, displacement thickness, Mach number, pressure ratio) studies in this chapter were all computed using the optimized field location ( $x = -5\text{mm}$ ,  $y = 2\text{mm}$ ) and a field strength of 0.5 Tesla .*

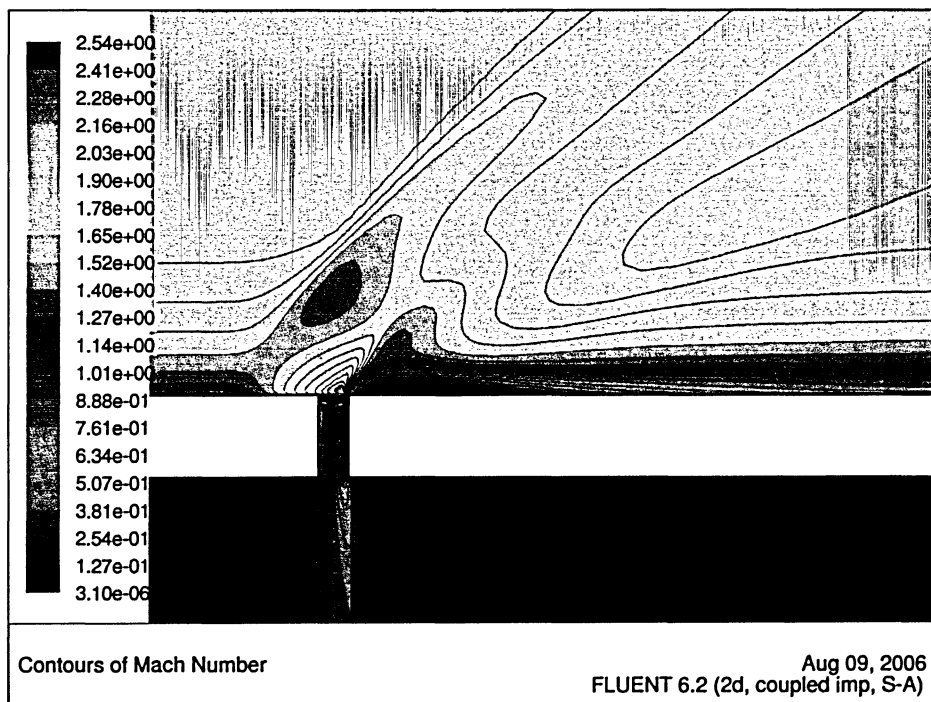


Figure 38: Mach contours resulting from optimized field location

## 6.7 BLEED SLOT GEOMETRY VARIATION

Another set of cases looked at different slot geometries to see what kind of an effect they would have on the performance of the optimized bleed control system discussed in the previous section. In particular, the angle  $\theta$  was varied in 10 degree steps yielding 3 cases for comparison: the baseline 90 degree slot, and two new cases of 80 and 70 degrees. The 70 degree case can be seen in Figure 39.

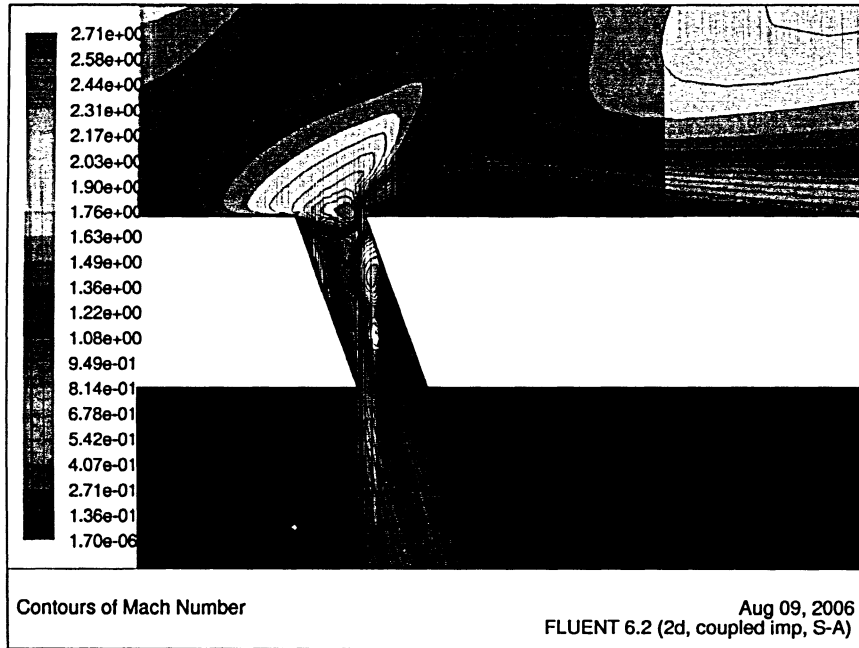


Figure 39: Mach Contours of 70° Slot at a Free stream Mach number of 1.97 - Field On

In general, the 80 and 70 degree cases exhibited higher sonic flow coefficients than the 90 degree case because angled slots have better alignment to the incoming flow. With the magnetic field turned on, the 70° and 80° slots had sonic flow coefficients of 0.0140 and 0.0128 respectively (versus the value of 0.00749 for a 90° slot). This decreasing sonic flow coefficient trend (with increasing angle) held true for cases with the optimized magnetic field turned off as well. With the magnetic field off, the sonic flow coefficients for 70, 80, and 90 degree slots were 0.0771, 0.0701, and 0.0636, respectively. The important result that should be noted is that the drop in sonic flow coefficient was not as pronounced as on the 90 degree slot. The 80 and 70 degree slots both exhibited a drop of 82% in sonic flow coefficient, compared to 88% on a 90 degree slot.

Another interesting observation was that local Mach numbers near the slot were 7% higher on the angled slots (maximum Mach number at 90° was 2.54, and at 70° it was 2.71). This would have implications in final design considerations because higher Mach numbers, especially in front of a separation bubble, could imply stronger shockwaves within the system. Therefore, not only is the magneto-aerodynamic control less effective on an angled slot but it also causes higher local Mach numbers. It is very likely that the magnetic field would need to be optimized for every geometry individually. Only further variations of field shape and position on these specific geometries could determine if sonic flow coefficients could be decreased over the 88% shown by the 90° case.

## 6.8 DISPLACEMENT THICKNESS VARIATION THROUGH LEAD PLATE LENGTH VARIATION

To study the effects of boundary layer size on the bleed flow, a series of grids were constructed with different lengths of plate leading up to the bleed hole, thus changing the boundary layer displacement thickness at the hole. Table 4 is a summary of the cases that were looked at:

Plate Length (metres)	Resulting $\delta^*/D$ (computed @ 1 slot diameter ahead of slot)
1.75	0.95
1.25	0.79
0.95	0.67
0.75	0.54
0.25	3.39E-04

Table 4: Relationship of slot location to displacement thickness

Figure 40 shows that with increasing  $\delta^*/D$  (from  $3.39 \times 10^{-4}$  to 0.95), the sonic flow coefficients decrease slightly for cases with the field off (from 0.0665 to 0.0637) and drastically for cases with the field on (from 0.0662 to 0.00750). Figure 41 shows the percentage drop in sonic flow coefficient and a clear trend develops. It appears the larger the  $\delta^*/D$  ratio, the more effective the bleed control system is. This is due to the fact that, for larger ratios, the lead plate has to be longer. Longer lead plates have more distance to generate charge; therefore, more charge is present within the boundary layer. It also appears, when  $\delta^*/D$  tends towards zero, the percentage drop of the sonic flow



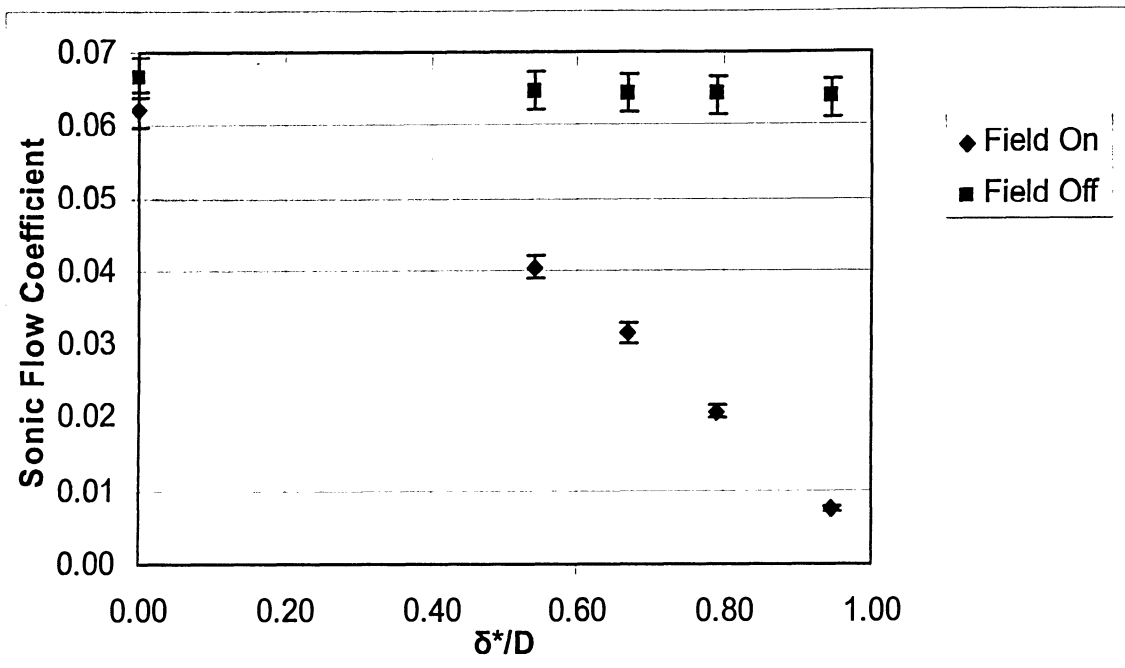


Figure 40: Effect of  $\delta^*$  on Sonic Flow Coefficients with Magnetic Field On & Off

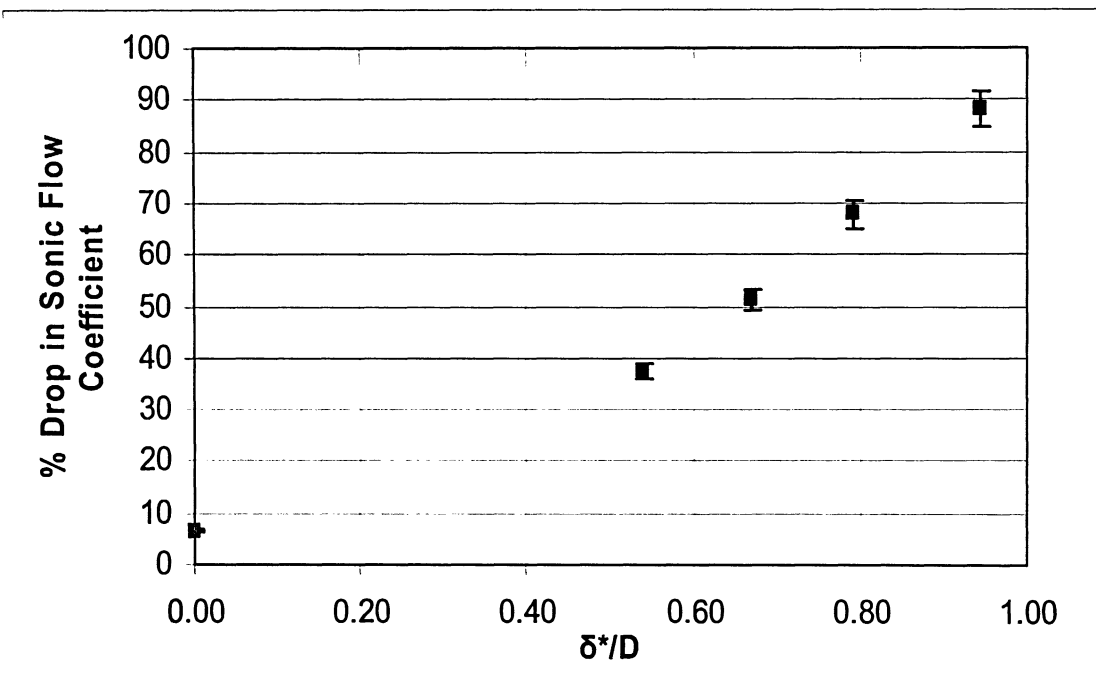


Figure 41: Influence of  $\delta^*$  on Effectiveness of Bleed Flow Control

coefficient also tends toward zero. This was to be expected, since the charge generation equations depend on the boundary layer development to generate charge source terms. As the plate gets shorter and the boundary layer is less significant, the solution tends toward an inviscid solution, where charge cannot be created; hence, sonic flow coefficient cannot be reduced by any significant amount with a magneto-aerodynamic control system.

The significance of this study shows that the positioning of the slots within an inlet would change how effective the system would be. Therefore, depending on the slot position (assuming more than one slot), each slot would have to have its own finely tuned magnetic fields. This is a result of holes further down stream in an inlet having more charge built up to take advantage of.

Furthermore, if this thesis over estimates charge buildup, the results of this study show reassuring trends. The hole can be scaled down (increasing the value of  $\delta^*/D$ ), thus increasing the effectiveness of the control to the point where conclusions in this thesis are once again valid.

## **6.9 MACH NUMBER VARIATION**

The Mach number variation study looked at the bleed control system's performance under a series of Mach numbers leading up to and slightly above the design Mach number. Figure 42 shows the values of sonic flow coefficient with both the magnetic field on and off, for different Mach numbers. At higher Mach numbers, it is apparent that the sonic flow coefficients are lower. The values with the magnetic field turned off dropped from 0.289 to 0.0309, and values with the field on dropped from 0.157 to 0.00256. These were respective decreases created by Mach number increases from Mach 1 to Mach 2.4. This implies that, under higher free stream Mach numbers, the solution is further from an ideal isentropic case and exhibits higher aerodynamic losses. Figure 43 shows the percentage drop in sonic flow coefficient when the magnetic field is turned on. The percentage drop in sonic flow coefficient behaves in the exact opposite manner. As Mach number is increased from 1 to 2.4, the sonic flow coefficient's percent reduction increases from 46% to 92%. This implies more effective magneto-aerodynamic bleed control at higher Mach numbers. The higher effectiveness is a result of increased

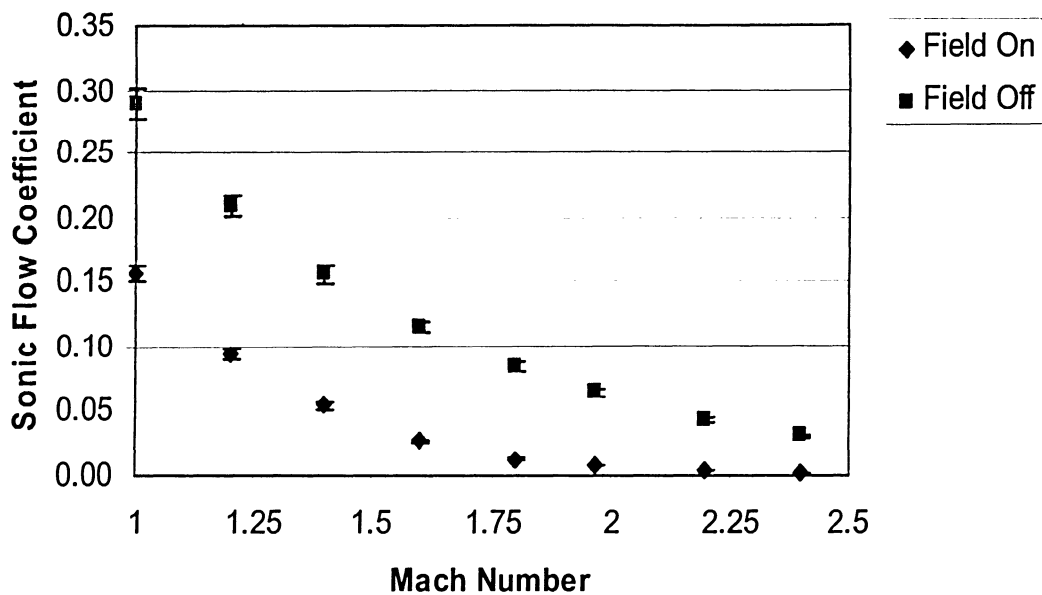


Figure 42: Mach number and Sonic Flow Coefficients with Magnetic Field On & Off

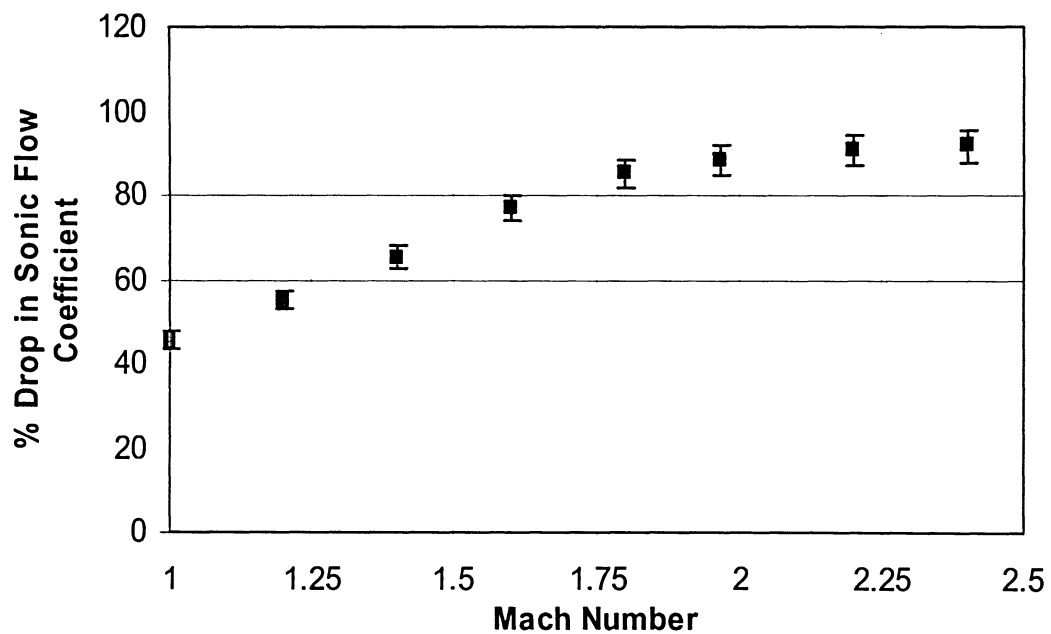


Figure 43: Influence of Mach number on Effectiveness of Bleed Flow Control

speeds and shear stress in the boundary layer causing higher values of charge. This trend seems to become less pronounced when Mach 1.97 is passed. Up to Mach 1.97, the increase (slope of the plot) is approximately 43% per 1 Mach unit. Beyond Mach 1.97, the slope is only 8% per 1 Mach unit. This could be due to the fact that Mach 1.97 is the speed at which the magnetic field position was optimized (Section 6.6).

The significance of these results is that the bleed control system's effectiveness increase is approximately linear with respect to Mach number up to the number the field location was optimized for. Beyond that value, any increases in Mach number still show increases in sonic flow coefficient reduction effectiveness, although it is not as rapid.

## **6.10 PRESSURE RATIO VARIATION**

The pressure ratio variation study looked at the driving pressure gradient that drives flow through the bleed slot and how it influences the bleed flow control effectiveness. From Figures 44 and 45, it was found that, although the sonic flow coefficients drop as the pressure ratio is increased (gradient decreased), the bleed control effectiveness increases. Although this in itself is not surprising since the magnetic field has less of a driving force to fight against, there is one important observation that should be noted. A pressure ratio of 0.1 yielded a 88% drop in sonic flow coefficient, while a pressure ratio of 0.4 yielded a 98% drop, effectively resulting in a sealed slot. This means that there exists a balance between the driving pressure gradient and magnetic field forces which result in very little flow moving through the slot. Beyond a pressure ratio of 0.4, the driving force through the slot reduces significantly and the magnetic field becomes too strong, causing a complete reversal of flow in the slot. This is represented by a sonic flow coefficient drop of 155%. The reason this value is higher than 100% is because the flow is now reversing. This could have catastrophic consequences within a propulsion system, causing too much mass flow going into an inlet, resulting in an unstart (reversal of self-start) condition. Figure 46 shows the vectors of a situation like this, where, at a pressure ratio of 0.6, the flow begins to reverse, causing an even larger separation bubble behind the slot than before, and larger shocks.

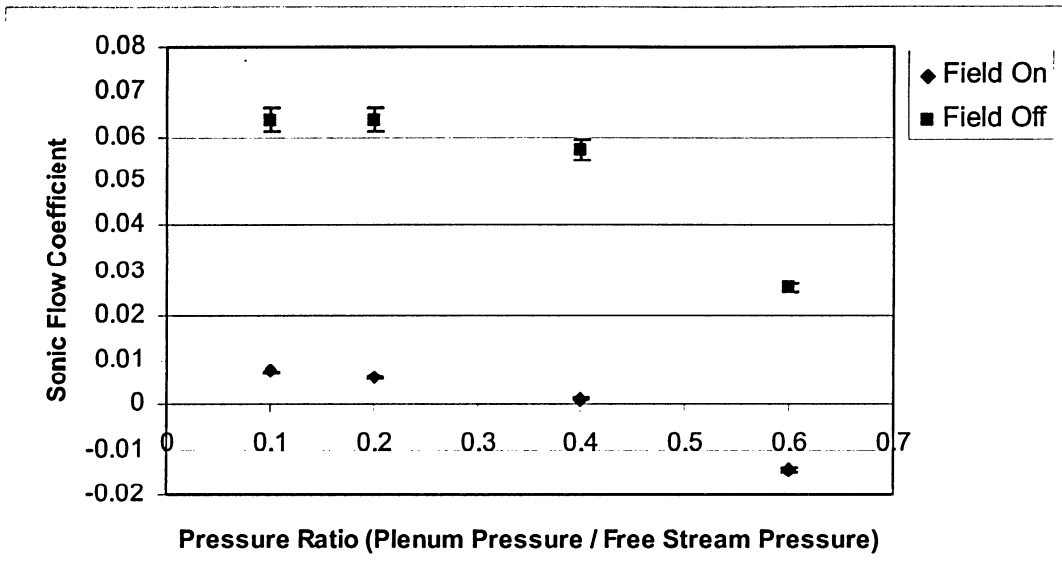


Figure 44: Effect of Pressure Ratio with Magnetic Field On & Off

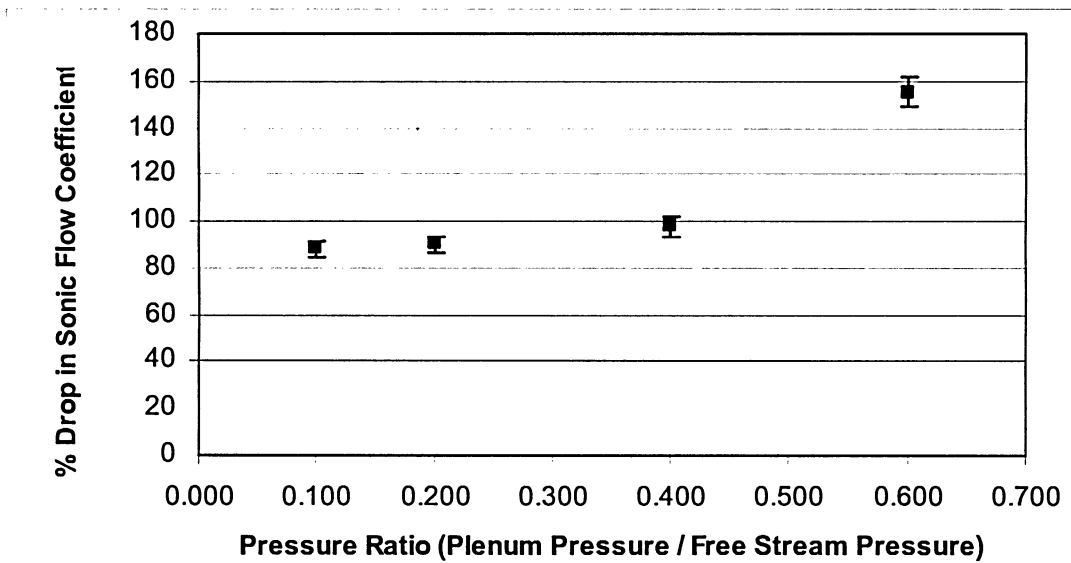


Figure 45: Influence of Pressure Ratio on Effectiveness of Bleed Flow Control

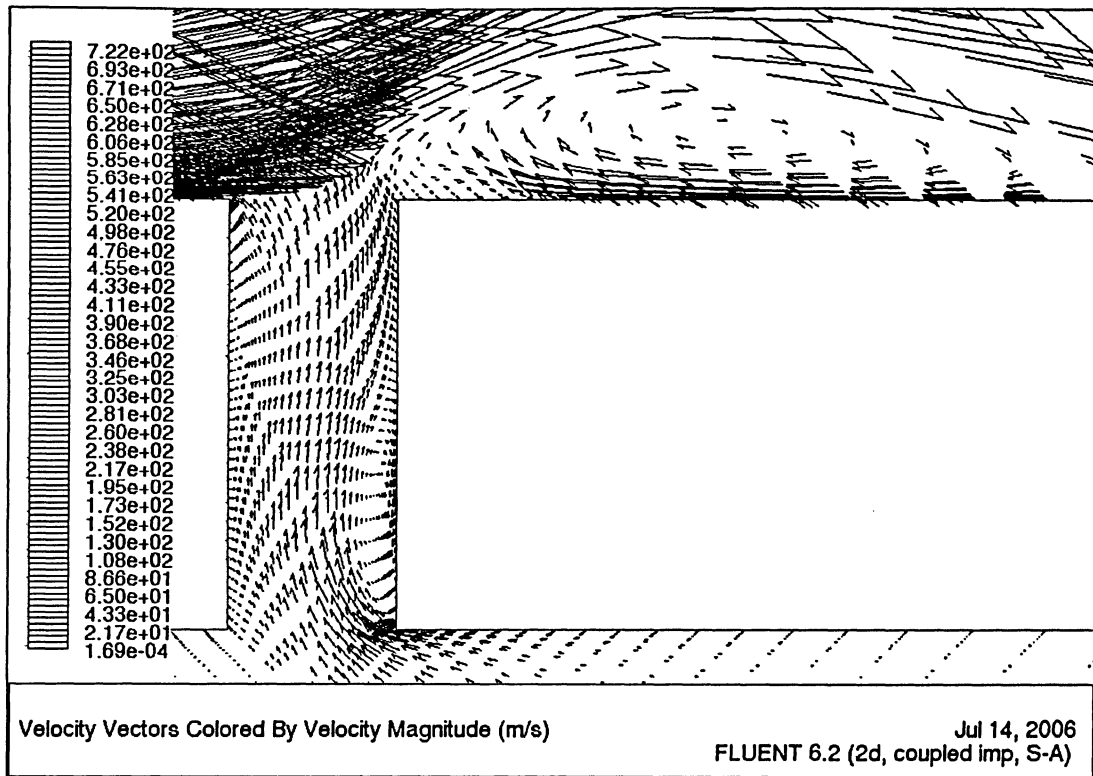


Figure 46: Reversed flow induced by Magnetic Field at Pressure Ratio of 0.6



## **CHAPTER 7: CONCLUDING REMARKS & SUGGESTIONS FOR FUTURE RESEARCH**

### **7.0 CONCLUSIONS**

To conclude this thesis, it should be noted that bleed flow control in high speed inlets using magneto-aerodynamics shows great promise. Although it hinges on assumptions made about the presence of static charge in the boundary layer, it is encouraging to see that flow within bleed slots could be controlled.

Some final generalizations and conclusions can be made about the magneto-aerodynamic bleed control system studied in this thesis:

- 1) It was shown that even when certain aspects of charge generation are underestimated or overestimated, it is fairly easy to compensate with other system parameters such as field strength or position as seen in Figures 34, 36 and 37.



- 2) An increase in field strength does increase the effectiveness of the control system. Figure 34 showed that sonic flow coefficients are reduced as much as 89% as field strength is increased. There appears to be a physical limit to which mass flow in the bleed slot can be controlled by increasing field strength.
- 3) Although the field location optimization that was done in this thesis is merely an exercise, not actual design, it shows that strategic placement of the magnetic field can reduce the sonic flow coefficients as effectively as simply increasing the field strength. Figures 36 and 37 have shown that sonic flow coefficients can be reduced by 88% when the field is moved 2mm above the slot entrance and 5mm left of the slot centerline.
- 4) Combining field strength and field location optimizations into one case produced a system that is not as effective as the others with only a 70% decrease in sonic flow coefficient. This means that a 3 parameter optimization would need to be done (x position, y position, and strength)
- 5) It was found that the effectiveness of a bleed control system depends on slot geometry as well. Applying the field position designed for use with a 90° slot, the sonic flow coefficients were reduced by only 82% in 70 and 80 degree slots, versus 88% for a 90 degree slot.
- 6) Studying the effect of displacement thickness  $\delta^*$  on the effectiveness of the system showed that thicker boundary layers have more charge built-up within them, and hence offer better control effectiveness. If future research shows that static charge in the boundary layer is not significant enough to modify flows of the size shown in this thesis, the  $\delta^*/D$  results show that the diameter can be scaled to even lower dimensions, where, once again, the conclusions drawn in this thesis would be valid.

- 7) Varying the free stream Mach number showed a linear relationship to sonic flow coefficient up to Mach 1.97. Beyond Mach 1.97, the slope of sonic flow coefficient to Mach number was reduced, but effectiveness continued to increase. This will be important to know for future design purposes because Mach number varies at different points in a diffuser.
- 8) The effectiveness of a bleed control system depends on the balance of the driving pressure gradient and magnetic field strength. It was shown that, at a plenum to free stream pressure ratio of 0.4, this balance is found, and the bleed slot sonic flow coefficient can be reduced by 98%. Below a ratio of 0.4, effectiveness is limited (at a ratio of 0.1, the sonic flow coefficients can be reduced by 88%). Above this ratio, the flow reverses and causes serious separation and shocks.

Although effectiveness of the control system varied depending on the case, this numerical feasibility study showed that a magneto-aerodynamic bleed flow control system has potential and that physical experimentation and further research is definitely warranted.

## **7.1 FUTURE RESEARCH SUGGESTIONS**

Upon completion of all the studies mentioned in the previous chapter, a number of important relationships were explored, some of which have a direct impact on future research. Since the feasibility of a magneto-aerodynamic system was reinforced by all the different studies conducted, it is suggested that future research be conducted under the following recommendations.

The first issue that must be resolved in future research is the determination of the constants within the charge generation equations. This can be done by designing experiments where emerging high speed jet flows that have charge built up within them are 'arced' by magnetic fields. This can then be modeled in CFD. The constants in the

equations can be adjusted so that the arc or displacement of the emerging jet matches that of experiment.

Another possibility of determining the nature of the statically charged boundary layer is to study high speed flow over a flat plate with electrodes embedded within the surface. As presumably there would be more charge present further downstream, there should be a voltage between electrodes downstream and upstream. This voltage could be measured for verification of boundary layer static charging.

Although the constants described above could be determined for a specific case, it is possible they are not constants but a function of properties such as temperature. It would be worth while to perform the studies described in Section 7.0 at different temperatures to determine this behaviour.

A natural extension of the research presented in this thesis would be to study 3D effects in a magneto-aerodynamic bleed control environment. 3D slots, as well as holes, plates and sequences of holes could be studied to observe their impact on bleed control effectiveness. Harloff and Smith [7] studied numerous configurations of bleed perforations, such as different L/D ratios, slot angles, hole shapes, plates, slots and hole patterns, so the body of experimental research for comparison is available.

The next step that should be taken, after the charge generation simulation equations are finalized and 3D effects are taken into account, is to study the bleed slots and magneto-aerodynamic control in the inlet environment. This means that a full viscous solution of a hypersonic inlet would have to be modeled, at which point bleed holes would be implemented within the geometry. After the CFD solutions would show that the bleed slots are effectively letting the inlet self-start, charge generations could be added in the same manner as done in this thesis and their performance in a real inlet environment could be studied.

For a complete design of a magneto-aerodynamic control system, a designer would need to look at more than just sonic flow coefficients through the CFD studies mentioned above. It would be necessary to model a complete inlet, verify charge generation equation constants, and then compare the final solutions to experiment. As mentioned in the theory chapter, the current state of technology dictates that CFD models

could be used to drive the design of experiments, not necessarily the design of the inlets themselves. As computing power becomes less expensive, it will be more economical to generate large grids which solve the system precisely enough for final design purposes.

Another topic of importance to a designer would be the flow features such as separation behind the bleed slots and oblique shockwaves generated by the deflection of flow around these separation bubbles. The field shape, size and strength would have to be adjusted to ensure that these performance robbing phenomena are minimized.

These future research proposals can now be used as a roadmap for developing the magneto-aerodynamic bleed control concept into a functional design and, in the process, advance the state of the art in high speed propulsion.



## REFERENCES

- 1) Anderson J.D. Modern Compressible Flow: Third Edition. McGraw Hill, New York USA, 2003.
- 2) Cheremisinoff N.P., Gupta R. Handbook of Fluids in Motion. Ann Arbor Science, Michigan, USA, 1983.
- 3) Chernyi L.T.. Electrification of Aircraft in Aerosol Flows with a solid disperse phase. Journal of Aerosol Science. Journal of Aerosol Science. Vol. 26, Suppl 1. 1995 .
- 4) FLUENT Inc. FLUENT 6.1 User Guide, Lebanon, NH, 2003.
- 5) FLUENT Inc. FLUENT 6.1 UDF User Guide, Lebanon, NH, 2003.
- 6) Goonko Y.P., Mazhul I.I.. Efficiency of Boundary Layer Bleeding for Hypersonic Aircraft With Ventral Ramjet Module. KORUS '99 Third Russian-Korean International Symposium on Science and Technology Proceedings, 2000 .
- 7) Harloff G. J. and Smith G.E.. Supersonic-Inlet Boundary-Layer Bleed Flow. AIAA Journal, 0001-1452 vol.34 no.4 (778-785), 1996.
- 8) Hill P. and Peterson C. Mechanics and Thermodynamics of Propulsion, 2nd Edition. Addison-Wesley Publishing Company, Massachusetts USA, 1992.
- 9) Hoffmann K.A., Chiang S.T. Computational Fluid Dynamics Volume II 4th Edition, Engineering Education System, Wichita, Kansas, USA, 2000.
- 10) Holland S.D.. Internal Aerodynamics of a Generic Three-Dimensional Scramjet Inlet at Mach 10, NASA Technical Paper 3476, Jan 1995.
- 11) Hughes W.F., Young F.J., The Electromagnetodynamics of Fluids, John Wiley & Sons, Inc. New York USA, 1966.
- 12) Macheret S.O., Shneider M.N., Miles R.B. Scramjet Inlet Control by Off-Body Energy Addition: A Virtual Cowl. 41st AIAA Aerospace Sciences Meeting and Exhibit, 2003-0032, 2003.

- 13) Macheret S.O., Shneider M.N., Miles R.B. External Supersonic Flow and Scramjet Inlet Control By MHD with Electron Beam Ionization, AIAA 39th Aerospace Sciences Meeting & Exhibit, 2001-0492, 2001.
- 14) Macheret S.O., Shneider M.N., Miles R.B. Magnetohydrodynamic and Electrohydrodynamic Control of Hypersonic Flows of Weakly Ionized Plasmas. 33rd AIAA Plasmadynamics and Lasers Conference, 2002-2249, 2002.
- 15) Molder S., McGregor R.J., Paisley T.W.. A Comparison of Three Hypersonic Air Inlets. Ryerson Polytechnical Institute, Toronto, 1991.
- 16) Murphy L., Statement on the Control of Numerical Accuracy, Journal of Fluids Engineering, <http://journaltool.asme.org/Templates/JFENumAccuracy.pdf>, 2004.
- 17) Paciorri R., Dieudonne W., Degrez G., Charbonnier J.M., Deconinck H., Validation of the Spalart-Allmaras Turbulence Model for Application in Hypersonic Flows, AIAA paper 97-2023, 1997.
- 18) Schetz J.A. Boundary Layer Analysis. Prentice Hall, New Jersey USA, 1993.
- 19) Streeter V.L. (Editor) Handbook of Fluid Dynamics, McGraw-Hill, New York USA 1961.
- 20) Tam C., Baurle R.A., Streby G.D. Numerical Analysis of Streamline-Traced Hypersonic Inlets. AIAA Paper, 2003-0013, 2003.
- 21) White F.M. Fluid Mechanics 4th Edition. WCB Mc.Graw-Hill, Toronto, 1999.
- 22) Wu J.H.T. On a Two-Dimensional Perforated Intake Diffuser. Aerospace Engineering, vol.21 no.7, 1962.

## APPENDIX A – SUPPLEMENTARY PROGRAMS: MATLAB SOURCE CODE

```
%-----%
%Sonic Flow Coefficient Calculator %
%By: Szymon Buhajczuk %
%See Section 1.7 for theory %
%-----%

clc; %Clears Screen
clear all; %Clears all variables from memory

Throat_Area = 4.399/1000; %Bleed slot width
CFD_Mass_Flow = -0.0437 %Mass flow obtained from CFD solution

%Flow Field Properties
%-----%
ftp = 756519; %Total Pressure
ftt = 532.272; %Total Temperature
gamma = 1.4; %Specific Heat Ratio for Air
R_const = 287; %Gas Constant for Air

%Calculations
%-----%
rho_total = ftp / (R_const * ftt) %Stagnation Density
rho_star = rho_total * (2/(gamma+1))^(1/(gamma-1)) %Density at Sonic
T_star = ftt * (2/(gamma+1)) %Temperature at Sonic
a_star = sqrt(gamma*R_const*T_star) %Speed of Sound at Sonic

mass_flow_rate = rho_star*Throat_Area*a_star %Ideal mass flow rate

Q = CFD_Mass_Flow/ mass_flow_rate %Sonic Flow Coefficient
disp(Q)

%-----%
%Displacement Thickness Calculator %
%By: Szymon Buhajczuk %
%See section 1.8 for theory %
%-----%

clc; %Clears Screen
clear all; %Clears all variables from memory
load vel398.txt %Loads Velocity Data from FLUENT file
load dens398.txt %Loads Density Data from FLUENT file
vel = vel398; %Populates Velocity Array
rho = dens398; %Populates Density Array
total_int = 0; %Clears running sum for integral

filesize = size(Rho); %Determines the size of array
for i = 2:1:filesize(1) %Starts summation
    rho_avg = (Rho(i-1,1)+Rho(i,1))/2; %Takes average density (n & n-1)
    vel_avg = (Vel(i-1,1)+Vel(i,1))/2; %Takes average velocity (n & n-1)
    dy = Vel(i,2)-Vel(i-1,2); %Interval size
    prod = Vel(filesize_1,1)*Rho(filesize_1,1);
    total_int = total_int + (1-(rho_avg*vel_avg)/(prod))*dy; %Adds to sum
end
Displacement_Thickness = total_int %Displays final Sum
```



```

%-----%
%Richardson's Extrapolation %
%By: Szymon Buhajczuk %
%Based on Theory in: %
%Journal of Fluids Engineering %
%Editorial Policy, Statement on %
%the Control of Numerical Accuracy %
%See section 4.5.1 for theory %
%-----%

clear all
clc

h1 = 0.002744961688; %fine grid %Grid size
M1 = 0.3655623; %Respective Mass Flow rate

h2 = 0.003589090278; %intermediate grid %Grid Size
M2 = 0.36718; %Respective Mass Flow rate

h3 = 0.004678427062; %coarse grid %Grid Size
M3 = 0.36927; %%Respective Mass Flow rate

r21 = h2/h1 %Grid Refinement Factor 1
r32 = h3/h2 %Grid Refinement Factor 2
s = sign((M3-M2)/(M2-M1)) %Sign of Ratio

p=1; %Order Initialization
resid =1 %Residual Initialization
while abs(resid) > 0.000001 %Iterative Loop for calculate order
    p=p+0.000001
    q = log(((r21^p)-s)/((r32^p)-s));
    resid = p - (abs(log(abs((M3-M2)/(M2-M1))))+q))/log(r21);
end
M_fine = ((r21^p)*M1-M2)/(r21^p-1) %Calculating Extrapolated value

```

## APPENDIX B – DETAILED FLUENT SETTINGS SUMMARY

FLUENT

Version: 2d, coupled imp, S-A (2d, coupled implicit, spalart-Allmaras)

Release: 6.2.16

Title:

### Models

Model	Settings
Space	2D
Time	Steady
Viscous	Spalart-Allmaras turbulence model
Production option	vorticity
Heat Transfer	Enabled
Solidification and Melting	Disabled
Radiation	None
Species Transport	Disabled
Coupled Dispersed Phase	Disabled
Pollutants	Disabled
Soot	Disabled

### Solver Controls

#### Equations

Equation	Solved
Flow	yes
Modified Turbulent Viscosity	yes
User Scalar 0	yes

#### Numerics

Numeric	Enabled
Absolute Velocity Formulation	yes

#### Relaxation

Variable	Relaxation Factor
Modified Turbulent Viscosity	0.80000001
Turbulent Viscosity	0.80000001
Solid	0.80000001
User Scalar 0	1

#### Linear Solver

Variable	Solver Type	Termination Criterion	Residual Reduction Tolerance
Flow	F-Cycle	0.1	
Modified Turbulent Viscosity	Flexible	0.1	0.7
User Scalar 0	Flexible	0.1	0.7

#### Discretization Scheme

Variable	Scheme
Flow	Second Order Upwind
Modified Turbulent Viscosity	Second Order Upwind
User Scalar 0	First Order Upwind

#### Time Marching

Parameter	Value
Solver	Implicit
Courant Number	1

#### Solution Limits

Quantity	Limit
Minimum Absolute Pressure	1e-15

Maximum Absolute Pressure	4.9999999e+12
Minimum Temperature	1e-15
Maximum Temperature	5e+11
Maximum Turb. Viscosity Ratio	9.9999998e+10

#### Material Properties

Material: air (fluid)

Property	Units	Method	Value(s)
Density	kg/m3	ideal-gas	#f
Cp (Specific Heat)	j/kg-k	constant	1006.43
Thermal Conductivity	w/m-k	constant	0.0242
Viscosity	kg/m-s	sutherland	(1.716e-05 273.10999 110.56
Molecular weight	kg/kgmol	constant	28.966
L-J Characteristic Length	angstrom	constant	3.711
L-J Energy Parameter	k	constant	78.6
Thermal Expansion Coefficient	1/k	constant	0
Degrees of Freedom		constant	0
UDS Diffusivity	kg/m-s	constant	0.01
Speed of Sound	m/s	none	#f

Material: aluminum (solid)

Property	Units	Method	Value(s)
Density	kg/m3	constant	2719
Cp (Specific Heat)	j/kg-k	constant	871
Thermal Conductivity	w/m-k	constant	202.4

## APPENDIX C – USER DEFINED FUNCTIONS: ANSI C SOURCE CODE

```

/*****
/* UDF Defining the Source term in the User Defined */
/* Scalar Transport (Scalar being Static Charge) */
/* By: Szymon Buhajczuk */
/* Based on templates in FLUENT user manual */
*****/
#include "udf.h"
#include "math.h"

#define magnetic_field 0.5
#define parabolic_growth 1.0
#define shearconst 100000
#define phiconst 30000000
#define pi 3.14159265

DEFINE_SOURCE(charge_source, cell, thread, ds, eqn)
{
    real charge_source;

    /*Source Term*/
    charge_source = shearconst*exp(-C_UDSI(cell,thread,0)/phiconst) * C_R(cell,thread) *
    C_MU_T(cell,thread) * (abs(C_DUDY(cell,thread))+abs(C_DVDX(cell,thread)));

    /*Derivative of Source Term*/
    ds[eqn]=-(shearconst/phiconst)*exp(-C_UDSI(cell,thread,0)/phiconst)*C_R(cell,thread)
    * C_MU_T(cell,thread)*(abs(C_DUDY(cell,thread))+abs(C_DVDX(cell,thread)));

    return charge_source;
}

/*****
/* UDFs Defining the Source term in the Momentum */
/* Equations based on magnetic field */
/* By: Szymon Buhajczuk */
/* Based on templates in FLUENT User Manual */
*****/
DEFINE_SOURCE(xmom_source, cell, thread, ds, eqn)
{
    real xm_source;
    /*Source Term*/
    xm_source=-magnetic_field*C_UDMI(cell,thread,0)*C_UDSI(cell,thread,0)
    * C_R(cell,thread) * C_V(cell,thread);

    /*Derivative of Source Term*/
    ds[eqn]= 0.0;

    return xm_source;
}

DEFINE_SOURCE(ymom_source, cell, thread, ds, eqn)
{
    real ym_source;

    /*Source Term*/
    ym_source = magnetic_field*C_UDMI(cell,thread,0)*C_UDSI(cell,thread,0)
    *C_R(cell,thread)*C_U(cell,thread);

    /*Derivative of Source Term*/
    ds[eqn]= 0.0;

    return ym_source;
}

/*****
/* UDF Defining the shape of the magnetic field */
/* through the use of User Defined Memory */
/* By: Szymon Buhajczuk */
/* Based on templates in FLUENT User Manual */
*****/

DEFINE_ON_DEMAND(field_target_zone)
{
    Domain *d;

```

```

Thread *t;
cell_t c;
real linear_slope;
real x_field_scale;
real y_field_scale;
real coord[ND_ND];
real x,y;
d = Get_Domain(1);

thread_loop_c(t,d)
{
    begin_c_loop(c,t)
    {
        C_CENTROID(coord,c,t);
        x=coord[0];
        y=coord[1];

        x_field_scale = 0;
        y_field_scale = 0;
        if (x>=1.74)
        {
            if (x<=1.76)
            {
                if (y>=-0.025)
                {
                    if (y<=0.015)
                    {
                        x_field_scale = -10000*(x-1.75)*(x-1.75)+1;
                        y_field_scale = -2500*(y+0.005)*(y+0.005)+1;
                    }
                }
            }
        }
        C_UDMI(c,t,0) = x_field_scale*y_field_scale;
    }
    end_c_loop(c, t)
}
}

```

## APPENDIX D – RAW RESULT DATA

Nodes (x1000)	Mass Flow Rate (kg/s) (Magnetic Field Off, Spalart Allmaras)	Mass Flow Rate (kg/s) (Magnetic Field Off, k-e)	Mass Flow Rate (kg/s) (Magnetic Field On, Spalart Allmaras)
15.029	0.378		0.1397
19.754			0.1387
21.394	0.374	0.375	
31.211	0.371	0.372	0.1345
52.852	0.369	0.369	0.1363
89.744	0.367	0.366	0.1360
153.067	0.366		0.1399

Table 5 : Grid Independence Study and Turbulence Model Selection Data

Shear Charge Scaling Constant, c	Mass Flow Rate (kg/s)	Maximum Charge (coulombs/kg)	Sonic Flow Coefficient	Oscillation
1.E+03	3.67E-01	1.02E+03	6.30E-02	
1.E+04	3.41E-01	1.02E+04	5.85E-02	
3.E+04	2.86E-01	3.08E+04	4.91E-02	
5.E+04	2.38E-01	5.17E+04	4.07E-02	+/- 0.4%
8.E+04	1.76E-01	8.52E+04	3.01E-02	+/- 1.0%
9.E+04	1.54E-01	9.91E+04	2.63E-02	+/- 1.5%
1.E+05	1.34E-01	1.13E+05	2.31E-02	
2.E+05	4.36E-02	2.41E+05	7.47E-03	
3.E+05	8.52E-02	3.77E+05	1.46E-02	
4.E+05	3.83E-02	6.05E+05	6.57E-03	

Table 6: Charge equation constant independence study, c constant variation

Charge Derivative Scaling Constant, $\hat{\phi}$	Mass Flow Rate (kg/s)	Maximum Charge (coulombs/kg)	Sonic Flow Coefficient	Oscillation
3.E+03	3.36E-01	1.02E+04	5.76E-02	
3.E+04	2.47E-01	4.31E+04	4.24E-02	+/- 0.4%
3.E+05	1.60E-01	9.32E+04	2.74E-02	
3.E+06	1.37E-01	1.11E+05	2.35E-02	
3.E+07	1.34E-01	1.13E+05	2.31E-02	
5.E+07	1.34E-01	1.13E+05	2.30E-02	
7.E+07	1.34E-01	1.13E+05	2.30E-02	
3.E+08	1.34E-01	1.13E+05	2.30E-02	
3.E+09	1.34E-01	1.13E+05	2.30E-02	
3.E+10	1.34E-01	1.13E+05	2.30E-02	

Table 7: Charge equation constant independence study,  $\hat{\phi}$  constant variation

Core Field Strength (Tesla)	Mass Flow Rate (kg/s)	Sonic Flow Coefficient	Oscillation
0	3.72E-01	6.37E-02	
0.1	3.13E-01	5.37E-02	
0.2	2.62E-01	4.49E-02	
0.3	2.15E-01	3.69E-02	
0.4	1.76E-01	3.01E-02	+/- 0.6%
0.5	1.34E-01	2.31E-02	
0.6	1.06E-01	1.81E-02	
0.7	7.60E-02	1.30E-02	
0.8	5.13E-02	8.80E-03	+/- 4.8%
0.9	3.94E-02	6.76E-03	
1	4.36E-02	7.48E-03	

Table 8: Field Strength Variation Study Data

Y position (mm)	Mass Flow Rate (kg/s)	Sonic Flow Coefficient	Oscillation
-5	1.34E-01	2.31E-02	
-4	1.28E-01	2.19E-02	+/- 0.4%
-3	1.22E-01	2.10E-02	
-2	1.18E-01	2.02E-02	
-1	1.15E-01	1.97E-02	
0	1.12E-01	1.93E-02	+/- 0.67%
1	1.11E-01	1.90E-02	+/- 0.63%
2	1.11E-01	1.90E-02	
3	1.11E-01	1.90E-02	
4	1.11E-01	1.90E-02	+/- 0.67%

Table 9: Vertical Field Positioning Optimization Data

X position (mm)	Mass Flow Rate (kg/s)	Sonic Flow Coefficient	Oscillation
0	1.11E-01	1.90E-02	
-1	9.08E-02	1.56E-02	+/- 2.1%
-2	7.25E-02	1.24E-02	+/- 2.1%
-3	5.81E-02	9.97E-03	
-4	4.73E-02	8.12E-03	
-5	4.37E-02	7.50E-03	
-6	4.58E-02	7.85E-03	
-7	5.00E-02	8.58E-03	

Table 10: Horizontal Field Positioning Optimization Data

Slot Angle ( $\theta$ ) Degrees	Mass Flow Rate (kg/s) Field Off	Mass Flow Rate (kg/s) Field On	Sonic Flow Coefficient, Field Off	Sonic Flow Coefficient, Field On	% SFC Drop
70	4.49E-01	8.17E-02	7.71E-02	1.40E-02	81.82
80	4.09E-01	7.49E-02	7.01E-02	1.28E-02	81.67
90	3.71E-01	4.37E-02	6.36E-02	7.50E-03	88.22

Table 11: Slot Geometry Variation Study Data (Slot Angle Variation)

d*/D	Lead Plate Length (m)	Mass Flow Rate (kg/s) Field Off	Mass Flow Rate (kg/s) Field On	Sonic Flow Coefficient, Field Off	Sonic Flow Coefficient, Field On	% SFC Drop
0.95	1.75	3.71E-01	4.37E-02	6.37E-02	7.50E-03	88
0.79	1.25	3.74E-01	1.20E-01	6.42E-02	2.06E-02	68
0.67	0.95	3.75E-01	1.83E-01	6.43E-02	3.14E-02	51
0.54	0.75	3.77E-01	2.35E-01	6.47E-02	4.04E-02	38
3.39E-04	0.25	3.88E-01	3.63E-01	6.65E-02	6.22E-02	6

Table 12: Boundary Layer Displacement Thickness Influence Data

Mach #	Mass Flow Rate (kg/s) Field Off	Mass Flow Rate (kg/s) Field On	Sonic Flow Coefficient, Field Off	Sonic Flow Coefficient, Field On	% SFC Drop
1	-4.27E-01	-2.32E-01	2.89E-01	1.57E-01	46
1.2	-3.97E-01	-1.78E-01	2.09E-01	9.41E-02	55
1.4	-3.87E-01	-1.34E-01	1.56E-01	5.39E-02	65
1.6	-3.82E-01	-8.81E-02	1.15E-01	2.65E-02	77
1.8	-3.77E-01	-5.56E-02	8.40E-02	1.24E-02	85
1.97	-3.71E-01	-4.37E-02	6.36E-02	7.49E-03	88
2.2	-3.62E-01	-3.40E-02	4.33E-02	4.08E-03	91
2.4	-3.52E-01	-2.92E-02	3.09E-02	2.56E-03	92

Table 13: Mach number Influence Data

Pressure Ratio ( $P_{\text{PLENUM}} / P_{\text{FREESTREAM}}$ )	Total Pressure Ratio ( $P_{\text{PLENUM}} / P_{\text{TOTALFREESTREAM}}$ )	Mass Flow Rate (kg/s) Field Off	Mass Flow Rate (kg/s) Field On	Sonic Flow Coefficient, Field Off	Sonic Flow Coefficient, Field On	% SFC Drop
0.100	0.027	3.71E-01	4.37E-02	6.36E-02	7.50E-03	88
0.200	0.054	3.71E-01	3.66E-02	6.37E-02	6.27E-03	90
0.400	0.107	3.33E-01	7.65E-03	5.71E-02	1.31E-03	98
0.600	0.161	1.51E-01	-8.38E-02	2.60E-02	-1.44E-02	155

Table 14: Pressure Ratio Influence Data